Università della Calabria

Dottorato di Ricerca in Ingegneria Idraulica
per l'Ambiente e il Territorio
(XXIII ciclo)

- Settore Scientifico Disciplinare: ICAR/02 -

Simulating Open-Channel Flows and Advective Diffusion Phenomena through SPH Model

- Ivan Federico -

Ivan Federico

Coordinatore:
Prof. Francesco Macchione

Francesco Macchione

Tutors:
Prof. Paolo Veltri
Veltri
Dr. Andrea Colagrossi

Andrea Colagrossi

Novembre 2010

Ivan Federico: *Simulating Open-Channel Flows and Advective Diffusion Phenomena through SPH Model*, PhD Thesis , © november 26, 2010.

A mia madre, mio padre e mio fratello.

Ascoltare Wicked Gravity di Jim Carroll.
Credo che in quel periodo
la mia vita fosse tutta lì.

— E. Clementi

ABSTRACT

The present thesis treats Computational Fluid Dynamics based on particle methods. The fully Lagrangian approach Smoothed Particle Hydrodynamics (SPH) is developed for two-phase flows. The model is extended to research fields of environmental hydraulic and open-channel flows. SPH is a Lagrangian, meshless and particle model. It was born about 30 years ago to solve gas-dynamics problems in open space (Lucy, 1977 [1]; Gingold and Monaghan, 1977 [2]). For many years, the SPH method has been applied to problems in the astrophysical field, as documented in the review paper by Benz (1990) [3]. During the last decades, the SPH method has been increasingly modified and extended to provide approximations to the partial difference equations (PDEs) in a wide range of scientific and engineering applications particularly in the hydrodynamic field. Monaghan (1994) [4] was the first to apply the SPH scheme to fluid-dynamics problems. After that, the SPH approach has been successfully extended to multiphase flows (see e.g. Grenier et *al.*, 2009 [5]) and fluid-structure interaction problems (see *e.g.* Colagrossi and Landrini, 2003 [6]). Following the SPH method, the motion of a continuum medium is described using an interpolation technique which allows to approximate functions and differential operators on an irregular distribution of points. In the standard SPH, where a weakly compressible fluid is considered, the discretized continuity and momentum equations are linked via a state equation.

Firstly, an algorithm is developed to treat upstream/downstream boundary conditions for 2D open-channel flows in SPH context. For this purpose two suitable sets of particles (in/out-flow particles) are defined allowing the enforcement of different upstream and downstream flow conditions. In particular this permits to avoid generation of unphysical pressure shock waves due to a direct creation/deletion of fluid particles. As first test case, the proposed algorithm is validated for a viscous laminar flow in open channel considering Reynolds numbers of order $\mathcal{O}(10^2)$. The obtained results are compared with analytical ones in order to heuristically check the convergence of the numerical scheme. The simulations are performed for a time interval long enough to reach steady state conditions. The suitability of the in/out-flow algorithm has been highlighted comparing the velocity field with the analytical Poiseuille solution. The second test case deals with a hydraulic jump for which different upstream and downstream conditions are needed. Several types of jumps, obtained varying the flow Froude number, are investigated with particular reference to the location of the jump and the velocity field. Comparisons between the numerical results and the classical theory of the hydraulic jump are provided, showing good agreements.

In the second part of the thesis, the SPH model is applied to evaluate the concentration field of pollutants in water. A Lagrangian formalism is formulated to solve the fickian diffusion equation considering pollutants with the same density as the water. Furthermore, a SPH form of the advective diffusion equation is also developed for pollutant-water, taking into account the effects of molecular diffusion and natural advection induced by differences between the fluid densities. These equations are coupled with the fluid mechanics equations. Attention is paid to the numerical aspects involved in the solution procedure and to the optimization of the model parameters. Environmental engineering problems concerning diffusion and natural advection phenomena occur in the presence of a pollutant in still water. Numerical tests referring to a strip and a bubble of contaminant in a water tank with different initial concentration laws have been carried out. The results obtained by the proposed SPH models are compared with other available SPH formulations, showing an overall better agreement with standard analytical solutions in terms of spatial evolution of the concentration values. Capabilities and limits of the proposed SPH models to simulate advective diffusion phenomena for a wide range of density ratios are discussed.

As future perspectives, coupling the two aspects considered in this thesis, it will be developed a numerical code for the simulation of the concentration field along a water stream by an intake of pollutants.

SOMMARIO

La presente tesi si occupa di Fluidodinamica Computazionale, basata su metodi particellari. L'approccio lagrangiano Smoothed Particle Hydrodynamics (SPH) è stato sviluppato per flussi bifase. Il modello è stato esteso al campo di ricerca dell'idraulica ambientale e ai flussi in canali a superficie libera. SPH è un modello particellare di tipo lagrangiano e meshless. E' stato ideato circa 30 anni fa per problemi di gas-dinamica in spazi aperti (Lucy, 1977 [1]; Gingold e Monaghan, 1977 [2]). Per molti anni, è stato applicato a problemi di astrofisica, come documentato nel lavoro di Benz (1990) [3]. Negli ultimi decenni, il metodo SPH è stato modificato ed esteso in modo da fornire approssimazioni delle equazioni alle derivate parziali in un vasto campo scientifico e per differenti applicazioni ingegneristiche. Monaghan (1994) [4] fu il primo ad applicare il modello SPH a problemi di fluidodinamica. In seguito, tale approccio è stato esteso con successo a flussi multifase (Grenier et *al.*, 2009 [5]) e a casi di interazione fluido-struttura (Colagrossi e Landrini, 2003 [6]). Attraverso lo schema SPH, il movimento di un mezzo continuo è descritto mediante una tecnica di interpolazione che permette di approssimare funzioni e operatori differenziali con una distribuzione irregolare di punti. Nel modello SPH standard, in cui il fluido è considerato debolmente comprimibile, l'equazioni del moto e di continuità, espresse in forma discreta, sono relazionate a un'equazione di stato.

Nella tesi, è stato sviluppato, inizialmente, un algoritmo, nel contesto SPH, che consente di trattare condizioni al contorno di monte e di valle in canali bidimensionali a pelo libero. A questo scopo, sono state definiti due appropriati set di particelle (particelle inflow e outflow) che permettono l'imposizione di differenti condizioni del flusso di monte e di valle. Ciò permette di evitare la generazione di shock di pressione non fisici attraverso un meccanismo di diretta creazione e cancellazione delle particelle. Come primo caso, l'algoritmo proposto è stato validato a flussi viscosi laminari in canali a superficie libera, considerando numeri di Reynolds dell'ordine di $\mathcal{O}(10^2)$. I risultati ottenuti sono stati confrontati con soluzioni analitiche al fine di controllare euristicamente la convergenza dello schema. Le simulazioni sono state realizzate per lunghi intervalli di tempo al fine di raggiungere lo stato di stazionarietà. L'efficienza dell'algoritmo in/out-flow è stata evidenziata confrontando il campo di velocità valutato numericamente con la soluzione analitica di Poiseuille. Il secondo test studiato riguarda casi di risalti idraulici, dove, inevitabilmente, sono necessarie condizioni al contorno di monte e di valle differenti tra loro. Variando il numero di Froude, diversi casi di risalto sono stati indagati con particolare riferimento alla posizione del suo fronte e al campo di velocità. Sono forniti confronti tra i risultati numerici e la classica teoria del risalto idraulico, mostrando buoni accordi.

Nella seconda parte della tesi, il modello SPH è stato applicato a casi di valutazione del campo di concentrazione di contaminati in acqua. E' stato proposto un nuovo formalismo lagrangiano per la risoluzione dell'equazione di diffusione fickiana, considerando inquinanti con densità simile a quella

dell'acqua. Inoltre, una forma discreta e particellare dell'equazione di advezione diffusione è stata sviluppata per casi di interazione tra contaminanti e acqua, considerando gli effetti di diffusione molecolare e di advezione naturale indotti dalla differenza di densità tra le diverse fasi fluide. Tali equazioni sono state accoppiate alle equazioni della meccanica dei fluidi. Particolare attenzione è stata rivolta agli aspetti numerici coinvolti nella procedura di risoluzione e all'ottimizzazione dei parametri del modello. Nei test considerati, i fenomeni di diffusione e advezione naturale avvengono in presenza di contaminante in acqua ferma. Sono stati simulati casi di strisce e bolle di contaminante in un serbatoio d'acqua con differenti leggi di concentrazione iniziali. I risultati ottenuti attraverso il modello SPH proposto hanno mostrato, in termini di evoluzione spaziale dei valori di concentrazione, un accordo globale con le soluzioni analitiche di riferimento migliore rispetto ad altre formulazioni SPH presenti in letteratura. Sono state discusse, infine, le capacità e i limiti dei modelli SPH proposti nel simulare processi di diffusione advettiva, considerando un ampio range di variazione dei rapporti di densità.

Come prospettive future, integrando i due aspetti studiati nella tesi, si vuole sviluppare un codice numerico, in linguaggio parallelo, in grado di simulare tratti di canali a pelo libero con immissioni di contaminante e valutarne il campo di concentrazione considerando i fenomeni di dispersione e diffusione turbolenta.

RINGRAZIAMENTI

Desidero ringraziare il prof. Paolo Veltri per la guida, l'equilibrio, i consigli e la fiducia. Per avermi seguito nel mio percorso di studi universitari, da quando le piogge venivano giù intense per una durata inferiore a 1 ora, a quando i fiumi si autodepuravano riossigenandosi, a ora che delle particelle si scontrano variando le loro caratteristiche fisiche.

Ringrazio Andrea Colagrossi e Salvatore Marrone per avermi insegnato tanto su *SPH*. Il primo per aver sempre conciliato il rigore scientifico alla leggerezza. Il secondo per tante, tante cose che non sto qui a elencare ma che spaziano in un range larghissimo che va dagli aspetti più tecnicamente computazionali all'eccessivo dosaggio di mandorle nel *pesto alla trapanese*.

Ringrazio Francesco Aristodemo per i consigli, i suggerimenti, la vicinanza e il supporto durante tutto il periodo di dottorato.

Desidero ringraziare gli amici e i colleghi del Dipartimento di Difesa del Suolo dell'Università della Calabria, in particolare Attilio (perchè di tempo ne è passato dall'esercitazione sulle scale di deflusso in sezione rettangolare!), Bianca, Giuseppe e Ali.

Ringrazio i ricercatori del Dipartimento di Sea-Keeping e Manovrabilità dell'*INSEAN*, per il costruttivo periodo di ricerca a Roma. Un grazie speciale va alla *Dynamo US3* per l'applicazione del metodo scientifico agli schemi calcistici!

Ringrazio gli amici e le persone con cui ho cercato di migliorarmi quotidianamente, coltivando e condividendo con loro interessi e passioni. Un grazie particolare a Marco per l'amicizia e il supporto TEXnico.

Il ringraziamento più sentito va alla mia famiglia, per la serenità e il sostegno quotidiano e incondizionato.

Rende, 26 Novembre 2010

IVAN FEDERICO

CONTENTS

1 INTRODUCTION 1
  1.1 Background and motivations 1
  1.2 An overview on Particle and Meshless Methods 3
    1.2.1 Eulerian vs. Lagrangian approach 3
    1.2.2 Some methods 3
  1.3 Smoothed Particle Hydrodynamics: the state-of-art 5
  1.4 Structure of the thesis 12

I Numerical Model: Smoothed Particle Hydrodynamics 13

2 MESHLESS OPERATORS IN LAGRANGIAN METHODS 15
  2.1 Integral interpolation techniques 15
  2.2 Types of kernel functions 18
  2.3 Neighbours search strategy 20
    2.3.1 Linked list 20

3 FLUID MECHANICHS EQUATIONS IN SPH CONTEXT 23
  3.1 Governing equations in Fluid Mechanics 23
  3.2 SPH discrete formalism of Fluid Mechanics Equations 24
    3.2.1 Continuity Equation 24
    3.2.2 Momentum Equation 25
    3.2.3 State Equation 26
    3.2.4 Numerical recipes for the code effectiveness 27
  3.3 Two-phase SPH discrete formalism (Grenier et al., 2009) 29
  3.4 Summarizing continuity and momentum equations used for the simulations 31
  3.5 Time integration for Fluid Mechanics Equations 32

4 DIFFUSION AND ADVECTIVE DIFFUSION EQUATIONS IN SPH CONTEXT 35
  4.1 Governing equations in Environmental Hydraulics 35
  4.2 A novel SPH discrete formalism of Environmental Hydraulic Equations 36
    4.2.1 Diffusion Equation 36
    4.2.2 Advective Diffusion Equation 38
    4.2.3 Reactive Diffusion Equation 38
  4.3 Time integration coupling Diffusion equation to Fluid Mechanics Equations 39

5 BOUNDARY CONDITIONS TREATMENT 41
  5.1 Free-surface Boundary Conditions 41
  5.2 Solid Boundary Conditions 41
    5.2.1 Repulsive Forces 42
    5.2.2 Bounce back 44
    5.2.3 Dummy Particles 45
    5.2.4 Ghost Particles 45

5.2.5 Coupling of Repulsive Forces and Ghost Particles 46
5.2.6 Fixed Ghost Particles 47
5.3 In/Out-Flow Boundary Conditions 48
5.3.1 A novel algorithm for simulating open-channel flows 48

II Physical Investigations 51

6 SIMULATIONS OF DAM BREAKS ON SILLS 53
6.1 Test case: dam-breaks on trapezoidal sills 53
6.1.1 Test case 1 53
6.1.2 Test case 2 54
6.1.3 Test case 3 55

7 SIMULATIONS OF OPEN-CHANNEL FLOWS 61
7.1 Viscous free-surface channel flows in laminar regime 61
7.2 Hydraulic jump 64
7.2.1 Hydraulic jump with initial condition no. 1 65
7.2.2 Hydraulic jump with initial condition no. 2 68
7.3 Concluding remarks 71

8 SIMULATIONS OF TWO-PHASE FLOWS 73
8.1 Evolution of pollutant in water 73
8.2 Evolution of air in water 74

9 SIMULATIONS OF DIFFUSION AND ADVECTIVE DIFFUSION PHENOMENA 77
9.1 Diffusion of pollutant in water 77
9.1.1 Strip of pollutant with initial uniform concentration. 78
9.1.2 Strip of pollutant with initial exponential concentration. 80
9.1.3 Bubble of pollutant with initial exponential concentration. 80
9.2 Reactive diffusion of pollutant in water 81
9.2.1 Bubble of pollutant with initial exponential concentration. 81
9.3 Advective diffusion of pollutant in water 83
9.4 Concluding remarks 89

10 CONCLUSIONS AND FUTURE PERSPECTIVES 91

BIBLIOGRAPHY 93

LIST OF FIGURES

Figure 1 Sketch of the kernel function. 16

Figure 2 Particle interaction in the SPH model: neighbors particles of a given particle. 20

Figure 3 Particle grid cells in the fluid domain (on the left) and linked list through neighbors grid cells (on the right). 20

Figure 4 Reduced linked list algorithm over five grid cells. 21

Figure 5 Repulsive forces boundary conditions. On the top, distances between a fluid particle (blue particle) and a boundary particle (red particles). On the bottom, repulsive contributions of two boundary particles. 43

Figure 6 Bounce back method. 44

Figure 7 Example of use of ghost particles to enforce no-penetration boundary condition. 46

Figure 8 Sketch of fixed ghost particles for the channel bottom. 47

Figure 9 Initial sketch of the computational domain: different colours are associated to different sets of particles. 48

Figure 10 Configuration of the whole particles array (a). Array sketch showing how the in/out-flow algorithm works at each step (b). 49

Figure 11 Test case 1: sketch of the experimental set-up. 54

Figure 12 Test case 1: SPH configurations for $t = 0\,s$, $3\,s$, $6\,s$, $10\,s$ and $15\,s$. 55

Figure 13 Test case 1: comparisons between numerical results and experimental data at three different gauges. 56

Figure 14 Test case 2: sketch of the experimental set-up. 56

Figure 15 Test case 2: SPH configurations for $t = 0\,s$, $2\,s$, $4\,s$, $10\,s$ and $15\,s$. 57

Figure 16 Test case 2: comparisons between numerical results and experimental data at three different gauges. 58

Figure 17 Test case 3: sketch of the experimental set-up. 58

Figure 18 Test case 3: SPH configurations for $t = 0\,s$, $2\,s$, $4\,s$, $10\,s$ and $15\,s$. 59

Figure 19 Test case 3: comparisons between numerical results and experimental data at three different gauges. 60

Figure 20 Sketch of the elementary fluid domain 62

Figure 21 Particles distributions and velocity field at $t(g/h)^{1/2} = 50$ (a) and $t(g/h)^{1/2} = 100$ (b) for a free-surface channel flow in laminar regime. The Reynolds number is $Re = 10$. 63

Figure 22 Particles distribution and velocity field at $t(g/h)^{1/2} = 100$ for $Re = 100$ (a) and $Re = 200$ (b). 63

Figure 23 Comparisons between analytical solution and numerical results at $t(g/h)^{1/2} = 100$ and $x = h$ for $Re = 10, 100$ and 200. 63

Figure 24 Time variation of MSEP for dx_1, dx_2 and dx_3 ($Re = 10$). 64

Figure 25 Sketch of a hydraulic jump with control volume. 65

Figure 26 Sketch of in/out-flow boundary conditions and initial condition *no. 1*. 66

Figure 27 SPH configuration for the undular jump ($Fr_1 = 1.15$, $Fr_2 = 0.87$ and $h_2/h_1 = 1.2$) at $t(g/h_1)^{1/2} = 150$. The colours represent the horizontal component of the velocity field. 66

Figure 28 SPH configurations for the weak jump ($Fr_1 = 1.88$, $Fr_2 = 0.57$ and $h_2/h_1 = 2.2$) at $t(g/h_1)^{1/2} = 1$, $t(g/h_1)^{1/2} = 50$, $t(g/h_1)^{1/2} = 100$ and $t(g/h_1)^{1/2} = 500$. The colours represent the horizontal component of the velocity. 67

Figure 29 Time variation of the upstream and downstream pressure forces adopting the initial condition *no. 1*. 67

Figure 30 Sketch for the determination of the pressure forces. 68

Figure 31 Sketch of in/out-flow boundary conditions and initial condition *no. 2*. 69

Figure 32 SPH configurations at $t\,(g/h_1)^{1/2} = 150$ for the considered hydraulic jumps. The colours represent the horizontal component of the velocity. 70

Figure 33 Time variation of the upstream and downstream pressure forces adopting the initial condition *no. 2*. 71

Figure 34 Comparisons between non-dimensional numerical water depths and theoretical ones at $x_1 = 7.0h_1$. 72

Figure 35 Comparisons between non-dimensional numerical water depths and theoretical ones at $L/h_1 = 20.0h_1$. 72

Figure 36 Sketch of the bubble in tank and adopted nomenclature. 74

Figure 37 2D evolution of pollutant circular bubble in still water at $t = 0.0s$, $t = 0.5s$, $t = 1.0s$ and $t = 1.5s$. 75

Figure 38 Time evolution of upper face for pollutant bubble: comparison between numerical results and analytical solution. 75

Figure 39 2D evolution of air circular bubble in still water at $t = 0.0s$, $t = 0.2s$, $t = 0.5s$ and $t = 0.7s$. 76

Figure 40 Time evolution of upper face for air bubble: comparison between numerical results and analytical solution. 76

Figure 41 Geometry of the computation domains and initial concentrations for the three diffusion test cases. 78

Figure 42 Comparisons between SPH diffusion models and analytical solution of the concentration field for a strip of pollutant with initial constant law (t = 1.00 s and 2.00 s). 79

Figure 43 Comparisons between SPH diffusion models and analytical solution of the concentration field for a strip of pollutant with initial exponential law ($t = 1.00$ s and 2.00 s). 81

Figure 44 Comparisons between SPH diffusion models and analytical solution of the concentration field for a bubble of pollutant with initial exponential law ($t = 1.00$ s and 2.00 s). 82

Figure 45 Maximum concentration curves C_{max}: comparison between SPH and analytical results varying the diffusion coefficient. 82

Figure 46 Sketch of the mixing layer for the bubble of pollutant. 83

Figure 47 Maximum concentration curves C_{max}: comparison between SPH and analytical results considering diffusion and reactive diffusion processes. 84

Figure 48 Comparisons between the proposed SPH diffusion model and analytical solution of the concentration field for a bubble of pollutant with initial exponential law and $\rho_2/\rho_1 = 0.3$ ($t = 0.00$ s, 0.20 s and 0.50 s). 85

Figure 49 Comparisons between SPH advective diffusion model and analytical solution of the concentration field for a bubble of pollutant with initial exponential law and $\rho_2/\rho_1 = 0.3$ ($t = 0.00$ s, 0.20 s and 0.50 s). 86

Figure 50 Comparisons between SPH advective diffusion model and analytical solution of the concentration field for a bubble of pollutant with initial exponential law and $\rho_2/\rho_1 = 0.5$ ($t = 0.00$ s, 0.20 s and 0.50 s). 86

Figure 51 Two-dimensional spatial distribution of particle velocities and concentration field of a bubble of pollutant with initial exponential concentration for $\rho_2/\rho_1 = 0.5$ (t = 0.00 s). 87

Figure 52 Two-dimensional spatial distribution of particle velocities and concentration field of a bubble of pollutant with initial exponential concentration for $\rho_2/\rho_1 = 0.5$ (t = 0.20 s). 87

Figure 53 Two-dimensional spatial distribution of particle velocities and concentration field of a bubble of pollutant with initial exponential concentration for $\rho_2/\rho_1 = 0.5$ (t = 0.50 s). 88

Figure 54 Three-dimensional view of the evolution of the concentration field of a bubble of pollutant with initial exponential concentration for $\rho_2/\rho_1 = 0.5$ ($t = 0.00$ s, 0.20 s and 0.50 s). 88

Figure 55 Root mean square errors vs. density ratios between pollutant and water ($t = 0.20$ s and 0.50 s). 89

LIST OF TABLES

Table 1 Test case 1: characteristic lengths of the experimental set-up. 54
Table 2 Test case 2: characteristic lengths of the experimental set-up. 57
Table 3 Test case 3: characteristic lengths of the experimental set-up. 57
Table 4 Upstream and downstream Froude numbers for the six hydraulic jumps varying h_2/h_1. 69

1 INTRODUCTION

CONTENTS

1.1 Background and motivations 1
1.2 An overview on Particle and Meshless Methods 3
  1.2.1 Eulerian vs. Lagrangian approach 3
  1.2.2 Some methods 3
1.3 Smoothed Particle Hydrodynamics: the state-of-art 5
1.4 Structure of the thesis 12

In this chapter, the background, the motivations and the aim of present thesis are defined. After a first overview on the meshless methods, attention will be focused on the Smoothed Particle Hydrodynamics model, considering its main features organized by topics. Finally, the structure of the thesis is illustrated.

1.1 BACKGROUND AND MOTIVATIONS

This thesis is rooted to Environmental Fluid Mechanics (EFM) background.

EFM is the scientific study of naturally occurring fluid flows of air and water on our planet Earth, especially of those flows that affect the environmental quality of air and water. Scales of relevance range from millimeters to kilometers, and from seconds to years.

The preceding definition also distinguishes EFM from classical fluid mechanics, the latter being chiefly concerned with artificial (engineered) fluid motions: flows in pipes and around airfoils, in pumps, turbines, heat exchangers and other machinery that utilizes fluids.

By contrast, EFM is exclusively concerned with only two fluids, air (or pollutant) and water, and moreover under a relatively narrow range of ambient temperatures and pressures. The objective of EFM also differs from that of classical hydraulics, which deals exclusively with free-surface water flow (Chow, 1959 [7]). Anyway, the development of classical hydraulics aspects, as open-channel flows, is necessary in order to deal with many EFM fields. For this reason in this work free-surface channel flows and environmental hydraulic problems are treated: the first ones considering uniform and non-uniform steady flows, the second ones referring to diffusion phenomena.

There are two primary modes of fluid transport that fall under the scope of EFM are:

- advection, which is the transport by the flow of the fluid itself;
- diffusion, which is the transport associated with random motions within the fluid. These random motions occur at the molecular scale

producing molecular diffusion or are caused by turbulence, causing turbulent diffusion. Molecular diffusion tends to be important in the close vicinity of interfaces, regulating for example the passage of a soluble gas between air and water, while turbulent diffusion tends to act mostly within the body of the system.

In EFM, main environmental interfaces need be considered, for example: air (or pollutant)-water and water-sediment. They are affected by the following processes:

- The air (or pollutant)-water interface is subjected to momentum, heat and mass transfer. the main actor in momentum transfer is the shear stress exerted as the result of a difference between wind speed and direction in the air and the surface velocity in the water. The shear stress generates a wave field, part of which goes to creating surface drift currents. The accompanying surface heat transfer represents a relevant source or sink of heat in producing the thermal structure of a water body. Finally, several chemicals are transferred upward to the air or downward to the water depending on the substances involved and departure from equilibrium (Henry's Law). This process is termed gas transfer. Hence, gas transfer of a volatile or semi-volatile chemical is a two-way process involving both dissolution by the water and volatilization into the air across an air-water interface. Finally, air-entrainment is the entrapment of undissolved air bubbles and air pockets by the flowing water.
- The water-sediment interface, which is very difficult to define precisely, is subjected to several complicated physical and chemical processes responsible for exchange of solids and solutes between the water column and the sediment bed. The physical processes involving the solids are settling, sedimentation and resuspension. settling is the downward movement of sediment particles due to their negative buoyancy. Sedimentation occurs once the settled particles reach the bottom and join the sediment bed, while resuspension is the process by which particles of the bed are entrained upward into the water column, usually by shear flow. Furthermore, diffusive exchanges, either molecular or turbulent and including adsorption/desorption, can occur between the water column and the sediment bed. Also, the bed solutes can be subjected to advection and diffusion. Bioturbation is the mixing of sediment by small organisms, usually worms, living in the upper layers of the sediment;

In this thesis, only topics referred to pollutant-water and air-water interaction are developed. Water-sediment interfaces will be studied in future.

The idea to adopt a Lagrangian particle model as Smoothed Particle Hydrodynamics (SPH) to simulate pollutant evolutions and environmental processes starts from the definition of Lagrangian point of view: *the fluid motion is described following the evolution of a particle, evaluating its variables in space and time*. To better clarify this definition, we can refer to the motion of a pollutant that determines the trajectory. Moreover, by the association of this concept with the fundamental similarity between the molecular dynamics and the Lagrangian methods, it was born the idea to deal with pollutant transport using Lagrangian models.

1.2 AN OVERVIEW ON PARTICLE AND MESHLESS METHODS

1.2.1 Eulerian vs. Lagrangian approach

Fluid mechanics has two basic ideas for the description of fluid flows: the Lagrangian and Eulerian approaches. In Lagrangian concept, the observation point moves with the fluid element, that is the observer moving with a velocity identical to the fluid element, while in the Eulerian concept, the observer keeps a fixed position without moving, with all the flow quantities as functions of positions and time. Analogously, Computational Fluid Dynamics (CFD) implementations are also classified as the Lagrangian method and Eulerian method. The latter has been well studied for more than fifty years and is broadly applied in many aspects of flow simulations. The Eulerian based approaches are the finite volume method (FVM), the finite difference method (FDM) and the finite element method (FEM). Several commercial software packages, such as STAR-CCM+, FLUENT, FLOW3D, ABAQUS, for instance, are providing solutions for engineering and hydrodynamic problems.

The Lagrangian approach has not been as widely used as the Eulerian one but it is becoming common in research. However, it offers a different possibility over the Eulerian approach. In practical applications, Eulerian based models are not suitable for problems involving large deformation and fragmentation of fluids. In Eulerian formulations it is very difficult and computationally expensive to accurately resolve free surfaces and track moving interfaces and boundaries as the problem evolves over the fixed mesh. Moreover, Lagrangian methods can better prescribe the physical phenomena due to the fundamental similarity with the molecular dynamics ([8], [9]).

Meshless numerical methods are those which attempt to solve these long standing problems of traditional mesh based approaches by providing a framework in which general Partial Differential Equations (PDEs) can be solved without the need for any underlying regular mesh or nodal connectivity. With no explicit mesh to generate the initial preprocessing time is reduced and the need for subsequent re-meshing is totally eliminated since mesh entanglement no longer occurs. In grid based schemes mesh adaptivity has been used to improve numerical results and reduce computation times. In this respect meshless methods show a great deal of promise. Adaptivity is easily implemented since nodes can be added or removed at will without the implications of mesh regeneration. Over the last thirty years research into the next generation of meshless numerical methods has gained considerable momentum and several different approaches have been developed. A number of good review papers, thesis and books are currently available which cover many of the recent developments in this field (see *e.g.* [10], [11], [12], [13], [14], [15]).

1.2.2 Some methods

The first particle models are the Marker And Cell (MAC) and Particle In Cell (PIC) which were developed in 1960's by Harlow (see [16], [17], [18]). Although these formulations still use a Eulerian mesh and the finite difference method for the solution of the Navier-Stokes equations they were the first to incorporate a set of Lagrangian 'marker' particles which move with the fluid. The main disadvantage of both these methods is the continual mapping of variables between the particles and the Eulerian mesh which introduces large amounts of dissipation.

The MAC method was originally developed to model confined, viscous, incompressible fluid flows ([17], [18]). In later applications to low viscosity flows the MAC method was found to be unstable and poorly capture free surfaces [19]. This was caused by both the simplified implementation of the boundary conditions and the method used to extrapolate the particle velocities from the Eulerian mesh. Later variations of the MAC method ([20], [19]) improved its accuracy and extended the boundary conditions to include curved and moving boundaries [21]. Similarly, the PIC method models the fluid as a set of Lagrangian particles moving through a fixed grid of cells ([22],[16]). In the original PIC formulation each particle is defined only by its position and mass. All other cell properties are calculated and updated by the transition of particles moving from one cell to another. It was found later that numerical dissipation could be reduced if the particles were assigned all fluid properties such as momentum and energy. With these improvements the PIC method has been successfully adapted to solve a variety of solid mechanics problems ([23], [24], [25]).

The Material Point Method (MPM) (see *e.g.* [26]), is an extension from the Particle-in-cell (PIC) Method in computational fluid dynamics to computational solid dynamics, and is a Finite element method (FEM)-based particle method. It is primarily used for multiphase simulations, because of the ease of detecting contact without inter-penetration. It can also be used as an alternative to dynamic FEM methods to simulate large material deformations, because there is no re-meshing required by the MPM.

In 1968, Shepard [27] presented a meshless interpolation for irregularly spaced data points. After introducing the Moving Least Square method by Lancaster and Salkauskas in 1981 [28], Nayroles et. al. [29], employed a local form of this approximation for numerical solution of some PDE's using nonsingular weight functions with compact support. In spite of disadvantage of having to find complete derivatives of their basis functions, they obtained acceptable results and named their method Diffuse Element Method (DEM). The DEM has the following properties: (1) locality of the finite element method; (2) increases degree of smoothing in the approximation; (3) avoids using time-consuming mesh generation process; (4) the basis function derivatives are not complete; (5) essential boundary conditions cannot be satisfied exactly and need another methods; (6) approximation is based on an irregular distribution of nodes; (7) smoothing degree of the approximation is directly depend on the smoothing degree of the weights.

In 1994, Belytschko et. *al.* [30] generalized the DEM and introduced Element Free Galerkin (EFG) method. Some of properties of the EFG method are: (1) high accuracy; (2) use of complete derivatives; and (3) relative to the DEM, the EFG method is computationally more expensive.

The Finite Volume Particle Method (FVPM) was first introduced by Hietel et *al.* [31]. Recent developments have been performed by Keck and Hietel ([32], [33]), Nestor et *al.* [34] and Teleaga [35]. In FVPMs, the fluid is represented by a set of particles, which in turn are associated with normalized, overlapping, compactly supported kernel functions. A test function is defined related to the particle volume. The particles are viewed as discrete volumes to which the integral form of the governing equations applies. The interaction between particles is calculated from the flux rate between neighbouring particles. The conservation law is ensured.

In the Finite Pointset Method (FPM) (see *e.g.* [36], [37], [38], [39]), all the points in the computing domain are only interpolation bases, without any relation to the physical properties of the fluid, such as density and volume. The first or second derivative of a hydrodynamic variable is obtained by minimizing the quadratic form of the error function which is built up from the Taylor expansion of the computing point value from the neighbouring points.

The Moving Particle Semi-implicit (MPS) method was developed by Koshizuka et *al.* [40] to simulate incompressible free-surface viscous flows particularly those with fluid fragmentation. The main feature of MPS method lies in the simplicity of its formulations and satisfaction of the fluid incompressibility. MPS deploys the original form of the weight function to approximate spatial derivatives of the Lagrangian Navier-Stokes by a deterministic particle interaction model. In MPS, incompressibility is presented by keeping the density of particles constant during computation time. The pressure term in momentum equations is determined by a Poisson equation.

In Vortex Methods (see *e.g.* [41]), the Navier-Stokes equations are expressed in vorticity formulation and the vorticity field becomes the principal variable for computation. The fluid velocity field is obtained from an integral of the vorticity, and the pressure is not explicitly solved for, as it is eliminated by the curl operator. Since vortex methods are characterized by a Lagrangian approach, fluid particles convect with the local fluid velocity at each time step. Vortex method are, obviously, very efficient for investigation of problems characterized by high vorticity zone.

1.3 SMOOTHED PARTICLE HYDRODYNAMICS: THE STATE-OF-ART

Smoothed Particle Hydrodynamics (SPH) was born about 30 years ago to solve gas-dynamics problems in open space, in particular polytropes (Lucy, 1977 [1]; Gingold and Monaghan, 1977 [2]). In astrophysics, a polytrope refers to a solution of the Lane-Emden equation in which the pressure is related to density via a constant known as polytropic index. For many years, the SPH method has been applied to problems in the astrophysical field, as documented in the review paper by Benz (1990) [3]. Hence, relevant improvements of the solver were achieved within that research area. During the last decades, the SPH method has been increasingly modified and extended to provide approximations to the PDEs in a wide range of scientific and engineering applications particularly in the hydrodynamic field. Monaghan [4] was the first to apply the SPH scheme to fluid-dynamics problems. The main steps leading to the current state-of-art of the SPH method are summarized here.

IMPROVEMENTS ABOUT EFFICIENCY, ROBUSTNESS, ACCURACY AND STABILITY OF SPH. Firstly, the efficiency of SPH was significantly improved by Hernquist and Katz (1989) [42] introducing a hierarchical algorithm to approximate the interactions between the particles located relatively far away from each other. As a result, in case of spatially persisting forces such as gravitational attractions among bodies, the cost of a computational step reduced. In their paper, Hernquist and Katz also provided a generalization of SPH method allowing a local refinement of the computational domain that could be performed where it was needed for example in areas where large gradients were expected. In 1994 Nelson and Papaloizou [43] discussed the SPH method with variable smoothing length and expressed the need for additional terms that had been neglected in the work by Hernquist and Katz [42], showing that such additional terms are essential for the conservation of energy especially during impact problems. Martel et *al.* (1994) [44] showed that an isotropic smoothing algorithm with spherical kernel would lead to poor results where considerable anisotropic volume changes are present. To handle this difficulty, they proposed a new version of SPH method, namely, the Adaptive SPH (ASPH) method. In the ASPH method, the isotropic kernel is replaced by an anisotropic kernel whose axes evolves automatically to follow the mean particle spacing as it varies in time and space. Although ASPH method may have better performance than the SPH method for the simulation of problems with anisotropic volume changes, its mathematical formulations are more complicated than those of the SPH method. In addition, more research is required to study the convergence, consistency, conservation and stability of ASPH formulations.

Stability is one of the most important aspects in all numerical computations. One of the most critical instabilities of the SPH method is the so-called *tensile instability* that mainly occurs in the situation where particles are under a certain tensile stress state. The tensile instability manifests itself as a clustering of the particles which may lead to unphysical results or even breakdown of calculation. By performing a Von Neumann stability analysis, Swegle et *al.* ([45] and [46]) concluded that tensile instability results from an effective stress emerging from a non-physical negative modulus being produced by the constitutive relation and the kernel interpolation. In other words, the kernel interpolation employed for spatial discretization changes the nature of original PDE. Starting from Swegle et *al.* ([45] and [46]) stability analysis criterion based on the second derivative of the kernel and the stress, it can be seen that such kind of instability can also occur in compression, not only tension. However, because of the characteristics of general kernel functions applied in SPH calculations, the instability is generally observed in tension and hence referred as tensile instability. Several remedies have been proposed to avoid such tensile instability. To remove the instability, Dyka et *al.* (1995) [47] proposed a so-called stress point method. The main idea of this approach is to add additional points when evaluating stresses of other state variables. Randles and Libersky (1996) [48] suggested certain dissipative terms which they call conservative smoothing. However, such approach is not always promising (Mandell et al., 1996) [49]. Monaghan (2000) [50] proposed an artificial pressure to provide a relatively small repulsive force in order to stabilize the computation.

Espanol and Revenga (2003) [51] presented a fluid particle model that was both a thermodynamically consistent version of smoothed particle hydrodynamics (SPH) and a version of dissipative particle dynamics (DPD), capturing the best of both methods. The model is a discrete version of

Navier-Stokes equations, like SPH, and includes thermal fluctuations, like DPD. This model solves some problems with the physical interpretation of the original DPD model.

Colagrossi et *al.* (2009) [52] provided an in-depth analysis of the theoretical structure of SPH for an inviscid, weakly compressible, and barotropic flow in the presence of a free surface. A detailed description of the free-surface influence on the smoothed differential operators was supplied. New and existing forms was analyzed in detail, in terms of convergence and conservation properties. The analysis was based on the principle of virtual works, which permits to exhibit the link with the enforcement of the dynamic free-surface boundary condition. Finally, possible SPH formulations resulting from this analysis was investigated, in terms of consistency, conservation, and dynamic free-surface boundary condition.

Vila (1999) [53] introduced a SPH model in Arbitrary Lagrangian Eulerian (ALE) formalism with Riemann solvers rewriting the SPH formalism in a way inspired by the Finite Volumes Formalism. Following this process, interaction between two particles can be seen as the result of a flux acting at the middle of the distance between the two particles.

A diffusive weakly-compressible SPH scheme was introduced by Antuono et al. (2010) [54] and subsequently called δ-SPH [55] [56]. It is characterized by a novel system of equations which contains diffusive terms in both the continuity and energy equations and, at the leading order, coincides with a standard weakly-compressible SPH scheme with artificial viscosity. A proper state equation is used to associate the internal energy variation to the pressure field and to increase the speed of sound when strong deformations/compressions of the fluid occur. The model has been tested using different free surface flows and it was clearly robust, efficient and accurate than standard SPH.

SPH FOR INCOMPRESSIBLE INVISCID FLOWS. Monaghan (1994) [4] was the first who applied the SPH method to simulate incompressible free-surface fluid flows. In his work, the fluid was considered as weakly (slightly) compressible so that the pressure field could be explicitly obtained from the density field by an appropriate equation of state. Weakly Compressible SPH (WCSPH) simulations are usually performed at a low Mach number leading to small fluctuations in density. The WCSPH method has been applied to simulate numerous free-surface fluid flows such as run-up and run-down of waves on beaches (Monaghan and Kos, 1999) [57], wave breaking (Landrini et *al.*, 2007 [58]; Monaghan et *al.*, 2004 [59]) and wave breaking and post-breaking on beaches (Dalrymple and Rogers, 2006 [60]). An alternative and favored approach to enforce the incompressibility in the SPH method is to apply a two-step projection method similar to that in the Moving Particle Semi-Implicit (MPS) method (Koshizuka et al., 1995 [40]). Based on this approach, Cummins and Rudman (1999)[61] proposed an Incompressible SPH (ISPH) method in which an intermediate velocity field is projected onto a divergence free space by solving a Poisson pressure equation derived from an approximate projection. Analogous to this SPH projection method, Shao and Lo (2003) [62] developed an ISPH method for the simulation of free surface hydrodynamic flows and successfully simulated several free-surface fluid flow problems such as wave overtopping (Shao et *al.*, 2006 [63]), wave-structure interaction (Gotoh et *al.*, 2004 [64]; Shao and Gotoh, 2004 [65]).

In order to solve the Poisson pressure equation, the ISPH needs the enforcement of explicit dynamics conditions at free surface. This requires an algorithm to detect the free surface both in two and three dimensions (see Marrone et *al.*, 2010 [66]; Dilts, 1999 [67]). Furthermore, this enforcement represents an disadvantage of ISPH with respect to WCSPH, in particular for 3D free surface. Conversely, to satisfying the fluid incompressibility, an advantage of ISPH to WCSPH is its independency from the speed of sound; thus, according to the required stability conditions (such as Courant condition) a larger computational time step would be allowed in ISPH calculations.

Ellero et *al.* (2007) [68] presented a smoothed particle hydrodynamic model for incompressible fluids where the incompressibility is achieved by requiring as a kinematic constraint that the volume of the fluid particles is constant. They used Lagrangian multipliers to enforce this restriction. These Lagrange multipliers play the role of non-thermodynamic pressures whose actual values are fixed through the kinematic restriction. The studied cases don't refer to free-surface problems.

SPH FOR VISCOUS LAMINAR FLOWS. The majority of SPH implementations employ an artificial viscosity initially introduced allowing to simulate strong shocks (Monaghan, 1992) [69]. The first introduction of a realistic viscosity term in a SPH-based calculation of Navier-Stokes equation was given by Takeda et *al.* (1994) [70]. The method was successfully applied to the 2D Poiseuille flow, to the 3D Hagen-Poiseuille flow, and to flow around a cylinder for Reynolds number ranging between 6 and 55. Still in the context of low Reynolds number flows, Morris et al. (1997) [71] calculated viscous stresses by a hybrid viscosity term that combines a standard SPH first derivative with a finite different approximation of first derivative. The authors verified their method by calculating Couette and Poiseuille flows and the flow passed through a regular lattice of cylinders.

Fang et *al.* (2009) [72] introduced improvements for the numerical simulation of free surface flows of viscous fluids. These are achieved by deriving a new set of general discrete SPH-like equations under an energy-based framework and applying a corrected (high-order) or coupled particle approximation scheme for function derivatives.

Nestor at al. (2009) [73] extended FVPM to viscous flows using a consistency - corrected smoothed particle hydrodynamics approximation to evaluate velocity gradients. The accuracy of the viscous FVPM is improved by a higher-order discretization of the inviscid flux combined with a second-order temporal discretization.

Colagrossi et *al.* (2010) [74] carried out a theoretical analysis on the performance, close to a free surface, of the most used SPH formulations for Newtonian viscous terms. Using a Taylor expansion, a reformulation of the SPH expressions for the viscous term in the momentum equation was undertaken which allows to characterize the behavior of the viscous term close to the free surface. Under specific flow conditions, the authors showed local singularity arise close to the free surface when spatial resolution is increased.

SPH FOR VISCOUS TURBULENT FLOWS. Welton (1998) [75] applied the SPH method within a Monte-Carlo probability density formulation to simulate turbulent flows. Wagner and Liu (2000) [76] applied the Reproducing Kernel Particle Method (RKPM) as a filter in their Large Eddy Simulation (LES) of turbulent flows. By applying the same concept of Sub-Grid-Scale turbulence modeling in grid-based methods to particle methods, Gotoh et *al.* (2001) [77] developed a Sub-Particle-Scale turbulence model for particle-based simulations of turbulent flows. By employing the SPS turbulence model, Gotoh et *al.* (2004) [64] performed an ISPH-LES simulation to study wave transmission and reflection by a half-immersed curtain breakwater. Good agreement was achieved in terms of both free-surface profile and turbulent eddy viscosity near the curtain wall.

In 2002, Monaghan [78] proposed a SPH version of the alpha turbulence model for compressible flow with a resolution that varies in space and time. The alpha model involves two velocity fields. One velocity field is obtained from the momentum equation, the other by averaging this velocity field as in the version of SPH called XSPH. Furthermore, Monaghan (2009) [79] presented a model similar to the Lagrangian averaged Navier Stokes alpha (LANS-alpha) turbulence model that satisfied different scaling laws while conserving energy, angular and linear momentum and circulation, though the latter is only conserved approximately.

Violeau and Issa (2007) [80] presented a review of developed turbulence models adapted to the SPH method, from the simplistic point of view of a one-equation model involving mixing length to more sophisticated (and thus realistic) models like explicit algebraic Reynolds stress models (EARSM) or large eddy simulation (LES).

SPH FOR MULTIPHASE FLOWS. Monaghan and Kocharyan (1995) [81] proposed a general SPH formulation for the simulation of multi-phase flows. The SPH capability to simulate weakly compressible multi-phase flows with small density differences is shown by Monaghan et *al.* (1999) [82]. However, when their approach is applied to simulate a multi-phase flow with large density differences as in case of air-water, severe instabilities develop along the interface. Colagrossi and Landrini (2003) [6] modified the spatial derivative approximation to diminish the effect of large density difference across the interface. As another remedy, Hu and Adams proposed a particle-averaged spatial derivative approximation and applied their multi-phase SPH method to simulate both weakly compressible (Hu and Adams, 2006) [83] and incompressible (Hu and Adams, 2007) [84] flows. Furthermore, a constant-density approach, which corrects intermediate density errors by adjusting the half-time-step velocity with exact projection, is proposed by Hu and Adams (2009) [85].

Tartakosky and Meakin (2005) [86] simulated unsaturated (multiphase) flow through fracture junctions. A combination of standard SPH equations with pair wise fluid-fluid and fluid-solid particle-particle interactions allowed surface tension and three-phase contact dynamics to be simulated.

Grenier et *al.* (2009) [5] proposed a formulation that is an extension of the one discussed in Colagrossi and Landrini (2003) [6] and is related to the one proposed by Hu and Adams (2006) [83] to study multi-fluid flows. The SPH scheme allows an accurate treatment of the discontinuity of quantities at the interface (such as the density), and permits to model flows where both interfaces and a free surface are present. The governing equations are derived following a Lagrangian variational principle leading to an Hamiltonian system of particles.

Adami et *al.* (2010) [87] introduced a novel surface-tension method for multi-phase SPH. With a new reproducing divergence approximation, the authors proposed a new formulation for the surface curvature and modify the color gradient summation with a density weighting.

SPH FOR DIFFUSION PHENOMENA. The modeling of diffusion processes by the SPH technique was first investigated by Cleary and Monaghan [88] referring to heat conduction problems. Other SPH modellings have been formulated to simulate diffusion phenomena in a spatially periodic porous media [89] [90], for miscible flow in fractures [91], and coupled with reactive transport and precipitation of a solute [92]. The use of the SPH method in the analysis of two-phase flows for advective diffusion processes has not been investigated. More recently a SPH diffusion modeling in the presence of a velocity field has been addressed to the simulation of the interaction between water and non-cohesive bed sediments [93].

Adami et al. (2010) [94] developed a method for simulating incompressible interfacial flows with surfactant dynamics. The surfactant transport model accounts for exchange between the bulk phase and the interface (adsorption, desorption, squeeze-out) as well as advection and diffusion on the interface and within the bulk phase. In the numerical scheme, the different transportation phenomena are considered simultaneously or separately, depending on the problem statement.

FREE-SURFACE BOUNDARY CONDITIONS IN SPH CONTEXT. Considering free-surface flows, the major advantage of the SPH method with respect to other numerical solvers is that it is not necessary to enforce explicitly the free-surface boundary conditions [52]. The kinematic condition is intrinsically incorporated in Lagrangian flow description. The dynamic condition is also automatically satisfied: due to one of the properties of the kernel function, the form of the discretized fluid momentum equation is such that the pressure is forced to vanish when approaching the free surface.

Within the SPH strategy it is also possible to model the surface tension at the free surface. Examples are given in Morris (2000) [95] and Nugent and Posch (2000) [96]. In the latter case, the surface tension is introduced by modifying the state equation. This approach is much easier than the technique by Morris (2000) and provide also a simple mechanism to control the numerical fragmentation of the interface. In the last decade, surface tension modellings was introduced by Colagrossi and Landrini (2003) [6], Hu and Adams (2006) [83], Grenier et *al.* (2009) [5], Adami et *al.* (2010) [87]; for further details see the section SPH FOR MULTIPHASE FLOWS in this paragraph.

Marrone et *al.* (2010) [66] defined a novel algorithm to detect the free-surface both in two and three dimensions. It is composed of two stages. The first stage consists in detecting the particles composing the free-surface. From this information, it is possible to define a level-set function throughout the domain in a second stage. This function can be used to interpolate flow quantities on a Cartesian grid, which makes possible the visualization and analysis of flow features using standard visualization tools.

SOLID BOUNDARY CONDITIONS IN SPH CONTEXT. As counterpart with respect to the free-surface conditions, the SPH has difficulties in handling the presence of solid boundaries. The first attempt to deal with solid walls was presented by Monaghan (1994) [4] modeling the body through boundary particles exerting forces on the fluid. This idea is based on the fact that, at micro scale, also body appears made of particles, *i.e.* atoms or molecules. The main drawbacks of such technique are: (i) it causes pressure-wave disturbances at the beginning of the numerical simulation and (ii) is not suitable to calculate accurately the local hydrodynamics loads induced on the structures.

Boundary conditions defined using ghost particles (Colagrossi and Landrini, 2003) [6] reproduce part of the computational fluid domain, which is close to the boundary at hand, symmetrically in a thin layer. Ghost particles present density, pressure and velocity deduced from the fluid particles. With this technique the local loads on the body can be calculated adequately. Attention has to be paid when dealing with the complex geometries structures.

Successively, Marrone et al. (2009) [97] proposed an enhanced treatment of the solid boundaries within two-dimensional SPH schemes. The solid boundary is modeled through fixed ghost particles firstly proposed for a simple flat profile by Fang et *al.* [98] and extended by Marrone et al. for a generic solid profile. Differently from the ghost particles that are instantaneous mirrors of the fluid particles with respect to the body surface, the position of the fixed ghost particles is fixed in the frame of reference of the body. The main advantage of using the fixed ghost particles instead of the ghost ones is that their distribution is always uniform and does not depend on the fluid particle positions. This allows a simple modeling of complex 2D geometries. Further, the use of an MLS interpolator [99] ensures an accurate mirroring procedure of the flow quantities.

De Leffe et *al.* (2009) [100] proposed a new boundary treatment for the SPH model in ALE formalism with Riemann solvers. The new technique has the capability to handle different kinds of boundary conditions (inflow, outflow, non-reflecting, free slip, etc.).

Ferrand et *al.* [101] presented a method analogous to Bonet et *al.*'s approach [102] that it is based on a geometrical parameter measuring the missing area in the kernel support when a particle is in the vicinity of a solid boundary, but improve accuracy for linear fields.

UPSTREAM/DOWNSTREAM BOUNDARY CONDITIONS IN SPH CONTEXT. The enforcement of upstream/downstream boundary conditions in SPH context is not trivial for particle methods. Conversely, in Lagrangian numerical approach, periodic conditions can be easily treated. With these, a particle that leaves the computational domain through an outflow boundary, re-enters the domain immediately through the inflow boundary. However, this method is useful just for academic problems.

Lastiwka et al. (2008) [103] presented a boundary condition implementation that enables the simulation of flow through permeable boundaries. Each permeable boundary is associated with an inflow or outflow zone outside the domain, in which particles are created or removed as required. The analytic boundary condition is applied by prescribing the appropriate variables for particles in an inflow or outflow zone, and extrapolating other variables from within the domain.

1.4 STRUCTURE OF THE THESIS

After the overview here presented on the meshless methods and SPH model, the thesis is structured as follows.

In Chapter 2, 3 and 4 theoretical aspects referring to the SPH interpolation technique, the discretized fluid mechanics equations and the new SPH formalism to model diffusion processes are introduced. The chapter 5 describes the main techniques for modeling solid boundaries. Furthermore, a novel algorithm for the enforcement of upstream and downstream boundary conditions based on inflow and outflow particles is presented. Chapter 6 and 7 refer to the simulations of dam breaks on sills and uniform and non-uniform steady open-channel flows. Chapter 8 and 9 deal with the simulations of two-phase pollutant (air)-water interaction and advective reactive diffusion phenomena. The conclusions are summarized in Chapter 10 and some research guide-lines for further developments are given.

Part I

Numerical Model: Smoothed Particle Hydrodynamics

2 MESHLESS OPERATORS IN LAGRANGIAN METHODS

CONTENTS

2.1 Integral interpolation techniques 15
2.2 Types of kernel functions 18
2.3 Neighbours search strategy 20
  2.3.1 Linked list 20

In this chapter, some significant meshless tools applied in the SPH computations are discussed. After the description of the integral interpolation techniques used to evaluate a physical variable, the types of kernel functions and the algorithm to search the neighbor particles are introduced.

2.1 INTEGRAL INTERPOLATION TECHNIQUES

A nonlinear fluid problem is governed by Partial Differential Equation (PDE) system. On the basis of the Lagrangian meshless approach there is the idea that the fluid can be modeled as a finite number N of particles, each one with its local mass and other physical properties. Following the evolution of those particles, the PDEs are solved considering the information they carry to reconstruct the fluid properties everywhere in the domain.

Being f a generic variable, the equations of fluid dynamics have the form

$$\frac{Df}{Dt} = \mathcal{F}\left(f, \nabla f, \mathbf{r}\right) \tag{2.1}$$

where

$$\frac{D}{Dt} = \frac{\partial}{\partial t} + \mathbf{u} \cdot \nabla \tag{2.2}$$

is the Lagrangian derivative, or the derivative following the motion, being $\mathbf{u}$ the velocity vector. It is worth noting that the characteristics of this differential operator are the particle trajectories.

In the equations of fluid dynamics, the rates of change of physical quantities require spatial derivatives of physical quantities. The key step in any computational fluid dynamics algorithm is to approximate these derivatives using information from a finite number of points. In finite difference methods, the points are the vertices of a mesh. In the SPH method, the interpolating points are particles which move with the flow, and the interpolation of any quantity, at any point in space, is based on kernel estimation.

SPH interpolation of the variable f, which is a function of the spatial coordinates, is based on the integral interpolant

$$\langle f(\mathbf{r})\rangle = \int_{\Omega} f(\mathbf{r}')W\left(\mathbf{r}-\mathbf{r}';\epsilon\right) dV' \tag{2.3}$$

where $\mathbf{r}$ is the position where f is evaluated by interpolating its known values in $\mathbf{r}'$ over the domain Ω. In Equation (2.3), $W\left(\mathbf{r}-\mathbf{r}';\epsilon\right)$ is a weight function and ϵ is a measure of the support of W, *i.e.* where W differs from zero. Physically, ϵ is also representative of the domain of influence $\Omega_{\mathbf{r}'}$ of $\mathbf{r}'$. In the SPH framework, $W\left(\mathbf{r}-\mathbf{r}'\right)$ is called *smoothing function* or *kernel*, and has the following properties:

- $W\left(\mathbf{r}-\mathbf{r}'\right) \geqslant 0$ for $\mathbf{r} \in \Omega_{\mathbf{r}'} \subset \Omega$ and zero otherwise.
- $\int_{\Omega} W\left(\mathbf{r}-\mathbf{r}';\epsilon\right) dV' = 1$.
- $W\left(\mathbf{r}-\mathbf{r}';\epsilon\right)$ decrease monotonously as $\parallel \mathbf{r}-\mathbf{r}' \parallel$ increases.
- $\nabla_{\mathbf{r}} W\left(\mathbf{r}-\mathbf{r}';\epsilon\right) = -\nabla_{\mathbf{r}'} W\left(\mathbf{r}-\mathbf{r}';\epsilon\right)$ symmetric property, W is an even function.

A sketch of the kernel function is reported in Figure 1.

For $\epsilon \to 0$, the kernel function W becomes a Dirac delta function, and therefore

$$\lim_{\epsilon\to 0} \int_{\Omega} f(\mathbf{r}')W\left(\mathbf{r}-\mathbf{r}';\epsilon\right) dV' \equiv f(\mathbf{r}).$$

The approximations of the derivatives of the field f can be deduced by

$$\nabla f(\mathbf{r}) \simeq \langle \nabla f(\mathbf{r}')\rangle = \int_{\Omega} \nabla f(\mathbf{r}')W\left(\mathbf{r}-\mathbf{r}';\epsilon\right) dV'. \tag{2.4}$$

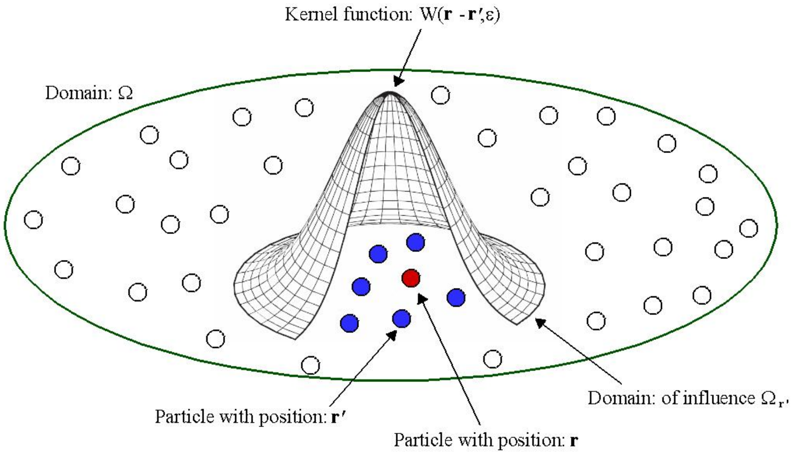
Kernel function: W(**r** -**r**',ε)
Domain: Ω
Particle with position: **r'**
Particle with position: **r**
Domain: of influence Ω_r'

Figure 1: Sketch of the kernel function.

The integration by parts of (2.4) gives:

$$\begin{aligned}\langle\nabla f(\mathbf{r}')\rangle =& \int_{\partial\Omega} f(\mathbf{r}')W\left(\mathbf{r}-\mathbf{r}';\epsilon\right)\mathbf{n}dS'+\\ &-\int_{\Omega} f(\mathbf{r}')\nabla_{\mathbf{r}'}W\left(\mathbf{r}-\mathbf{r}';\epsilon\right)dV'.\end{aligned} \tag{2.5}$$

The surface contribution in (2.5) is negligible inside the domain. Therefore, ignoring this term, the approximations for any derivative of the field f can be expressed only by the derivatives of the kernel W:

$$\begin{aligned}\langle\nabla f(\mathbf{r}')\rangle &= -\int_{\Omega} f(\mathbf{r}')\nabla_{\mathbf{r}'}W\left(\mathbf{r}-\mathbf{r}';\epsilon\right)dV'\\ &= \int_{\Omega} f(\mathbf{r}')\nabla_{\mathbf{r}}W\left(\mathbf{r}-\mathbf{r}';\epsilon\right)dV'.\end{aligned} \tag{2.6}$$

In the last integral, the symmetric property of the kernel W has been used. The choice of the smoothing function affects both the CPU requirements and stability properties of the scheme in the computations.

To apply this interpolation to a fluid, we divide it into a set of small mass elements. The element a will have a mass m_a, density ρ_a and position $\mathbf{r}_a$. The value of f at particle a is denoted by f_a. The interpolation integral can be written as

$$\int_{\Omega}\frac{f(\mathbf{r}')}{\rho(\mathbf{r}')}\rho(\mathbf{r}')dV' \tag{2.7}$$

where an element of mass is $\rho dV'$. The integral can then be approximated by a summation over the mass elements. This gives the summation interpolant

$$\langle f_a\rangle = \sum_b \frac{f_b}{\rho_b} m_b W_b(\mathbf{r}_a) \tag{2.8}$$

where $W_b(\mathbf{r}_a) = W(\mathbf{r}_a - \mathbf{r}_b;\epsilon)$. The summation is over all the particles but, in practice, it is only over near neighbours because W falls off rapidly with distance. In practice, we choose kernels which have compact support, i.e. they vanish at a finite distance.

The SPH formulation allows derivatives to be estimated easily. If W is a differentiable function (2.8) can be differentiated exactly to give

$$\langle\nabla f(\mathbf{r}_a)\rangle = \sum_b m_b\frac{f_b}{\rho_b}\nabla W_b(\mathbf{r}_a) \tag{2.9}$$

In SPH the derivative is, therefore, found by an *exact derivative* of an approximate function. However, this form of the derivative does not vanish if f is constant. A simple way to ensure that it does vanish if f is constant is to write

$$\langle \nabla f \rangle = \frac{1}{\Phi} \left(\nabla(\Phi f) - f \nabla \Phi \right) \tag{2.10}$$

where Φ is any differentiable function. The SPH form of (2.10) is

$$\langle \nabla f(\mathbf{r}_a) \rangle = \frac{1}{\Phi_a} \sum_b m_b \frac{\Phi_b}{\rho_b} \left(f_b - f_a \right) \nabla W_b(\mathbf{r}_a) \tag{2.11}$$

which vanishes if f is constant. Changing Φ it is possible to derive different formulation of the derivatives. For example, choosing $\Phi = 1$ gives

$$\langle \nabla f(\mathbf{r}_a) \rangle = \sum_b \left(f_b - f_a \right) \nabla W_b(\mathbf{r}_a) \Delta V_b \tag{2.12}$$

being $\Delta V_b = m_b / \rho_b$. Choosing $\Phi = \rho$

$$\langle \nabla f(\mathbf{r}_a) \rangle = \frac{1}{\rho_a} \sum_b m_b \left(f_b - f_a \right) \nabla W_b(\mathbf{r}_a) \tag{2.13}$$

The Equations (2.12) and (2.13) will be used in Chapter 3 in order to discretize the Fluid Mechanics Equations.

As in the case of first derivatives, second derivatives can be estimated by differentiating an SPH interpolant twice. For example, the second derivative of the variable f at the position of particle a can be estimated by

$$\langle \nabla^2 f(\mathbf{r}_a) \rangle = \sum_b m_b f_b \nabla^2 W_b(\mathbf{r}_a) \tag{2.14}$$

This equation will be applied and developed in Chapter 4 in order to discretize the diffusion equation.

2.2 TYPES OF KERNEL FUNCTIONS

A first class of kernel is given by Gaussian functions such as:

$$W(s, \epsilon) = \frac{\sigma}{\epsilon^\lambda} e^{-(s/\epsilon)^2} \tag{2.15}$$

where λ indicates the dimensions number of the treated problem and σ is the normalization factor, $\sigma = \left[\frac{1}{\pi}; \frac{1}{\pi\sqrt{\pi}} \right]$ in 2D and 3D simulations respectively. This function has the advantage to be infinitely differentiable and therefore has good stability properties [104]. Furthermore, a cut-off radius δ with relating renormalized coefficient is introduced in order to reduce computing costs. This leads to the "modified" Gaussian kernel

$$W(s, \epsilon, \delta) = \frac{e^{(s/h)^2} - e^{(\delta/h)^2}}{2\pi \int_0^\delta s \left(e^{(s/h)^2} - e^{(\delta/h)^2} \right) ds}. \tag{2.16}$$

This kernel has the compact support of size 3ϵ. It is used in the simulations in Chapter 8.

Another function, introduced by Johnson et *al.* [105], has the general formulation written as follows:

$$W(s,\epsilon) = \frac{\sigma}{\epsilon^{\lambda}}\left(\frac{3}{8}s^2 - \frac{3}{2}s + \frac{3}{2}\right) \qquad \text{if} \qquad 0 \leqslant s \leqslant 2 \tag{2.17}$$

with normalization factor, $\sigma = \left[\frac{1}{\pi}; \frac{15}{64\pi}\right]$ in 2D and 3D simulations respectively.

One of the most used kernel is the cubic spline proposed by Monaghan and Lattanzio [106], which has a low CPU time. This kernel can be approximated by:

$$W(s,\epsilon) = \frac{\sigma}{\epsilon^{\lambda}}\begin{cases} 4 - 6s^2 + 3s^3 & \text{for} \quad 0 \leqslant s \leqslant 1 \\ \left(2 - s^2\right)^3 & \text{for} \quad 1 < s \leqslant 2 \\ 0 & \text{otherwise} \end{cases} \tag{2.18}$$

with normalization factor, $\sigma = \left[\frac{10}{7\pi}; \frac{1}{\pi}\right]$ in 2D and 3D simulations respectively. This kernel has a compact support of size 2ϵ. This kernel is used in the simulations in Chapter 6 and 7.

By increasing the smoothing length to 3ϵ it is possible to define another kernel that is the quintic spline:

$$W(s,\epsilon) = \frac{\sigma}{\epsilon^{\lambda}}\begin{cases} (3-s)^5 - 6(2-s)^5 + 15(1-s)^5 & \text{for} \quad 0 \leqslant s \leqslant 1 \\ (3-s)^5 - 6(2-s)^5 & \text{for} \quad 1 < s \leqslant 2 \\ (3-s)^5 & \text{for} \quad 2 < s \leqslant 3 \\ 0 & \text{otherwise} \end{cases} \tag{2.19}$$

with normalization factor $\sigma = \left[\frac{7}{478\pi}; \frac{1}{120\pi}\right]$ in 2D and 3D simulations respectively [109]. This kernel gives the same results of the renormalized Gaussian Kernel (2.16) but needs more CPU time.

Another class of positive, definite and compactly supported radial functions was introduced by Wendland [107], that are defined as:

$$W(s,\epsilon) = \frac{\sigma}{\epsilon^{\lambda}}(1-s)^{\lambda+1}(\lambda+1)(s+1) \qquad \text{if} \qquad 0 \leqslant s \leqslant 3 \tag{2.20}$$

with $s = r/3\epsilon$ and normalization factor $\sigma = \left[\frac{5}{9\pi}, \frac{7}{18\pi}\right]$ in 2D and 3D dimensions respectively. The Wendland radial basis functions in 2D and 3D are quartic and quintic spline weight functions respectively.

The comparisons between the considered kernel functions have been identified the form (2.16) as the one leading to the best stability properties [109]. The choice of kernel has been motivated by the fact that from a numerical point of view the behavior of the renormalized Gaussian kernel is almost identical to the classical Gaussian kernel (the maximum error between the two kernels is less than $4 \cdot 10^{-4}$) [113]. For what concerns the latter one the following properties are well established: (i) among ten tested kernel shapes, the Gaussian kernel appears to give the best numerical accuracy in the stable field [108]; (ii) it presents also a lower computational cost with respect to evolved forms of spline kernels [11]; finally, (iii) its gradient can be straightforwardly obtained from the evaluation of W itself.

2.3 NEIGHBOURS SEARCH STRATEGY

Because of the neighbour particles searching at every time step, SPH numerical model needs great computational time. In order to reduce this computational time, several numerical techniques have been proposed to optimize the definition of the interacting neighbors of each particle of the fluid domain: Figure 2 shows the neighbors (black particles) of the particle at hand. In the followings two of the most successful SPH optimizing techniques will be introduced.

2.3.1 Linked list

The principal idea of linked list, or *Verlet* list, methods is to reduce the neighbor search algorithm by setting the particles in an ordered grid, characterized by a grid cell size equal to the size of the kernel support, as sketched in Figure 3 where a 2ϵ kernel support is considered as example. In this way, it is clear that each particle interacts at least with particles of

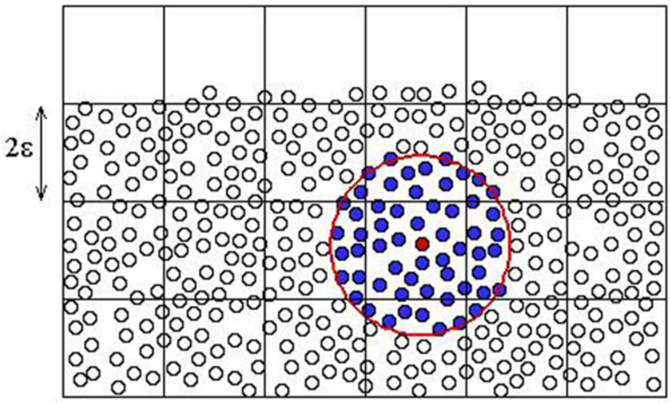

Figure 2: Particle interaction in the SPH model: neighbors particles of a given particle.

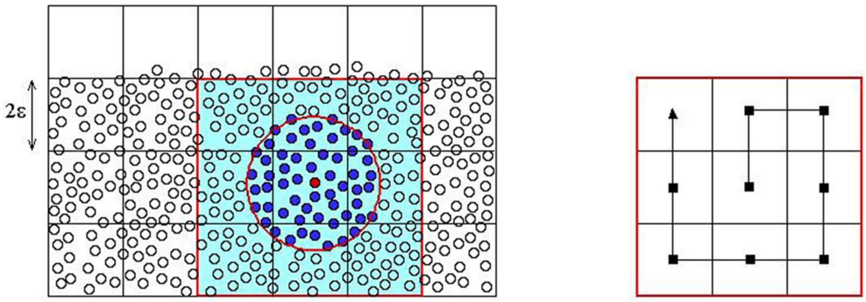

Figure 3: Particle grid cells in the fluid domain (on the left) and linked list through neighbors grid cells (on the right).

the same grid cell, and at most with particles placed in the eight adjacent grid cells, as it is shown in the left panel of Figure 3. So that, a linked list algorithm consists of searching neighbors particles looking at the eight grid cells around the cell at hand: the right panel of Figure 4 shows one of the possible way to look at the neighbors cells.

An optimization of this method is obtained by employing the action-reaction principle, according to which each interaction value A between a couple of particles a and b could be defined as $f_{ab} = -f_{ba}$, as the value of the kernel W is a function only of the distance between particles. So, the basic idea is to compute only once W_{ab} between two particles. This can be attained taking into account grid cells by a main direction over the grid. In this optic it is sufficient to look only at five of the grid cells of the previously defined linked list, as it is shown in Figure 4, while all interaction values have to be stored in dedicated vectors, with a small wasting of memory. In this example, the five neighbors cells are placed around the right upper corner of the cell at hand, so the main direction according to which grid cells have to be considered starts from the left bottom corner of the computational domain, going to the right upper corner.

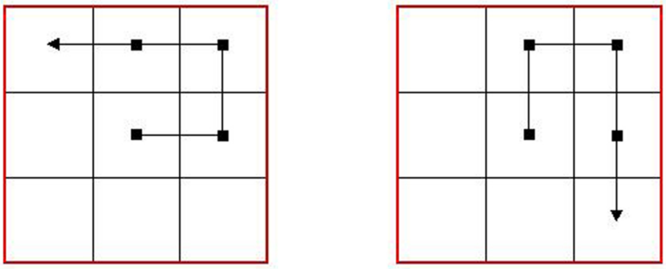

Figure 4: Reduced linked list algorithm over five grid cells.

3 FLUID MECHANICHS EQUATIONS IN SPH CONTEXT

CONTENTS

3.1 Governing equations in Fluid Mechanics 23
3.2 SPH discrete formalism of Fluid Mechanics Equations 24
  3.2.1 Continuity Equation 24
  3.2.2 Momentum Equation 25
  3.2.3 State Equation 26
  3.2.4 Numerical recipes for the code effectiveness 27
3.3 Two-phase SPH discrete formalism (Grenier et al., 2009) 29
3.4 Summarizing continuity and momentum equations used for the simulations 31
3.5 Time integration for Fluid Mechanics Equations 32

The chapter describes the governing equations of the Fluid Mechanics field, presenting different discrete Lagrangian forms derived by the interpolations techniques introduced in Chapter 2.

3.1 GOVERNING EQUATIONS IN FLUID MECHANICS

The equations governing the studied phenomena are the continuity and the momentum equations. Considering a weakly compressible medium these equations are coupled to the state equation.

The continuity equation defines the rate of change of the density related to the divergence of the velocity:

$$\frac{D\rho}{Dt} = -\rho\nabla\cdot\mathbf{u} \tag{3.1}$$

where $\mathbf{u}$ and ρ are the velocity of a generic material point and its density. This equation can be written also as follows [109]:

$$\frac{D\rho}{Dt} = -\rho\left[\frac{\nabla\cdot(\rho\mathbf{u}) - \mathbf{u}\cdot\nabla\rho}{\rho}\right] \tag{3.2}$$

The momentum conservation equation for a inviscid fluid (Euler equation) is:

$$\frac{D\mathbf{u}}{Dt} = -\frac{1}{\rho}\nabla p + \mathbf{g} \tag{3.3}$$

where p is pressure of a generic material point and $\mathbf{g}$ represents the mass force acting on the fluid.

The equation (3.3) can be rewritten considering the pressure gradient as function of density:

$$\frac{D\mathbf{u}}{Dt} = -\left[\nabla\left(\frac{p}{\rho}\right) + \frac{p}{\rho^2}\nabla\rho\right] + \mathbf{g} \tag{3.4}$$

For a viscous fluid the momentum equation is:

$$\frac{D\mathbf{u}}{Dt} = -\frac{1}{\rho}\nabla p + \mathbf{g} + \frac{1}{\rho}\nabla \cdot \mathbb{V} \tag{3.5}$$

where $\mathbb{V}$ is the viscous stress tensor.

3.2 SPH DISCRETE FORMALISM OF FLUID MECHANICS EQUATIONS

Here, we introduce different SPH discrete forms of Fluid Mechanics Equations based on the interpolations equations (2.12) and (2.13) expressed in Chapter 2.

3.2.1 Continuity Equation

Several expressions can be used to model the continuity equation. Starting from the interpolation relation (2.12), we can have the following equation:

$$\frac{D\rho_a}{Dt} = -\rho_a \sum_{b}^{N} (\mathbf{u}_b - \mathbf{u}_a) \cdot \nabla W_b(\mathbf{r}_a)\Delta V_b \tag{3.6}$$

where the sub-indexes indicate the quantities associated with the a-th and b-th particles. The symbol ΔV_b is the b-th particle volume that is $\Delta V_b = m_b/\rho_b$ and m_b is the b-th particle mass (constant during the flow evolution). Furthermore, $W_b(\mathbf{r}_a)$ represents the kernel centered at the b-th particle position and evaluated at the a-th particle position and ∇ denotes the gradient taken with respect to the coordinates of particle a.

Considering the interpolation relation (2.13), the continuity equation is:

$$\frac{D\rho_a}{Dt} = -\sum_{b}^{N} m_b (\mathbf{u}_b - \mathbf{u}_a) \cdot \nabla W_b(\mathbf{r}_a)\,. \tag{3.7}$$

If (3.6) is compared with (3.7) it will be seen that the former involves ρ explicitly in the summation, whereas the latter does not. Both expressions vanish, as they should, when the velocity is constant. However, when the system involves two or more fluids with large density ratios in contact, the expression (3.6) with ρ in the summation is more accurate (see Colagrossi and Landrini, 2003 [6]). The reason is that near an interface the summation for $\nabla \cdot \mathbf{u}$ for one type of fluid SPH particle involves contributions from the other fluid. If we imagine the other fluid being changed for a fluid with exactly the same velocity field, and exactly the same particle positions but different density, we would still want the same estimate of $\nabla \cdot \mathbf{u}$. However, with (3.7) the mass elements will be changed and the estimate will be different, but if (3.6) is used the ratio of mass to density will be constant and $\nabla \cdot \mathbf{u}$ will not change. In practice, it turns out that either (3.6) or ((3.6) can be used for density ratios $\leqslant 2$, but for larger density ratios it is better to use (3.6). The Lagrangian approach, which we consider later, requires that these equations for the rate of change of density with time be included as constraints. As a result, the form of the pressure forces changes with the form chosen for the density convergence equation.

3.2.2 Momentum Equation

Considering the interpolation relation (2.12) the momentum equation in Euler form (3.3) can be assume the following discrete fashion:

$$\frac{D\mathbf{u}_a}{Dt} = -\frac{1}{\rho_a} \sum_b^N \left(p_a + p_b\right) \nabla W_b(\mathbf{r}_a) \Delta V_b + \mathbf{g}_a \tag{3.8}$$

while adopting the interpolation relation (2.13), the momentum equation is:

$$\frac{D\mathbf{u}_a}{Dt} = -\sum_b^N m_b \left(\frac{p_a}{\rho_a^2} + \frac{p_b}{\rho_b^2}\right) \nabla W_b(\mathbf{r}_a) + \mathbf{g}_a \, . \tag{3.9}$$

As regard as the Navier-Stokes momentum equation (3.5), the discrete form of the viscous term is:

$$\nabla \cdot \mathbb{V} = \mu \sum_b \frac{8\left(\mathbf{u}_b - \mathbf{u}_a\right) \cdot \mathbf{r}_{ba}}{\|\mathbf{r}_{ab}\|^2} \nabla_a W_b(\mathbf{r}_a) \Delta V_b \tag{3.10}$$

where $\mathbf{r}_{ab} = -\mathbf{r}_{ba} = \mathbf{r}_a - \mathbf{r}_b$ and μ is the dynamic viscosity.

In many simulations the real viscosity term $\nabla \cdot \mathbb{V}$ is replaced by an artificial one $\nabla \cdot \mathbb{V}^\alpha$ tuned by the dimensionless parameter α. The use of the artificial viscosity is needed for reasons of stability (see *e.g.* [110]).

This artificial viscosity term is proposed by Monaghan [4] and it is:

$$\nabla \cdot \mathbb{V}^\alpha = m_b \prod_{ab} \nabla_a W_b(\mathbf{r}_a) \tag{3.11}$$

where:

$$\prod_{ab} = \begin{cases} \frac{-\alpha \bar{c}_{ab} \xi_{ab} + \beta \xi_{ab}^2}{\bar{\rho}_{ab}} & \text{if} \quad (\mathbf{u}_a - \mathbf{u}_b) \cdot \mathbf{r}_{ab} < 0 \\ 0 & \text{otherwise} \end{cases} \tag{3.12}$$

where $\xi_{ab} = \frac{\epsilon(\mathbf{u}_a - \mathbf{u}_b)\cdot \mathbf{r}_{ab}}{\mathbf{r}_{ab}^2 + \eta^2}$, $\bar{\rho}_{ab} = \frac{\rho_a + \rho_b}{2}$, $\bar{c}_{ab} = \frac{c_a + c_b}{2}$, c_a and c_b are, respectively, the sound speed of particles a and b, $\eta^2 = 0.01\epsilon^2$, and α and β are constants dependent on the type of simulation performed. In hydraulic applications, α assumes values in the range $[0.01 - 0.1]$ and β is set equal to 0 [4]. For $\epsilon \rightarrow 0$ the viscosity vanishes and the Euler equation is recovered.

A variant form of viscosity term is adopted by Antuono et *al.* [54]:

$$\nabla \cdot \mathbb{V}^{\alpha} = \alpha \epsilon c_0 \rho_0 \sum_b \frac{(\mathbf{u}_b - \mathbf{u}_a)\cdot \mathbf{r}_{ba}}{\|\mathbf{r}_{ab}\|^2} \nabla_a W_b(\mathbf{r}_a)\, \Delta V_b \qquad (3.13)$$

where $\alpha > 0.01$. In free-surface context, the use of this term instead (3.11) gives a less CPU cost and an easily direct calculation of numerical Reynolds number $Re = 0.125\alpha\epsilon c_0 \rho_0$.

3.2.3 State Equation

In the present SPH modeling, the fluid flow is considered weakly compressible in order to avoid solving the Poisson equation for incompressible fluids at each time step. A state equation is adopted to evaluate the pressure, p_i, as a function of density. In particular the Tait's equation is often used [111]:

$$p_a = B\left[\left(\frac{\rho_a}{\rho_0}\right)^{\gamma} - 1\right] \qquad (3.14)$$

where γ is the polytropic index of fluid, ρ_0 is the initial density and B is a constant chosen to make sure the Mach number $Ma = u/c$ is small enough to avoid fast sound waves which would require small time steps. B is defined considering that the Mach number has to be $Ma < 0.2$. In the simulations of the present work, the Mach number was set $Ma = 0.1$. According to the definition of the sound speed under constant entropy, it is possible to write:

$$c_a^2 = \frac{\partial p}{\partial \rho} = \frac{\gamma B}{\rho_0}\left(\frac{\rho_a}{\rho_0}\right)^{\gamma - 1} \qquad (3.15)$$

and, in initial conditions, the constant $B = c_0^2 \rho_0/\gamma$.

The value of the initial sound speed c_0 is evaluated as a function of a representative depth of the case to be simulated [4].

SPH computations has two constraints to impose c_0. As discussed by [112], the value of the initial sound speed c_0 can be evaluated as representative depth h of the case to be simulated [4] $c_0 > 10\sqrt{gh}$ and also as a function of maximum velocity $c_0 = 10U_{max}$.

Another kind of state equation permits a direct link between pressure and density

$$p_a = c_0^2(\rho_a - \rho_0) \qquad (3.16)$$

This equation is a linearization of (3.14) [54] that gives good results for hydrodynamics problems and reduces computing costs. The use of the equation (3.14) instead the equation (3.16) induces generally a very weak influence on the results (see *e.g.* [113]).

3.2.4 Numerical recipes for the code effectiveness

To improve the stability properties and, in general, the performances of the code, the following numerical recipes have been used.

XSPH velocity correction

To regularize the velocity field and the weakly - compressible treatment of liquids, the motion equation (see §3.2.2) has been replaced in the implementation by:

$$\frac{D\mathbf{r}_a}{Dt} \simeq \mathbf{u}_a + \Delta\mathbf{u}_a = \langle \mathbf{u}_a \rangle. \tag{3.17}$$

The so-called XSPH velocity correction $\Delta\mathbf{u}_a$ was introduced firstly by Monaghan [4], and takes into account the neighbor velocities through a mean velocity evaluated within the particle support, *i.e.*

$$\Delta\mathbf{u}_a = \frac{\epsilon_X}{2} \sum_b \frac{m_b}{\bar{\rho}_{ab}} (\mathbf{u}_b - \mathbf{u}_a) W_b(\mathbf{r}_a) \qquad \bar{\rho}_{ab} = \frac{\rho_a + \rho_b}{2} \tag{3.18}$$

In problems investigated, the (3.18) can be simplified as [97]:

$$\Delta\mathbf{u}_a = \frac{\epsilon_X}{2} \sum_b (\mathbf{u}_b - \mathbf{u}_a) W_b(\mathbf{r}_a) \Delta V_b \tag{3.19}$$

The corrected velocity $\langle \mathbf{u}_a \rangle$ is used only in the density and position evolution equations, not in the momentum equation. Typical value used for ϵ_X is 0.5.

Density re-initialization

In the SPH method, each particle has a fixed mass m_b and, if the number of particles is constant, mass conservation is intrinsically satisfied. On the other hand, by using the continuity equation (see §3.2.1), we cannot enforce exactly the consistence between mass, density and occupied area (see [3], [69] and [71]) as it would be possible by using

$$\rho_a = \sum_b m_b W_b(\mathbf{r}_a). \tag{3.20}$$

To alleviate this problem, the density field is periodically re-initialized by applying equation (3.20). In this procedure, special attention has to be paid to the used kernel. In fact, if $\sum_b W_{ab} \neq 1$ at point $\mathbf{x}_a$, the use of 3.20 would introduce additional errors. In particular, this happens when approaching any boundary of the fluid domain (free surface, interfaces between phases) [5]. In these cases, indeed, the number of particle neighbors seen by a boundary particle is lower, consequently the density computed is smaller than the original value. The equation of state would therefore predict a wrong pressure value and the entire field would be progressively corrupted [4]. Here such numerical errors have been overcome by using a more precise interpolation technique to re-initialize the density field, *i.e.* $\rho_a \simeq \langle \rho_a \rangle$, as

$$\langle \rho_a \rangle = \sum_b m_b W_b^{MLS}(\mathbf{r}_a) \tag{3.21}$$

In particular, the moving-least-square kernel W_b^{MLS} is computed by adopting the first-order accurate interpolation scheme on irregularly - scattered points proposed by Belytschko *et al.* [114].

Introducing a linear operator $\beta(\mathbf{r}_a)$ [67], the modified Kernel $W_b^{MLS}(\mathbf{r}_a)$ is expressed as

$$\begin{aligned} &W_b^{MLS}(\mathbf{r}_a) = \\ &[\beta_0(\mathbf{r}_a) + \beta_1(\mathbf{r}_a)(x_b - x_a) + \beta_2(\mathbf{r}_a)(y_b - y_a)]\, W_b(\mathbf{r}_a) \end{aligned} \tag{3.22}$$

The evaluation of $\beta_0(\mathbf{r}_a)$, $\beta_1(\mathbf{r}_a)$ and $\beta_2(\mathbf{r}_a)$ needs the solution of 3×3 linear algebraic problem for each particle:

$$\mathbf{A}_{ab} := \sum_b \Theta W_b(\mathbf{r}_a) \Delta V_b$$

where

$$\Theta = \begin{bmatrix} 1 & x_b - x_a & y_b - y_a \\ \dots & (x_b - x_a)^2 & (x_b - x_a)(y_b - y_a) \\ symm & \dots & (y_b - y_a)^2 \end{bmatrix}$$

and

$$\mathbf{A}_{ab} \begin{bmatrix} \beta_0(\mathbf{r}_a) \\ \beta_1(\mathbf{r}_a) \\ \beta_2(\mathbf{r}_a) \end{bmatrix} = \begin{bmatrix} 1 \\ 0 \\ 0 \end{bmatrix} \tag{3.23}$$

During the simulations the density re-initialization procedure is applied every, say, υ time-steps and increases slightly the computing time, mainly because of the inversion of the symmetric 3×3 (in 2D) matrix $\mathbf{A}$ for each a-th fluid particle; $\mathbf{A}$ is a symmetric 5×5 matrix in 3D. On the other hand, not only the consistency between mass, density and occupied area is restored, but (i) a more regular pressure distribution can be obtained, and (ii) the total energy is better conserved when artificial viscosity is used in the computations. Test cases showed that a good compromise between efficiency and effectiveness is achieved by enforcing the re-initialization every $\upsilon = 20$ time-steps [6].

3.3 TWO-PHASE SPH DISCRETE FORMALISM (GRENIER ET AL., 2009)

Here the Grenier et *al.* [5] model for two-phase flows is illustrated. It is an extension of the formulation discussed in Colagrossi and Landrini [6] and it is based on the Lagrangian variational approach introduced by Bonet and Lok [115]. In this context the motion equation can be characterized by a surface tension term.

The density is evaluated using a Shepard Kernel [114]:

$$\begin{cases} \rho_a = \sum_{b \in X} m_b W_b^S(\mathbf{r}_a); \\ \\ W_b^S(\mathbf{r}_a) = \dfrac{W_b(\mathbf{r}_a)}{\sum_{k \in X} W_k(\mathbf{r}_a)\Delta V_k}; \qquad \forall \mathbf{r} \in X \end{cases} \tag{3.24}$$

The summation in the second equation of the system (3.24) is extended only to the particles belonging to the fluid X containing the particle a.

The continuous momentum equation is

$$\frac{D\mathbf{u}}{Dt} = -\frac{1}{\rho}\nabla p + \mathbf{g} + \frac{1}{\rho}\nabla \cdot \mathbb{V} + \frac{1}{\rho}\mathbb{F}_S \tag{3.25}$$

where $\mathbb{F}_s$ represents the surface tension forces.

Being $\Gamma_a = \sum_a W_a(\mathbf{r}_b)\Delta V_a$ and $\Gamma_b = \sum_b W_b(\mathbf{r}_a)\Delta V_b$, a new discrete formula for the smoothed pressure gradient Grenier et *al.* [5] is introduced:

$$\nabla p_a = \sum_b^N \left(\frac{p_a}{\Gamma_a} + \frac{p_b}{\Gamma_b}\right) \nabla W_b(\mathbf{r}_a)\Delta V_b. \tag{3.26}$$

Following Flekkøy et *al.* ([116], [83]) the inter-particle averaged shear tensor $\mathbf{T}_{ab}^V$ whose compressible part is neglected can be approximated as

$$\begin{aligned} \mathbf{T}_{ab}^V = & \frac{2\mu_a\mu_b}{\mu_a + \mu_b}\frac{1}{r_{ab}^2} \\ & [(\mathbf{r}_a - \mathbf{r}_b) \otimes (\mathbf{u}_a - \mathbf{u}_b) + (\mathbf{u}_a - \mathbf{u}_b) \otimes (\mathbf{r}_a - \mathbf{r}_b)] \end{aligned} \tag{3.27}$$

The viscous force acting on the generic particle a can be evaluated through the discrete formula

$$\nabla \cdot \mathbb{V} = \frac{1}{2}\sum_b^N \left(\frac{1}{\Gamma_a} + \frac{1}{\Gamma_b}\right) \mathbf{T}_{ab}^V \nabla W_b(\mathbf{r}_a)\Delta V_b \tag{3.28}$$

Neglecting the compressibility effects, this formula can be rewritten as (for details see [116])

$$\nabla \cdot \mathbb{V} = \sum_{b}^{N} \frac{2\mu_a \mu_b}{\mu_a + \mu_b} \left(\frac{1}{\Gamma_a} + \frac{1}{\Gamma_b} \right) \frac{(\mathbf{x}_a - \mathbf{x}_b) \cdot \nabla W_b(\mathbf{r}_a)}{\|\mathbf{r}_{ab}\|^2} (\mathbf{u}_a - \mathbf{u}_b) \Delta V_b \tag{3.29}$$

which resembles a mixing of the formulæ adopted by Morris et *al.* [109] and Monaghan [104] with the presence of the corrective term $[1/\Gamma_a + 1/\Gamma_a]$. Anyway, differently from the equation proposed by Monaghan [[104] (3.29), does not preserve the angular momentum. A possible adaptation of the Monaghan formula to the present formulation is

$$\nabla \cdot \mathbb{V} = \sum_{b}^{N} \frac{8\mu_a \mu_b}{\mu_a + \mu_b} \left(\frac{1}{\Gamma_a} + \frac{1}{\Gamma_b} \right) \frac{(\mathbf{x}_a - \mathbf{x}_b) \cdot (\mathbf{u}_a - \mathbf{u}_b)}{\|\mathbf{r}_{ab}\|^2} \nabla W_b(\mathbf{r}_a) \Delta V_b \tag{3.30}$$

The expression (3.30) still preserves linear and angular momenta. Note that without the corrective term $[1/\Gamma_a + 1/\Gamma_a]$ in formulae (3.29 and (3.30), the viscous force unphysically decreases close to the free surface as shown in [117].

To model the surface tension, a continuous surface force (*CSF*) model [118] can be adopted. To simplify the notation we consider only two fluids (*X*,*Y*) here. The surface tension $\mathbb{F}_{Sa}^{XY}$ acting on the generic *a*-th particle belonging to the fluid *X* due to the presence of *Y*, can be evaluated by

$$\begin{cases} \mathbb{F}_{Sa}^{XY} = \nabla \cdot \mathbf{T}_{Sa}^{XY} \qquad \forall a \in X \\ \mathbf{T}_{Sa}^{XY} = \sigma^{XY} \dfrac{1}{|\nabla c|} \left(\dfrac{1}{\lambda} |\nabla c_a|^2 - \nabla c_a \otimes \nabla c_a \right) \end{cases} \tag{3.31}$$

where $\mathbf{T}_{Sa}^{XY}$ is the surface stress tensor and σ^{XY} is the surface tension coefficient between the fluids *X* and *Y*; λ is the spatial dimension of the problem. The tensor $\mathbf{T}_{Sa}^{XY}$ can be evaluated through the spatial gradient of a color index c which has a unit jump across the interface between *X* and *Y*

$$c_a^Y = \begin{cases} 0 & a \in X \\ 1 & a \in Y \end{cases} \tag{3.32}$$

In the present formulation this gradient ∇c_a^{XY} can be evaluated as

$$\nabla c_a^{XY} = \sum_{b \in Y} \left(\frac{c_a^Y}{\Gamma_a} + \frac{c_b^Y}{\Gamma_b} \right) \nabla_a W_b(\mathbf{r}_a) \Delta V_b \,, \quad \forall a \in X \tag{3.33}$$

where $c_a^Y = 0$ by definition since particle a belongs to fluid *X*. Note that this formulation provides surface tension effects between two different fluids but it does not produce any surface tension on a free surface (where ∇c becomes zero). Finally, the divergence of the surface stress tensor $\mathbf{T}^{XY}_{Sa}$ is evaluated through a discrete operator similar to the one used for the pressure gradient (see Equation (3.26))

$$\mathbb{F}^{XY}_{Sa} = \nabla \cdot \mathbf{T}^{XY}_{Sa} = \sum_{b} \left(\frac{\mathbf{T}^{XY}_{Sa}}{\Gamma_a} + \frac{\mathbf{T}^{XY}_{Sb}}{\Gamma_b} \right) \nabla_a W_b(\mathbf{r}_a)\, \Delta V_b \tag{3.34}$$

For interface flows where surface tension effects are negligible a spurious fragmentation of the interface can take place. To prevent this, a small repulsive force is introduced in the pressure gradient having the following momentum equation:

$$\begin{aligned} \frac{D\mathbf{u}_a}{Dt} &= -\frac{1}{\rho_a} \sum_{b} \left(\frac{p_a}{\Gamma_a} + \frac{p_b}{\Gamma_b} \right) \nabla_a W_b(\mathbf{r}_a)\, \Delta V_b + \\ &+ \chi \sum_{b \in X^{\zeta}} \left(\left| \frac{p_a}{\Gamma_a} \right| + \left| \frac{p_b}{\Gamma_b} \right| \right) \nabla_a W_b(\mathbf{r}_a)\, \Delta V_b \end{aligned} \tag{3.35}$$

where χ ranges between 0.01 and 0.1, and the second summation applies to all the particles which do not belong to the fluid of the a-th particle; the latter set of particles is noted by X^{ζ}.

3.4 SUMMARIZING CONTINUITY AND MOMENTUM EQUATIONS USED FOR THE SIMULATIONS

Different systems of continuity and momentum equations are adopted in this thesis in order to perform several simulations. Here there is a summary (see the systems below).

SYSTEM 1

$$\begin{aligned} \frac{D\rho_a}{Dt} &= -\sum_{b}^{N} m_b \left(\mathbf{u}_b - \mathbf{u}_a \right) \cdot \nabla W_b(\mathbf{r}_a) \\ \frac{D\mathbf{u}_a}{Dt} &= -\sum_{b}^{N} m_b \left(\frac{p_a}{\rho_a^2} + \frac{p_b}{\rho_b^2} \right) \nabla W_b(\mathbf{r}_a) + \mathbf{g}_a + m_b \prod_{ab} \nabla_a W_b(\mathbf{r}_a) \end{aligned}$$

This formulation is adopted by many authors (see *e.g.*Monaghan [4]).

SYSTEM 2

$$\begin{aligned} \frac{D\rho_a}{Dt} &= -\rho_a \sum_{b}^{N} \left(\mathbf{u}_b - \mathbf{u}_a \right) \cdot \nabla W_b(\mathbf{r}_a) \Delta V_b \\ \frac{D\mathbf{u}_a}{Dt} &= -\frac{1}{\rho_a} \sum_{b}^{N} \left(p_a + p_b \right) \nabla W_b(\mathbf{r}_a) \Delta V_b + \mathbf{g}_a + \\ &+ \frac{\alpha \epsilon c_0 \rho_0}{\rho_a} \sum_{b} \frac{\left(\mathbf{u}_b - \mathbf{u}_a \right) \cdot \mathbf{r}_{ba}}{\left\| \mathbf{r}_{ab} \right\|^2} \nabla_a W_b(\mathbf{r}_a)\, \Delta V_b \end{aligned}$$

This formulation is adopted in particular by Colagrossi (see *e.g.* [6], [54]).

SYSTEM 3

$$
\begin{aligned}
\frac{D\rho_a}{Dt} &= -\rho_a \sum_b^N (\mathbf{u}_b - \mathbf{u}_a) \cdot \nabla W_b(\mathbf{r}_a)\Delta V_b \\
\frac{D\mathbf{u}_a}{Dt} &= -\frac{1}{\rho_a} \sum_b^N (p_a + p_b)\, \nabla W_b(\mathbf{r}_a)\Delta V_b + \mathbf{g}_a + \\
&\quad + \mu \sum_b \frac{8\,(\mathbf{u}_b - \mathbf{u}_a) \cdot \mathbf{r}_{ba}}{\|\mathbf{r}_{ab}\|^2} \nabla_a W_b(\mathbf{r}_a)\Delta V_b
\end{aligned}
$$

This formulation is the same of the previous one but it is based on real viscosity (see *e.g.* [52]).

SYSTEM 4

$$
\begin{aligned}
\rho_a &= \sum_{b\in X} m_b \frac{W_b(\mathbf{r}_a)}{\sum_{k\in X} W_k(\mathbf{r}_a)\Delta V_k} \\
\frac{D\mathbf{u}_a}{Dt} &= -\frac{1}{\rho_a} \sum_b \left(\frac{p_a}{\Gamma_a} + \frac{p_b}{\Gamma_b} \right) \nabla_a W_b(\mathbf{r}_a)\,\Delta V_b \; + \mathbf{g}_a + \\
&\quad + \chi \sum_{b\in X^\zeta} \left(\left|\frac{p_a}{\Gamma_a}\right| + \left|\frac{p_b}{\Gamma_b}\right| \right) \nabla_a W_b(\mathbf{r}_a)\,\Delta V_b
\end{aligned}
$$

This formulation has been introduced by Grenier et *al.* [5]).

3.5 TIME INTEGRATION FOR FLUID MECHANICS EQUATIONS

The time stepping defines the time integration used to update particle positions. Different time integration schemes have been employed in SPH. Because the SPH algorithm reduces the original continuum partial differential equations to sets of ordinary differential equations, any stable time stepping algorithm for ordinary differential equations can be used [104]. The present numerical simulations have been performed using the modified Verlet time stepping scheme (see *e.g.* [113]).

First step:

$$
\begin{aligned}
\mathbf{r}^{j+1/2} &= \mathbf{r}^j + 0.5\Delta t \mathbf{u}^j \\
\rho^{j+1/2} &= \rho^j + 0.5\Delta t \left(\frac{D\rho}{Dt} \right)^j
\end{aligned}
\tag{3.36}
$$

Second step:

$$\begin{aligned}\mathbf{u}^{j+1} &= \mathbf{u}^{j} + \Delta t \left(\frac{D\mathbf{u}}{Dt}\right)^{j+1/2} \\ \mathbf{r}^{j+1} &= \mathbf{r}^{j+1/2} + 0.5\Delta t \boldsymbol{v}^{j+1} \\ \rho^{j+1} &= \rho^{j+1/2} + 0.5\Delta t \left(\frac{D\rho}{Dt}\right)^{j+1/2}\end{aligned} \tag{3.37}$$

where the indices j, $j + 1/2$ and $j + 1$ denote the values at the start, halfway and at the end of a step, respectively. The rate of change of density, $D\rho/Dt$, and the particle acceleration, $D\mathbf{u}/Dt$, are calculated from continuity (§3.2.1) and momentum equation (§3.2.2), respectively.

The time step Δt is evaluated considering the Courant-Friedrichs-Levy (CFL) condition:

$$\Delta t = C_{FL} \frac{\epsilon}{max_j \left(c_j + \|\mathbf{u}_j\|\right)} \tag{3.38}$$

where $0 < C_{FL} < 1.2$ is the Courant number.

4 DIFFUSION AND ADVECTIVE DIFFUSION EQUATIONS IN SPH CONTEXT

CONTENTS

4.1 Governing equations in Environmental Hydraulics 35
4.2 A novel SPH discrete formalism of Environmental Hydraulic Equations 36
  4.2.1 Diffusion Equation 36
  4.2.2 Advective Diffusion Equation 38
  4.2.3 Reactive Diffusion Equation 38
4.3 Time integration coupling Diffusion equation to Fluid Mechanics Equations 39

In this Chapter, a novel SPH fashion for discretizing the diffusion equation in Environmental Hydraulics context is introduced. The Lagrangian formalism is extended to advective diffusion and reactive diffusion equations.

4.1 GOVERNING EQUATIONS IN ENVIRONMENTAL HYDRAULICS

Pollutant transport in still water is generally dominated by the effect of diffusion and advection processes. For pollutants having densities close to the water and initial velocity equal to zero, the evaluation of the concentration field is induced by diffusion. This phenomenon is characterized by the scattering of particles by random molecular motions. If the contaminant density is quite different from the water, the phenomena of natural advection become relevant. The transport process is consequently associated to the induced kinematics. In rivers a host of processes lead to a non-uniform velocity field, which allows mixing to occur much faster than by molecular diffusion alone (see *e.g.* [119]). In this case the turbulent diffusion processes assume a fundamental role in modeling the concentration field.

Diffusion phenomena of pollutants are described by Fick's law [120]. Fick extended the Fourier heat transfer equation to the analysis of diffusion processes. This law states the proportionality between the mass flux diffusion, DC/Dt, and the concentration gradient, ∇C. In the absence of advective phenomena, this hypothesis coupled with the mass conservation leads to the classical diffusion equation:

$$\frac{DC}{Dt} = \mathcal{D}\nabla^2 C \tag{4.1}$$

where $\mathcal{D}$ is the diffusion coefficient and C is the tracer concentration.

Transport occurs in fluids through the combination of advection and diffusion. When the ratio density between the two fluids (for example $\rho_2/\rho_1 = 0.1$, being ρ_1 the water density and ρ_2 the pollutant one), the evolution of the concentration field of pollutant in still water is influenced by the velocities of the particles. This phenomenon can be modeled by the advective diffusion equation, including the fickian diffusion term and the advective transport (see *e.g.* [121]):

$$\frac{DC}{Dt} = \mathcal{D}\nabla^2 C - \nabla \cdot (\mathbf{u}C) \tag{4.2}$$

4.2 A NOVEL SPH DISCRETE FORMALISM OF ENVIRONMENTAL HYDRAULIC EQUATIONS

In this paragraph, a SPH formalism for diffusion, advective diffusion and reactive diffusion equations is proposed, starting from the approach of Monaghan and Cleary [88] in heat transfer field.

4.2.1 Diffusion Equation

The Lagrangian SPH formalism of the diffusion equation has some drawbacks. First, it is very sensitive to particle disorder. Moreover the transfer of concentration between the particles may be positive or negative, depending on their separation because the second derivative of the kernel can change sign. This behaviour can lead to less accuracy, especially at low resolution [71].

Following the approach used by Cleary and Monaghan [88] for determining a correct SPH formalism of heat conduction equation, Equation (4.1) is here rewritten as follows:

$$\frac{DC}{Dt} = \frac{\mathcal{D}\rho}{\rho}\nabla^2 C = \frac{1}{\rho}\nabla \cdot (\mathcal{D}\rho\nabla C) \tag{4.3}$$

The spatial derivatives can be calculated using an integral approximation [122] [88] in order to define a better SPH form of diffusion equation:

$$\nabla \cdot (\mathcal{D}\rho\nabla C) = \int_S \left[\mathcal{D}(\mathbf{r}')\rho(\mathbf{r}') + \mathcal{D}(\mathbf{r})\rho(\mathbf{r})\right] \\ \left[C(\mathbf{r}) + C(\mathbf{r}')\right] \frac{(\mathbf{r}-\mathbf{r}')\cdot\nabla_r W(\mathbf{r}-\mathbf{r}',\epsilon)}{(\mathbf{r}-\mathbf{r}')^2+\eta^2} d\mathbf{r}' \tag{4.4}$$

Expanding $\mathcal{D}(\mathbf{r}')\rho(\mathbf{r}')$ and $C(\mathbf{r}')$ in Taylor series about $\mathbf{r}$, and keeping up to second order terms, this integral differs from the actual diffusion term $\nabla \cdot (\mathcal{D}\rho\nabla C)$ by $\mathcal{O}(\epsilon^2)$ errors. In this case the SPH formalism of Equation (4.3) takes the form:

$$\frac{DC_a}{Dt} = \sum_b^N \frac{m_b}{\rho_a\rho_b}(\mathcal{D}_a + \mathcal{D}_b)(\rho_a+\rho_b)\frac{\mathbf{r}_{ab}\cdot\nabla_a W_b(\mathbf{r}_a)}{\mathbf{r}_{ab}^2+\eta^2}C_{ab} \tag{4.5}$$

where $C_{ab} = C_a - C_b$.

Because the term

$$\frac{\mathbf{r}_{ab} \cdot \nabla_a W_b(\mathbf{r}_a)}{r^2 + \eta^2} C_{ab}$$

is less or equal to zero, Equation (4.5) has the property that if $C_a > C_b$, then the diffusion process will propagate from a to b, resulting in the molecularly dispersed contaminant tending to move from a volume element with a higher concentration toward any neighboring element with a lower concentration. As observed by Cleary and Monaghan [88] for heat conduction problems, the SPH formalism of Equation (4.5) does not guarantee that the diffusion will be continuous when $\mathcal{D}$ is discontinuous, as for example along the interface between two phases. This drawback can be avoided by replacing the summation $\mathcal{D}_a + \mathcal{D}_b$ with the term:

$$\frac{4\mathcal{D}_a\mathcal{D}_b}{\mathcal{D}_a + \mathcal{D}_b} \tag{4.6}$$

Consequently, the proposed SPH diffusion equation takes the form:

$$\frac{DC_a}{Dt} = \sum_b^N \frac{m_b}{\rho_a\rho_b} \frac{4\mathcal{D}_a\mathcal{D}_b}{\mathcal{D}_a + \mathcal{D}_b} (\rho_a + \rho_b) \frac{\mathbf{r}_{ab} \cdot \nabla_a W_b(\mathbf{r}_a)}{r_{ab}^2 + \eta^2} C_{ab} \tag{4.7}$$

Equation (4.7) represents a suitable SPH diffusion form for determining the concentration field of pollutants in water. This form makes it possible to obtain a continuity of the diffusion phenomena even with large jumps in $\mathcal{D}$, while also avoiding the particle disorder during the evolution of the concentration field. Moreover diffusion problems with discontinuous $\mathcal{D}$ are accurately integrated and the total mass of pollutant and water is conserved by Equation (4.7).

Different SPH diffusion models have been proposed in other fields. In particular these formulations have been referred to different combinations of the terms involving diffusion coefficients and densities. Zhu and Fox [89] [90] suggested the following SPH form of the diffusion equation applied to spatially periodic porous media:

$$\frac{DC_a}{Dt} = \sum_b^N \frac{m_a}{\rho_a\rho_b} (\mathcal{D}_a\rho_a + \mathcal{D}_b\rho_b) \frac{\mathbf{r}_{ab} \cdot \nabla_a W_b(\mathbf{r}_a)}{r_{ab}^2 + \eta^2} C_{ab} \tag{4.8}$$

A similar SPH form of the diffusion equation was developed by Tartakovsky and Meakin [91] and Tartakovsky et *al.* [92] to simulate a two-dimensional Rayleigh-Taylor instability, three-dimensional miscible flows in fractures, and reactive transport and precipitation in fractured and porous materials:

$$\frac{DC_a}{Dt} = \sum_b^N \frac{(m_b\rho_a\mathcal{D}_a + m_a\rho_b\mathcal{D}_b)}{\rho_a\rho_b} \frac{\mathbf{r}_{ab} \cdot \nabla_a W_b(\mathbf{r}_a)}{r_{ab}^2 + \eta^2} C_{ab} \tag{4.9}$$

Finally Monaghan [104] formulated a SPH diffusion equation to evaluate the salt concentration with an analogous form of the SPH heat conduction equation [88], by replacing the thermal conductivity coefficient with the diffusion coefficient, and the absolute temperature with the concentration, as follows:

$$\frac{DC_a}{Dt} = \sum_b^N \frac{m_b}{\rho_a \rho_b} \frac{4\mathcal{D}_a \mathcal{D}_b}{\mathcal{D}_a + \mathcal{D}_b} \frac{\mathbf{r}_{ab} \cdot \nabla_a W_b(\mathbf{r}_a)}{r_{ab}^2 + \eta^2} C_{ab} \tag{4.10}$$

In Chapter 7 the proposed SPH diffusion formulation (Equation 4.7) and the other lagrangian diffusion models (Equation 4.8, 4.9 and 4.10) are compared to evaluate the concentration field induced by a two-phase contaminant-water flow.

4.2.2 Advective Diffusion Equation

The advective diffusion equation (4.2) can be rewritten in the following fashion in order to get better numerical results:

$$\frac{DC}{Dt} = \frac{1}{\rho} \nabla \cdot (\mathcal{D} \rho \nabla C) - \frac{1}{\rho} [\nabla \cdot (\rho \mathbf{u} C) - \mathbf{u} C \cdot \nabla \rho] \tag{4.11}$$

The SPH form of Equation (4.11) becomes:

$$\begin{aligned} \frac{DC_a}{Dt} = \sum_b^N \frac{m_b}{\rho_a \rho_b} \frac{4\mathcal{D}_a \mathcal{D}_b}{\mathcal{D}_a + \mathcal{D}_b} (\rho_a + \rho_b) \frac{\mathbf{r}_{ab} \cdot \nabla_a W_b(\mathbf{r}_a)}{r_{ab}^2 + \eta^2} C_{ab} + \\ - \sum_b^N m_b \frac{C_a}{\rho_a} \mathbf{u}_{ab} \cdot \nabla_a W_b(\mathbf{r}_a) \end{aligned} \tag{4.12}$$

It is worth noting that the contribution of the advective term in Equation (4.12) produces numerical instabilities at the interface for low density ratios ($\rho_2/\rho_1 < 0.1$), such as the case of air-water. In this case the problem can be avoided by replacing m_b/ρ_a with m_b/ρ_b in the SPH advective formalism. This change gives a smoother density gradient at the contact surface of the fluids, preventing anomalous high values of the concentration and leading to a decay in the transport process.

4.2.3 Reactive Diffusion Equation

The kinetics reaction is the study of the rate of formation of products from reactants in a transformation reaction.

Here a reactive diffusion equation is introduced:

$$\begin{aligned} \frac{DC_a}{Dt} = \sum_b^N \frac{m_b}{\rho_a \rho_b} \frac{4\mathcal{D}_a \mathcal{D}_b}{\mathcal{D}_a + \mathcal{D}_b} (\rho_a + \rho_b) \frac{\mathbf{r}_{ab} \cdot \nabla_a W_b(\mathbf{r}_a)}{r_{ab}^2 + \eta^2} C_{ab} + \\ \pm \mathcal{R}(C_a - C_{eq}) \end{aligned} \tag{4.13}$$

where $\mathcal{R}$ is the local reaction rate constant and C_{eq} is the pollutant concentration in equilibrium with the water. This equation can be also used for reaeration phenomena at interface between water and air (see *e.g.* [123], [124]).

The equation (4.13) refers to a first-order kinetics reaction, but can be extended to *n*-order one.

The simplest type of model to evaluate $\mathcal{R}$ is the Lewis-Whitman model [125], which says that the mixing layer is a constant thickness, δ, which leads to $\mathcal{R}$ given by

$$\mathcal{R} = \frac{\mathcal{D}}{\delta} \tag{4.14}$$

Note that for this model $\mathcal{R}$ is linearly proportional to $\mathcal{D}$, as compared to the square-root dependence derived in the stagnant case. Also, the mixing depth δ is a pure function of the hydrodynamic condition. Thus, once one has an expression for δ, the transfer velocity for different substances can be computed using the various respective molecular diffusivities $\mathcal{D}$. The weakness of this model is that is does not provide any physical insight into how to predict δ; hence, δ must be determined empirically. In this work the mixing layer has the length of the compact support of kernel, $\delta = 2\epsilon$.

The Equation (4.13) can be particularized adding the advective term:

$$\begin{aligned}\frac{DC_a}{Dt} = &\sum_b^N \frac{m_b}{\rho_a\rho_b}\frac{4\mathcal{D}_a\mathcal{D}_b}{\mathcal{D}_a+\mathcal{D}_b}(\rho_a+\rho_b)\frac{\mathbf{r}_{ab}\cdot\nabla_a W_b(\mathbf{r}_a)}{\mathbf{r}_{ab}^2+\eta^2}C_{ab}+\\ &-\sum_b^N m_b\frac{C_a}{\rho_a}\mathbf{u}_{ab}\cdot\nabla_a W_b(\mathbf{r}_a) \pm \mathcal{R}(C_a - C_{eq})\end{aligned} \tag{4.15}$$

obtaining a reactive advective diffusion equation in SPH form.

4.3 TIME INTEGRATION COUPLING DIFFUSION EQUATION TO FLUID MECHANICS EQUATIONS

In this section the time integration of diffusion equation coupled to the fluid mechanics equation (see Chapter 3) is defined. The two steps are the following.

First step:

$$\begin{aligned}\mathbf{r}^{j+1/2} &= \mathbf{r}^j + 0.5\Delta t\mathbf{u}^j\\ C^{j+1/2} &= C^j + 0.5\Delta t\left(\frac{DC}{Dt}\right)^j \qquad (4.16)\\ \rho^{j+1/2} &= \rho^j + 0.5\Delta t\left(\frac{D\rho}{Dt}\right)^j\end{aligned}$$

$$(4.17)$$

Second step:

$$\begin{aligned}
\mathbf{u}^{j+1} &= \mathbf{u}^{j} + \Delta t \left(\frac{D\mathbf{u}}{Dt}\right)^{j+1/2} \\
\mathbf{r}^{j+1} &= \mathbf{r}^{j+1/2} + 0.5\Delta t \boldsymbol{v}^{j+1} \\
C^{j+1} &= C^{j+1/2} + 0.5\Delta t \left(\frac{DC}{Dt}\right)^{j+1/2} \\
\rho^{j+1} &= \rho^{j+1/2} + 0.5\Delta t \left(\frac{D\rho}{Dt}\right)^{j+1/2}
\end{aligned} \tag{4.18}$$

where the indices j, $j+1/2$ and $j+1$ denote the values at the start, halfway and at the end of a step, respectively. The rate of change of density, $D\rho/Dt$, and the particle acceleration, $D\mathbf{u}/Dt$, are calculated from continuity (§3.2.1) and momentum equation (§3.2.2), respectively. The rate of change of concentration, DC/Dt, is evaluated for diffusion phenomena from Equations (4.7), (4.8), (4.9) or (4.10), for the cases of advective diffusion using Equation (4.12), for the cases of reactive advective diffusion using (4.13) and for the cases of reactive advective diffusion using (4.15).

The time step Δt is evaluated considering the minimum value between the Courant-Friedrichs-Levy (CFL) condition and a diffusion condition derived from the viscous diffusion [71]:

$$\Delta t = \min\left(C_{FL}\frac{\epsilon}{\max_j\left(c_j + \|\mathbf{u}_j\|\right)}; 0.125\frac{\epsilon^2}{D}\right) \tag{4.19}$$

where $0 < C_{FL} < 1.2$ is the Courant number.

5 BOUNDARY CONDITIONS TREATMENT

CONTENTS

5.1 Free-surface Boundary Conditions 41
5.2 Solid Boundary Conditions 41
  5.2.1 Repulsive Forces 42
  5.2.2 Bounce back 44
  5.2.3 Dummy Particles 45
  5.2.4 Ghost Particles 45
  5.2.5 Coupling of Repulsive Forces and Ghost Particles 46
  5.2.6 Fixed Ghost Particles 47
5.3 In/Out-Flow Boundary Conditions 48
  5.3.1 A novel algorithm for simulating open-channel flows 48

The Chapter describes the main techniques for modeling solid boundaries highlighting capabilities and drawbacks for each one. Furthermore, a novel algorithm for the enforcement of upstream and downstream boundary conditions based on inflow and outflow particles is presented.

5.1 FREE-SURFACE BOUNDARY CONDITIONS

The free-surface boundary conditions can be easily handled by the SPH method. Due to the Lagrangian character of the solver, the kinematic condition is intrinsically satisfied. For the dynamic boundary condition, the enforcement of null-pressure along the free-surface is satisfied implicitly by the discrete SPH equations since these can be derived through a Lagrangian Variational Principle where the work done by the external pressure field on the free surface is forced to be zero even at the discrete level (see for more details [115], [52]). The implicit enforcement of the free-surface dynamic boundary is one of the main advantages of the weakly compressible SPH method in comparison to other field solvers where this boundary condition has to be forced directly.

5.2 SOLID BOUNDARY CONDITIONS

The boundary becomes an issue in SPH when dealing with solid boundaries. The enforcement of solid boundary conditions is a drawback for the SPH while its features are an advantage in the cases of free boundary conditions.

While the free surface does not require any specific treatment with SPH (the particles move freely at the free surface), the solid-boundary treatment is a crucial point and exact free-slip/no-slip boundary conditions are difficult to obtain. This is because there are no specific fluid particles that stay close to the boundaries. The physical values of the magnitudes to be forced on them should come from interpolation with the neighbor particles but this approach is unpractical.

Here some method to enforce solid boundary conditions are illustrated.

5.2.1 Repulsive Forces

Microscopically, solid structures are constituted by atoms which exert forces on fluid. Inspired by this physical principle, wall can be modeled in SPH theory by solid particles which exert repulsive forces on fluid particles ([69], [4]), ensuring thus wall impermeability. These solid particles are not involved in the pressure gradient term of the momentum equation. However, if zero velocity at the wall is required, they contribute to the viscous term in order to mimic no-slip conditions. The solid particles are immobile or can define a mobile wall. In this last case, their velocity is equal to the wall velocity: for instance, Monaghan [126] considered a moving lock gate modeled by a set of moving wall particles.

Three types of forces among several are presented in this part: purely repulsive forces, similar Lennard-Jones forces and normal forces. These forces are added in right hand side of the momentum equation as external forces

Purely repulsive forces

One of the most employed method to set boundary conditions in hydrodynamic simulations was introduced by Monaghan [4]. The method was conceived as an inter-molecular repulsive force. Considering a boundary and a fluid particle at the given distance r, the force between them is defined as:

$$F_1(r) = A_1 \left[\left(\frac{r_0}{r}\right)^{P_1} - \left(\frac{r_0}{r}\right)^{P_2} \right] \frac{\mathbf{r}}{r^2} \tag{5.1}$$

The considered force $F_1(r)$ is set to zero for $r > r_0$, and so is central purely repulsive. In the same paper, Monaghan [4] suggest to use the values $P_1 = 12$ and $P_2 = 6$ for the constants in (5.1) (the most important features is $P_1 > p_2$). Moreover, while r_0 is the scaling initial particle distance in the repulsive force, A_1 is a coefficient to be set for each different problem. For a flow driven by the gravity, if H defines a characteristic vertical length scale of the problem, a value of A_1 around gH is suitable [4].

Lennard-Jones forces

Another central solid force, inspired by Lennard-Jones interatomic force, is presented. Contrary to the previous one, this force has an attractive core:

$$F_2(r) = \begin{cases} A_2 \left[\left(\frac{1}{r}\right)^m - \left(\frac{1}{r}\right)^n \right] & \text{if } 0 < r < r_c \\ A_3 (R - r)^2 + A_4 (R - r) & \text{if } r_c < r < R \\ 0 & \text{if } r > R \end{cases} \tag{5.2}$$

where r_c represents the distance which separates the attractive part from the repulsive one of the force. Values of different parameters of Equation (5.2) are defined by Monaghan [126]. One problem associated to central forces is that they produce unphysical perturbations in the flow.

Normal repulsive forces

Monaghan faced the problem of the irregular force distribution over a smooth plane given by the repulsive force expressed by Equation (5.1). The new form of the repulsive force is defined by Monaghan and Kos [57] as:

$$F_3 \left(r_{//}, r_\perp \right) = \mathbf{n} \cdot R \left(r_\perp \right) \cdot P \left(r_{//} \right) \tag{5.3}$$

where F_3 is the force per unit mass on a fluid particle, and it is evaluated considering two different contributions. Considering the upper sketch in Figure 5, the former is defined as a function of the normal distance $r_\perp$ of the fluid particle from the boundary at hand; the latter is defined as a function of the distance $r_{//}$ between the fluid and the boundary particles, taken along the tangent. $R \left(r_\perp \right)$ is defined as:

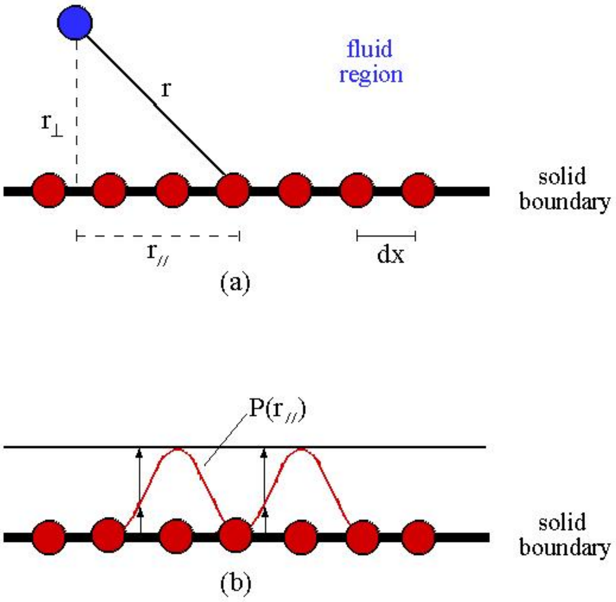

Figure 5: Repulsive forces boundary conditions. On the top, distances between a fluid particle (blue particle) and a boundary particle (red particles). On the bottom, repulsive contributions of two boundary particles.

$$R\left(r_{\perp}\right)=\begin{cases} A_5\frac{1}{\sqrt{q}}\left(1-q\right) & \text{for } r_{\perp}<dx \\ 0 & \text{for } r_{\perp}\geqslant dx \end{cases} \tag{5.4}$$

where $q=\frac{r_{\perp}}{dx}$, $A_5=\frac{1}{\epsilon}\left(\beta_1 c_0^2+\beta_2 c_0\,\mathbf{u}_{ab}\cdot\mathbf{n}_a\right)$. On the other hand, $P\left(r_{//}\right)$ is a function set to balance the repulsive contributions from neighbor boundary particles, in order to ensure that the repulsive force presents a constant value at each point of the boundary line. The role of the P function is explained by the lower sketch of Figure 5, and it is defined as:

$$P\left(r_{//}\right)=\begin{cases} \frac{1}{2}\left[1+\cos\left(\frac{\pi r_{//}}{dx}\right)\right] & \text{for } r_{\perp}<dx \\ 0 & \text{for } r_{\perp}\geqslant dx \end{cases} \tag{5.5}$$

This kind of boundary conditions are easy to implement, fast in the SPH computational time, and allow to model arbitrary shaped boundaries. However, due to the constant value of the repulsive force along a boundary line, particles in proximity of a boundary are induced to arrange along a layer parallel to the boundary at hand.

One of the limit of this approach is represented by the calibration of parameters which can cause particles disorder at the wall and unphysical effects.

5.2.2 Bounce back

The bounce back boundary implementation is conceptually the simplest method used to enforce boundary conditions within the SPH framework. Particles that are identified as having come into contact with a solid boundary are simply reflected back into the computational domain according to Newton's law of restitution (see Figure 6).

If the interaction between the boundary and the particle is assumed to be perfectly elastic (corresponding to a coefficient of restitution equal to one) then the linear momentum of the system will be conserved.

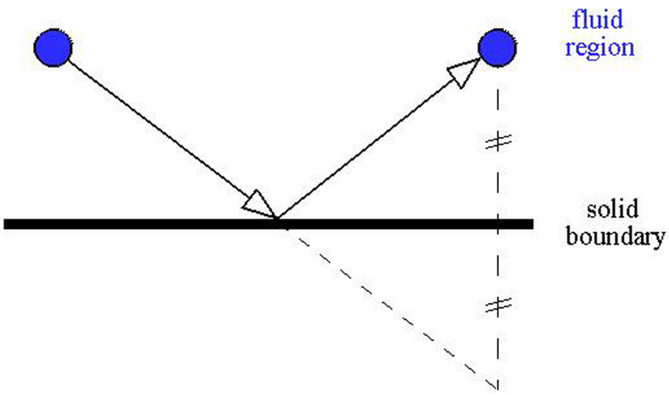

Figure 6: Bounce back method.

The bounce back and repulsive force methods have the limit to induce a missing kernel support area near the solid wall defining an inaccurate gradient operator which provides non-consistent behaviour. It is necessary a near-boundary kernel-corrected version [100] [101] to simulate long-time simulations ideally suited for channel flow with accurate boundary conditions.

5.2.3 Dummy Particles

Dummy particles are regularly distributed at the initial state and have zero velocity through the whole simulation, while several layers of dummy particles [62] are built as an extension of the particles surrounding the solid boundaries to ensure the same order of discretization (in terms of kernel compact support) for particles located close to those boundaries, as for particles located in the core of the domain. This also makes the coding simpler (e.g. for parallelisation) as the same scheme is used for all particles with the only difference that wall particles fix their initial position every time step. The number of dummy particle layers is decided from the radius of the compact support (such that the kernel is not truncated for the near-wall particles).

This approach has the drawback of use zero velocity particles and consequently problems to enforce free-slip conditions.

5.2.4 Ghost Particles

Boundary conditions defined using ghost particles (successively used by Colagrossi and Landrini [6]) reproduce part of the computational fluid domain, which is close to the boundary at hand, symmetrically in a thin layer with dimensions of the order $\mathcal{O}(\epsilon)$, as sketched in Figure 7. Ghost particles present density, pressure and velocity deduced from the fluid particles. The mirroring rules are the followings:

$$\begin{aligned} \mathbf{r}_a^G &= 2\mathbf{r}^B - \mathbf{r}_a \\ u_{\perp,a}^G &= 2U^B - u_{\perp,a} \\ u_{//,a}^G &= u_{//,a} \\ p_a^G &= p_a - \rho_a g z \end{aligned} \tag{5.6}$$

where the sub-index a is referred to a generic fluid particle, the super-index G is referred to the corresponding ghost particle, $\perp$ and $//$ are the normal and the tangential velocity components to the boundary, which is placed at the position $\mathbf{r}^B$. Figure 7 presents a simple reference sketch with a boundary wall parallel to the y axis. For arbitrary shaped boundaries, the particles mirroring has to be performed considering local normal and tangent, making particular attention to particles mass balance between outside and inside the computational domain. As discussed in Colagrossi and Landrini [6], Equations (5.6) permit to model free-slip boundary conditions for plane boundaries allowing the enforcement of the Neumann boundary condition, that is, $\partial p/\partial n = \rho \mathbf{g} \cdot \mathbf{n}$ where $\mathbf{n}$ is the normal unit vector to the solid profile. Boundaries with curvatures need an extension of the ghost particles technique [127] considering the local tangent plane.

Instead, the tangential velocity component is

$$u^G_{//,a} = -u_{//,a} \tag{5.7}$$

for no-slip boundary conditions.

Enforcing $u^G_{//,a} = 0$ for linear and quadratic velocity, a singularity with the inverse of the smoothing length in the viscous term arises [128].

We can summarize that the free-slip and no-slip (5.7) conditions give good results as further discussed by Takeda et *al.* (1994) [70] and Morris et *al.* (1999) [129].

5.2.5 Coupling of Repulsive Forces and Ghost Particles

Some authors (see *e.g.* [130], [131]) adopted the coupling of the normal repulsive forces with the ghost particles. In particular the tangential velocity component of the ghost particles is evaluated through the relationship:

$$u^G_{//,a} = \psi\, u_{//,a} \tag{5.8}$$

where ψ $[0 \div 1]$ is a parameter to calibrate the bottom roughness. This represents the main drawback of this technique and it can generate unphysical effects.

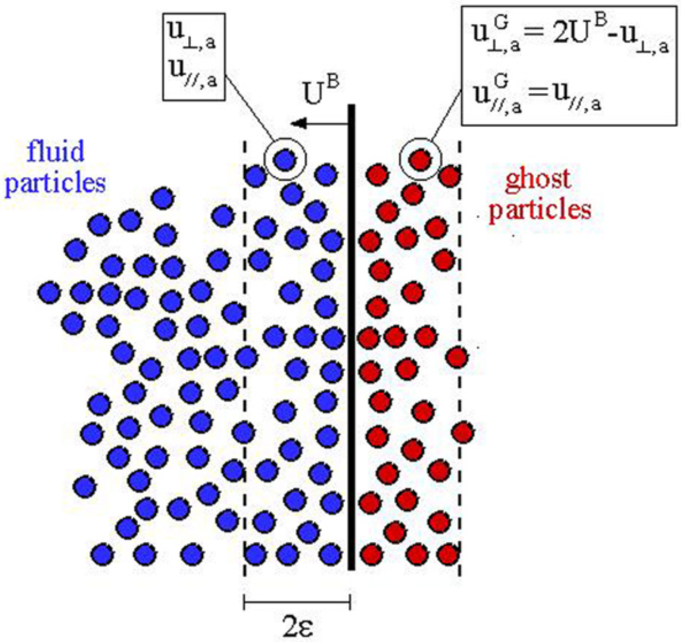

Figure 7: Example of use of ghost particles to enforce no-penetration boundary condition.

5.2.6 Fixed Ghost Particles

In the present section, the enhanced treatment of the solid boundaries within two-dimensional SPH schemes proposed by Marrone et *al.* [97] is illustrated.

The solid boundary is modeled through fixed ghost particles firstly proposed for a simple flat profile by Fang et *al.* [98] and extended by Marrone et *al.* [97] for a generic solid profile. Differently from the classical ghost particles that are instantaneous mirrors of the fluid particles with respect to the body surface [6], the fixed ghost particles are associated to interpolation points internal to the fluid through which they take the flow properties. In this way, it is possible to enforce both Dirichlet and Neumann conditions. In this approach the channel bottom is approximated by points and normal and tangent unit vectors along the body are also assigned. The normal vectors are assumed to be oriented out of the fluid domain and the body points are equispaced with a prescribed interparticle distance dx. Then, using the normal vector, the body points are reproduced out of the fluid at a distance $dx/2$ from the solid profile. These points are the fixed ghost particles. In the same way but using a vector opposite to the normal, each fixed ghost particle is mirrored inside the fluid. These are the associated interpolation points of the fixed ghost particles (see Figure 8). The procedure is repeated to cover the interaction radius of the fluid particles. The main advantage of using the fixed ghost particles instead of the classical ghost technique is that their distribution is always uniform and does not depend on the fluid particle positions. Furthermore, the use of a Moving Least Square interpolation technique [99] ensures an accurate mirroring procedure of the flow quantities. Both free-slip and no-slip conditions can be implemented along solid boundaries. In the former case, the tangential component of velocity is maintained unaltered during the mirroring procedure while, in the latter case, its direction is reversed. In both the cases, the normal component of the fluid velocity is reversed to avoid particles going across the solid profile. For what concerns the assignment of the pressure field along the solid boundaries, the Neumann boundary condition is enforced, that is, $\partial p/\partial n = \rho \mathbf{g} \cdot \mathbf{n}$ where $\mathbf{n}$ is the normal unit vector to the solid profile.

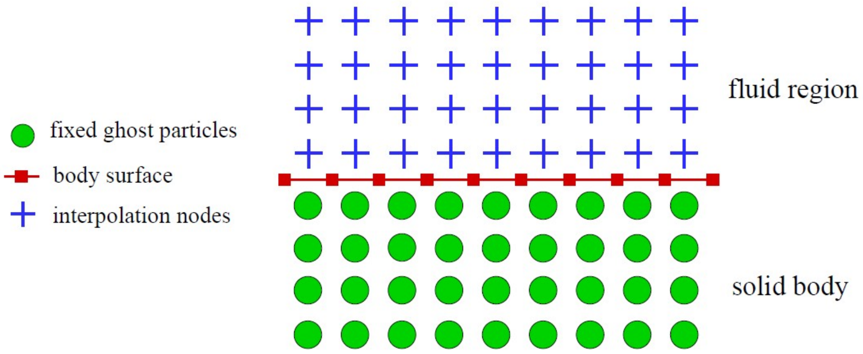

Figure 8: Sketch of fixed ghost particles for the channel bottom.

5.3 IN/OUT-FLOW BOUNDARY CONDITIONS

The enforcement of in/out-flow boundary conditions in SPH context is not trivial for particle methods. These kinds of conditions allow modeling cases as open-channel flow where the imposition of upstream and downstream velocity/pressure fields is necessary. Here, an algorithm for simulating it is introduced.

5.3.1 A novel algorithm for simulating open-channel flows

In the present section the proposed algorithm for the enforcement of in/out-flow boundary conditions is illustrated. In order to assign different upstream and downstream flow conditions two new sets of boundary particles are defined. Four sets of particles are used: fluid (f), fixed ghost (s), inflow (i) and outflow (o) particles. Similarly to the fixed ghost particles, the in/out-flow particles affect the fluid particles but not vice versa. The region covered by these particles is at least as wide as the kernel radius.

Figure 9 shows the initial sketch of the computational domain: different colours are associated to different sets of particles. The flow extends along the x-axis and is limited by an *inlet* and an *outlet* boundary. An *inflow* and an *outflow* threshold are defined, the particles that cross these thresholds change the set they belongs to.

The use of in/out-flow particles permits the imposition of different velocity and pressure fields both upstream and downstream in the computational domain. As regards the water levels the upstream condition is assigned while the downstream one is determined by the flow evolution.

The particles belonging to each set have been listed subsequently in only one array. In this way all the particles interactions can be computed in just one loop over the array elements. Figure 10a displays a generic configura-

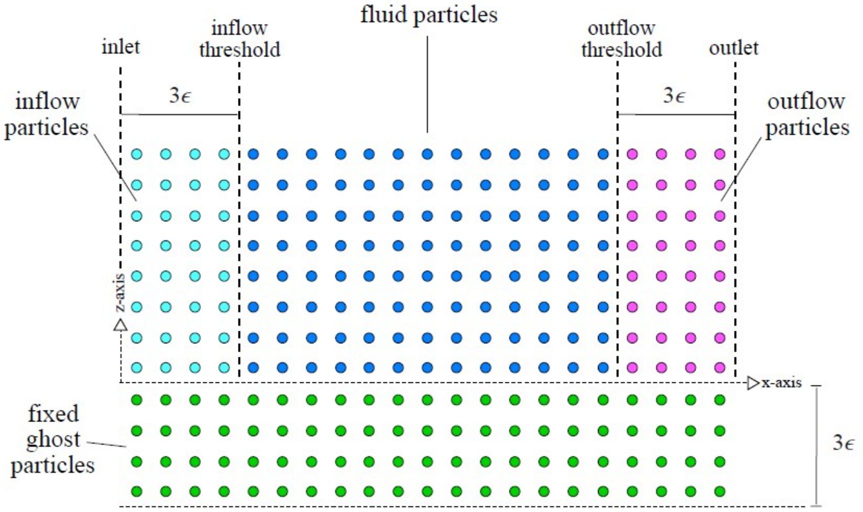

Figure 9: Initial sketch of the computational domain: different colours are associated to different sets of particles.

tion of the whole particles array where N_i, N_f, N_o and N_s are, respectively, the number of inflow, fluid, outflow and fixed ghost particles. Figure 10b shows how the algorithm works. Note that the algorithm is based on the assumption that the fluid particles cannot enter the inflow region.

At each time step a loop over the whole particles array is performed in order to find out the particles that exit from their belonging region. In Figure 10b the symbols $N_{i,inflow}$, $N_{f,outflow}$ and $N_{o,outlet}$ are, respectively, the number of inflow particles that have crossed the inflow threshold, the number of fluid particles that have crossed the outflow threshold and the number of outflow particles that have crossed the outlet. For the sake of simplicity these particles are represented in unique blocks even if in memory they are actually spread over the array (these blocks are named i_2, f_2 and o_2 in Figure 10b). After the determination of the blocks (top panel in Figure 10b), these change the set they belong to. In particular:

- The block i_2 is moved to the fluid particles set and a new inflow particles block of the same size (i_0 in bottom panel in Figure 10b) is created at the beginning of the array. The particles of this new block have the x-coordinate equal to the inlet one and their velocity and pressure are consistent with the enforced upstream boundary conditions.
- The block f_2 is moved from the fluid particles set to the outflow particles set.
- The block o_2 is deleted.

Since some particles are created and others are removed, the algorithm procedure is performed at the end of each time step. This procedure allows several hydraulic problems to be treated due to the possibility to enforcing a wide range of different boundary conditions. The CPU time cost of the present algorithm is approximately 1/10 respect to the computation of a whole time iteration.

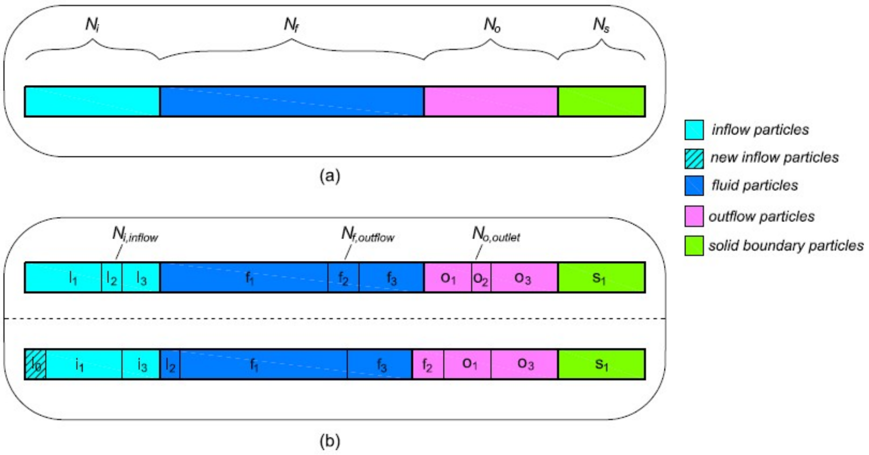

Figure 10: Configuration of the whole particles array (a). Array sketch showing how the in/out-flow algorithm works at each step (b).

Part II

Physical Investigations

6 SIMULATIONS OF DAM BREAKS ON SILLS

CONTENTS

6.1 Test case: dam-breaks on trapezoidal sills 53
  6.1.1 Test case 1 53
  6.1.2 Test case 2 54
  6.1.3 Test case 3 55

In this Chapter the boundary conditions of coupling repulsive forces and ghost particles discussed in §5.2.5 are tested for three dam-breaks on sill generated by an instantaneous gate opening (less than 0.05s). The SPH results are compared with experimental data [132]. In the experiment smooth conditions were considered with a Manning's roughness coefficient $n = 0.01$.

6.1 TEST CASE: DAM-BREAKS ON TRAPEZOIDAL SILLS

In SPH computations (see the three test cases above) the parameter ψ in the Equation (5.8) is imposed 0.4 and the parameter A_5 in (5.4) is:

$$A_5 = \frac{1}{\epsilon}\left(0.01c_0^2 + c_0\,\mathbf{u}_{ab}\cdot\mathbf{n}_a\right) \tag{6.1}$$

Using these parameters the simulations are performed for a long time of $t = 15$s, without any unphysical effect near the boundaries.

The simulations are performed adopting the flow equations of system 1 in §3.4 and imposing the following parameters: $\alpha = 0.03$, $\epsilon_X = 0.3$ and $c_0 = 10\sqrt{gH}$, where H is the initial depth of the water tank.

6.1.1 Test case 1

The first test is characterized by the presence trapezoidal sill located downstream the channel. The horizontal channel configuration is reported in Figure 11 and the geometrical lengths in Table 1.

For different times the particle configuration is reported in Figure 12. The time evolution of the water depth compared with experimental results for the gauges x_{g1}, x_{g2} and x_{g3} is shown in Figure 13.

For the gauge x_{g1}, it is note to worth a good agreement until to $t = 10$ s between numerical and experimental results. After that, the water depth increase calculated by SPH has a time shifting with respect to the

$h_1 = 0.35\,\mathrm{m}$	$x_1 = 2.25\,\mathrm{m}$
$x_2 = 3.85\,\mathrm{m}$	$x_3 = 0.40\,\mathrm{m}$
$x_4 = 0.10\,\mathrm{m}$	$x_5 = 0.40\,\mathrm{m}$
$z_2 = 0.21\,\mathrm{m}$	$x_{g1} = 1.40\,\mathrm{m}$
$x_{g2} = 2.25\,\mathrm{m}$	$x_{g3} = 3.40\,\mathrm{m}$

Table 1: Test case 1: characteristic lengths of the experimental set-up.

experimental values. As regard as the peak values of the water level, a good agreement between numerical and experimental data is shown.

For the gauge x_{g2}, in the first time stage, the decay of depth reaches a lower value for the experimental results compared to the numerical ones. After $t = 11\,\mathrm{s}$, the water depth increase evaluated through SPH has a time shifting with respect to the experimental values. The peak value of the water level at $t = 7\,\mathrm{s}$ calculated by SPH underestimates the experimental one.

For the gauge x_{g3}, it is evident a good agreement between numerical and experimental results. The two water depth increases (at $t = 5\,\mathrm{s}$ and $t = 14\,\mathrm{s}$ approximately) calculated by SPH have a time shifting with respect to the experimental values.

6.1.2 Test case 2

The second test is characterized by the presence of two trapezoidal sills, one located downstream water block and the other downstream the channel. The horizontal channel configuration is reported in Figure 14 and the geometrical lengths in Table 2.

For different times the particle configuration is reported in Figure 15. The time evolution of the water depth compared with experimental results for the gauges x_{g1}, x_{g2} and x_{g3} is shown in Figure 16.

For the gauge x_{g1}, it is note to worth a good agreement until between numerical and experimental results. The two water depth increases (at $t = 8.5\,\mathrm{s}$ and $t = 11\,\mathrm{s}$ approximately) measured by experiments are not highlighted in SPH simulations.

For the gauge x_{g2}, in the first time stage, the decay of depth reaches a lower value for the experimental results compared to the numerical ones.

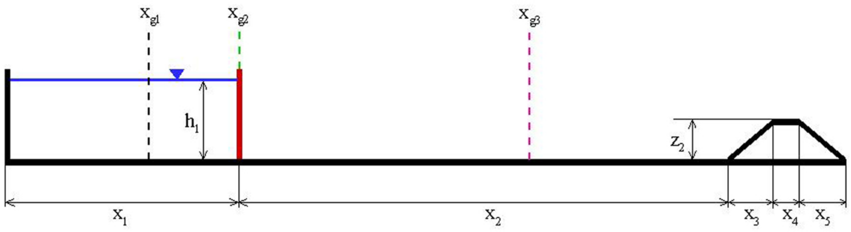

Figure 11: Test case 1: sketch of the experimental set-up.

After that, it is evident a good agreement between numerical and experimental data.

For the gauge x_{g3}, the peak value of the water level at $t = 5\,s$ calculated by SPH slightly overestimates the experimental one. After $t = 9\,s$, the water depth increase calculated by SPH has a time shifting with respect to the experimental value.

6.1.3 Test case 3

The last test is characterized by the presence of a trapezoidal sill located downstream the channel. The channel has a slope s_0 and its configuration is reported in Figure 17 and the geometrical lengths in Table 3.

For different times the particle configuration is reported in Figure 18. The time evolution of the water depth compared with experimental results for the gauges x_{g1}, x_{g2} and x_{g3} is shown in Figure 19.

For the gauge x_{g1}, it is note to worth a good agreement until between numerical and experimental results.

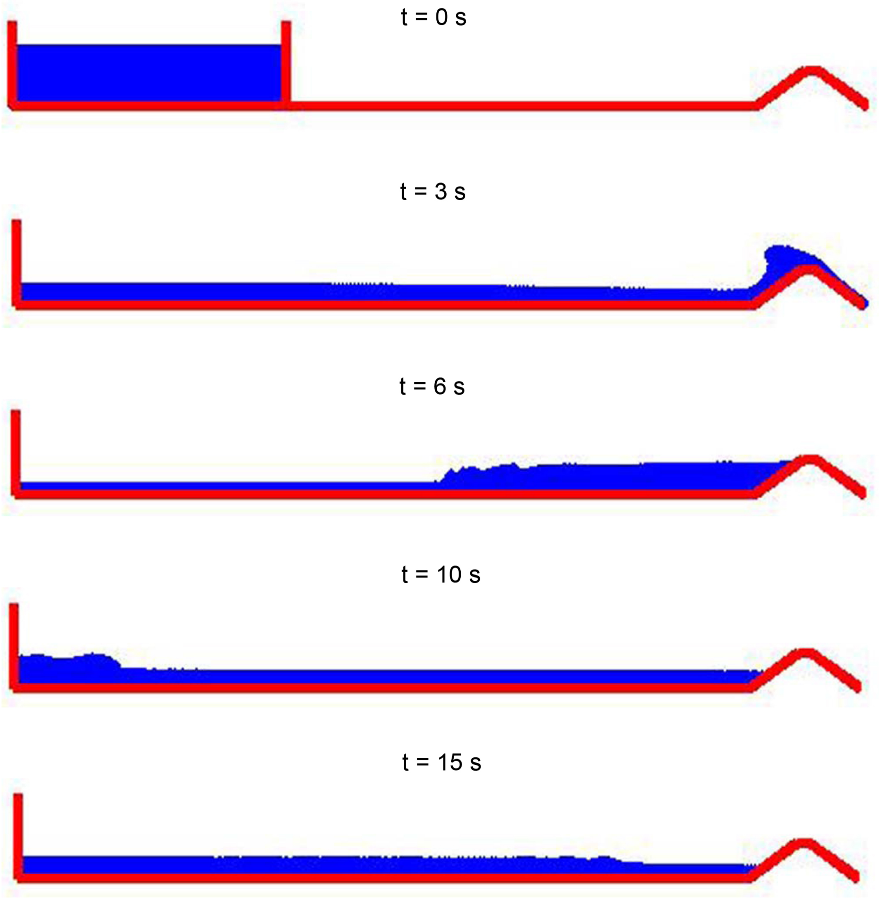

Figure 12: Test case 1: SPH configurations for $t = 0\,s$, $3\,s$, $6\,s$, $10\,s$ and $15\,s$.

For the gauge x_{g2}, in the first time stage, the decay of depth reaches a lower value for the experimental results compared to the numerical ones.

For the gauge x_{g3}, it is evident a good agreement between numerical and experimental results. The water depth increase at $t = 8.5\,\mathrm{s}$ calculated by SPH has a time shifting with respect to the experimental values.

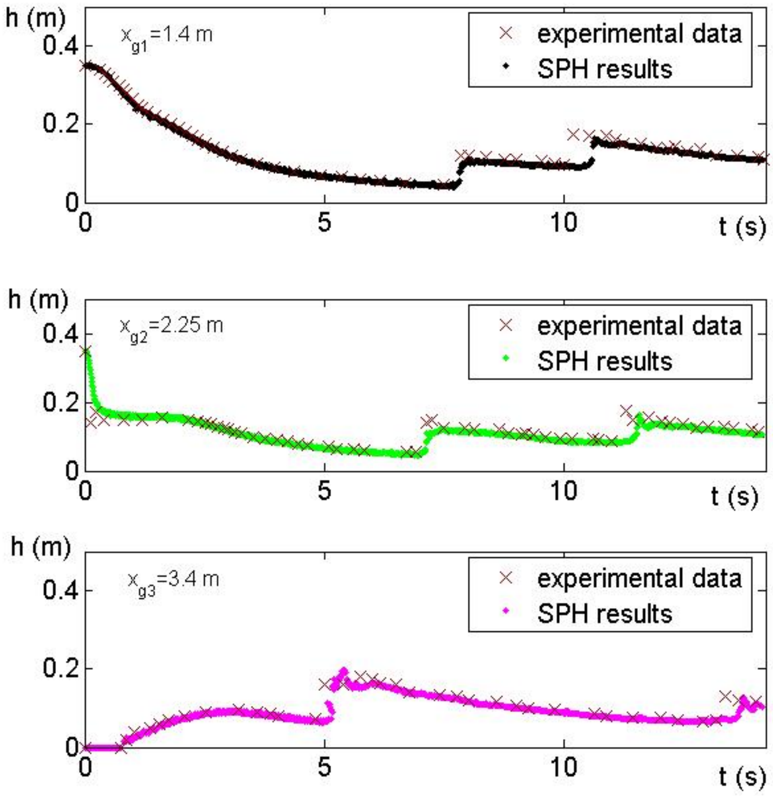

Figure 13: Test case 1: comparisons between numerical results and experimental data at three different gauges.

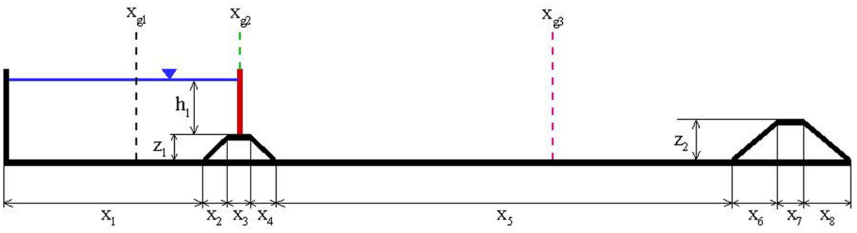

Figure 14: Test case 2: sketch of the experimental set-up.

$h_1 = 0.34\,\mathrm{m}$	$x_1 = 2.00\,\mathrm{m}$
$x_2 = 0.20\,\mathrm{m}$	$x_3 = 0.10\,\mathrm{m}$
$x_4 = 0.20\,\mathrm{m}$	$x_5 = 3.60\,\mathrm{m}$
$x_6 = 0.40\,\mathrm{m}$	$x_7 = 0.10\,\mathrm{m}$
$x_8 = 0.40\,\mathrm{m}$	$z_1 = 0.11\,\mathrm{m}$
$z_2 = 0.21\,\mathrm{m}$	$x_{g1} = 1.40\,\mathrm{m}$
$x_{g2} = 2.25\,\mathrm{m}$	$x_{g3} = 4.50\,\mathrm{m}$

Table 2: Test case 2: characteristic lengths of the experimental set-up.

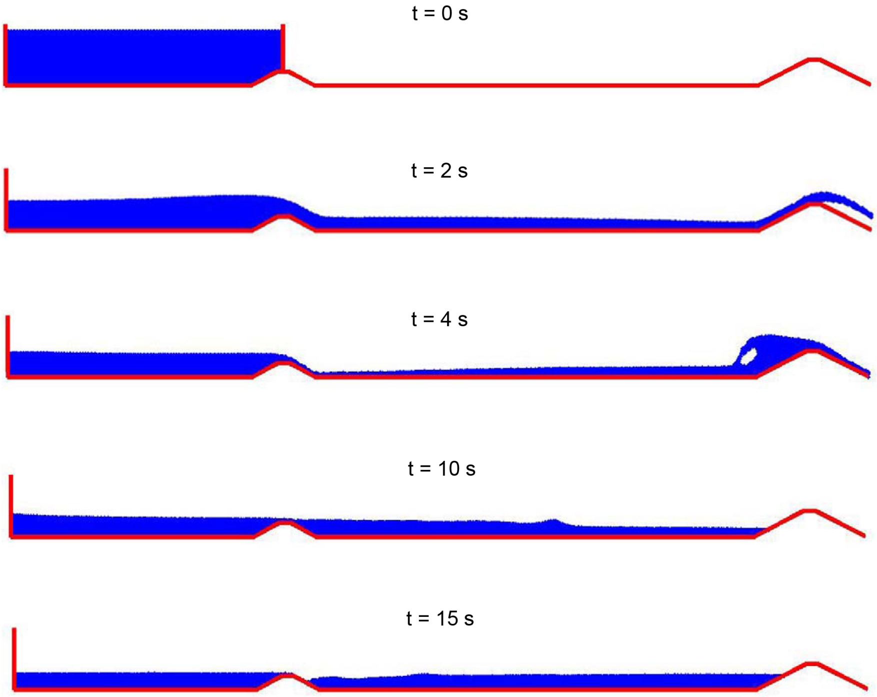

Figure 15: Test case 2: SPH configurations for $t = 0\,\mathrm{s}$, $2\,\mathrm{s}$, $4\,\mathrm{s}$, $10\,\mathrm{s}$ and $15\,\mathrm{s}$.

$h_1 = 0.35\,\mathrm{m}$	$x_1 = 2.25\,\mathrm{m}$
$x_2 = 3.85\,\mathrm{m}$	$x_3 = 0.40\,\mathrm{m}$
$x_4 = 0.10\,\mathrm{m}$	$x_5 = 0.40\,\mathrm{m}$
$z_2 = 0.21\,\mathrm{m}$	$x_{g1} = 1.40\,\mathrm{m}$
$x_{g2} = 2.35\,\mathrm{m}$	$x_{g3} = 3.40\,\mathrm{m}$
$s_0 = 3.3\ \%$	

Table 3: Test case 3: characteristic lengths of the experimental set-up.

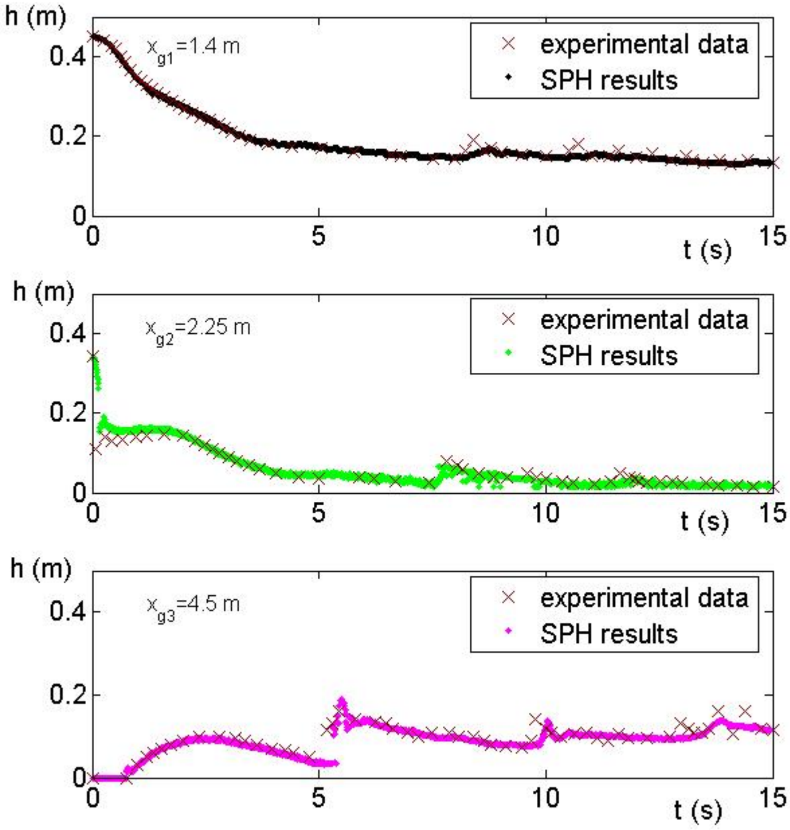

Figure 16: Test case 2: comparisons between numerical results and experimental data at three different gauges.

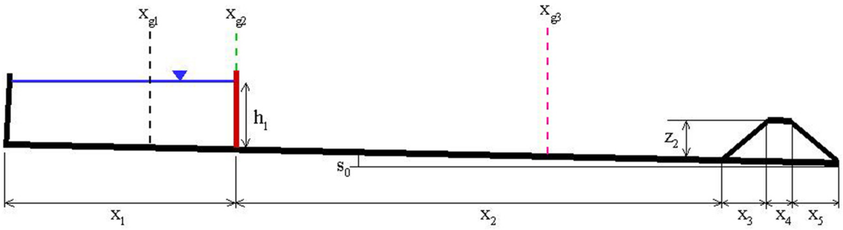
x_{g1}
x_{g2}
x_{g3}
h_1
z_2
s_0
x_1
x_2
x_3
x_4
x_5

Figure 17: Test case 3: sketch of the experimental set-up.

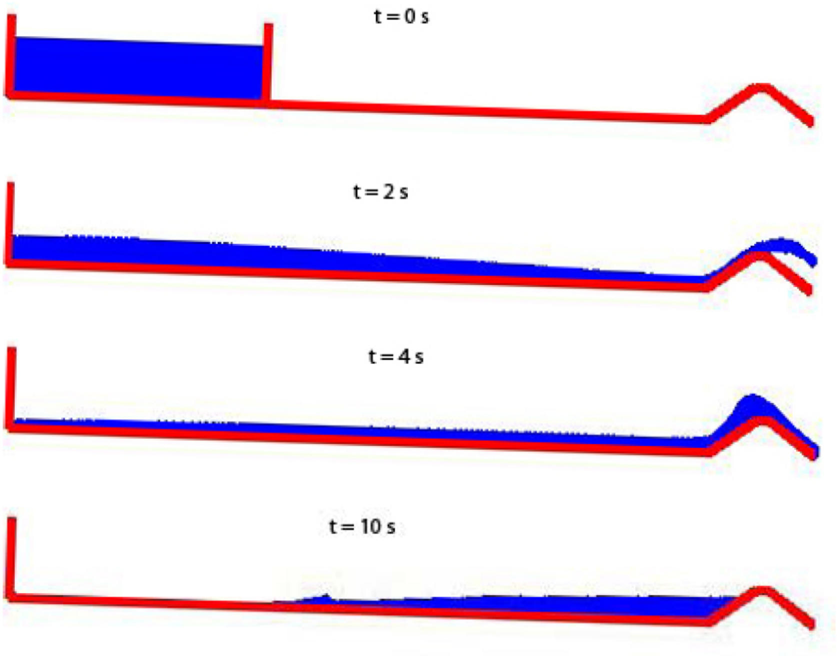
t = 0 s
t = 2 s
t = 4 s
t = 10 s

Figure 18: Test case 3: SPH configurations for $t = 0\,s, 2\,s, 4\,s, 10\,s$ and $15\,s$.

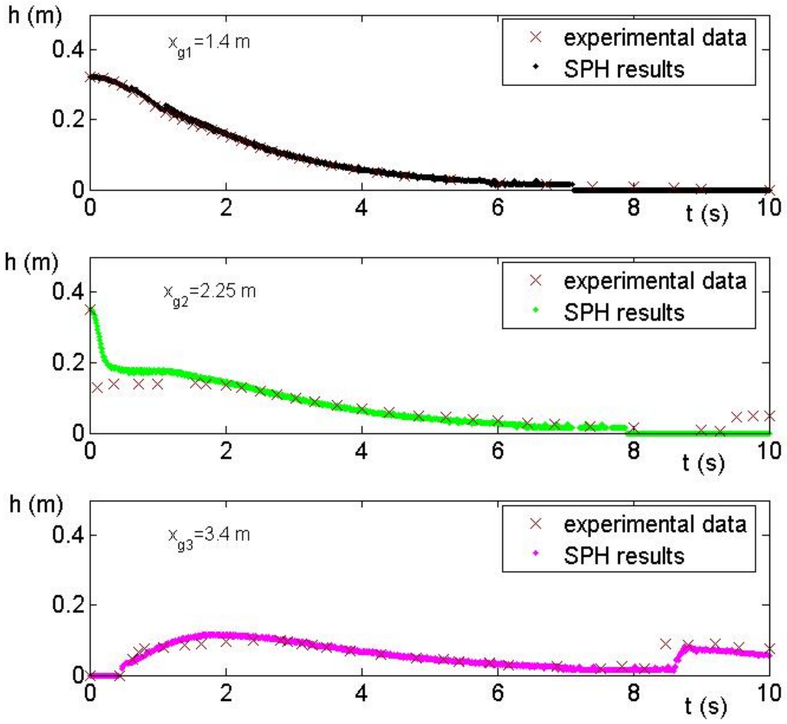

Figure 19: Test case 3: comparisons between numerical results and experimental data at three different gauges.

7 SIMULATIONS OF OPEN-CHANNEL FLOWS

CONTENTS

7.1 Viscous free-surface channel flows in laminar regime 61
7.2 Hydraulic jump 64
  7.2.1 Hydraulic jump with initial condition no. 1 65
  7.2.2 Hydraulic jump with initial condition no. 2 68
7.3 Concluding remarks 71

In this chapter the novel algorithm for the enforcement of upstream / downstream boundary conditions presented in §5.3 is tested to two cases. Firstly, the model is applied to viscous free-surface channel flows at low Reynolds numbers. The suitability of the in/out-flow algorithm is shown comparing the obtained velocity field against the analytical Poiseuille solution in uniform flow (see *e.g.* [134]). Then the capabilities of the algorithm are tested in non uniform flow through different upstream and downstream conditions. A typical phenomenon is the hydraulic jump, that is characterized by sharp discontinuities at the water level and strong dissipative effects. Varying the Froude number, different types of jumps are obtained: undular, breaking undular and weak jump. The results are validated with the classical hydraulic jump theory (see *e.g.* [7]) based on the balance of the upstream and downstream pressure forces. The numerical water depths are compared with the theoretical ones. Numerical simulations are performed for a time interval long enough to reach steady state conditions in order to check the stability and the convergence of the model.

7.1 VISCOUS FREE-SURFACE CHANNEL FLOWS IN LAMINAR REGIME

In this section all the simulations are performed using the equations of system 3 in §3.4.

Uniform, steady and laminar flow in a free-surface channel is a special case of the *Poiseuille* flow (see *e.g.* [134]). The distribution of velocity $u(z)$ for two-dimensional channel flow is given by a second order equation:

$$u(z) = \frac{\rho g s_0}{2\mu}\left(2hz - z^2\right) \tag{7.1}$$

where g is the gravity acceleration, h is the free surface depth, s_0 is the bottom slope and z is the vertical abscissa whose origin is located at the channel bottom.

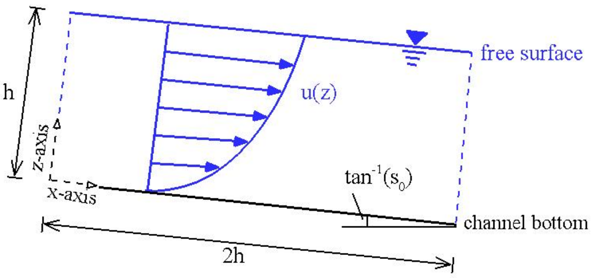

Figure 20: Sketch of the elementary fluid domain

The Reynolds number $Re = \rho Uh/\mu$ is evaluated with reference to the average horizontal velocity $U = \frac{1}{h}\int_0^h u(z)\,dz$.

An elementary fluid domain h deep and $2h$ long with $s_0 = 0.001$ is used to perform simulations at different Re (see Figure 20). The fluid particles are initialized with the analytical solution (7.1) and the value of c_0 is set equal to $10u(z = h)$. At each time step a consistent velocity profile (7.1) is imposed on the in/out-flow particles. The initial and boundary conditions are reported as follows:

$$u_f(z, t = 0) = u_i(z, t) = u_o(z, t) = \frac{\rho g s_0}{2\mu}\left(2hz - z^2\right) \tag{7.2}$$

At the channel bottom no-slip conditions are imposed through the fixed ghost particles where the velocity vectors of the fluid particles are reversed for both normal and tangential components.

The simulations are carried out for a long enough time to let the fluid particles of the initial configuration ($t = 0$) cross the whole fluid domain at least once. The initial spatial resolutions of the simulations are $dx_1 = h/125$, $dx_2 = 2dx$ and $dx_3 = 4dx$.

In Figure 21 the particles distributions at $t(g/h)^{1/2} = 50$ and100 for $Re = 10$ are reported. The initial interparticle distance is dx_3. The flow occurs in almost parallel layers with a quite ordered particles distribution, as expected for a viscous laminar regime.

The in/out-flow boundary conditions allow simulations to be carried out in laminar regime up to Re of order $\mathcal{O}(10^2)$. It is shown in Figure 22 where at $t(g/h)^{1/2} = 100$ the streamline flow and the parabolic velocity field are preserved for $Re = 100$ (Figure 22a) and $Re = 200$ (Figure 22b).

The comparison between the analytical solution (7.1) and the numerical results is reported in Figure 23 at the middle of the domain ($x = h$) at $t(g/h)^{1/2} = 100$ for Re equal to 10, 100 and 200. A good agreement between the analytical and numerical velocity profile for dx_1 can be observed.

In order to check the convergence of the numerical scheme of the proposed in/out-flow algorithm heuristically, a mean square error

$$MSEP = \frac{100}{N}\sum_{j=1}^{N}\left(\frac{u_j^a - u_j^n}{u_j^a}\right)^2 \tag{7.3}$$

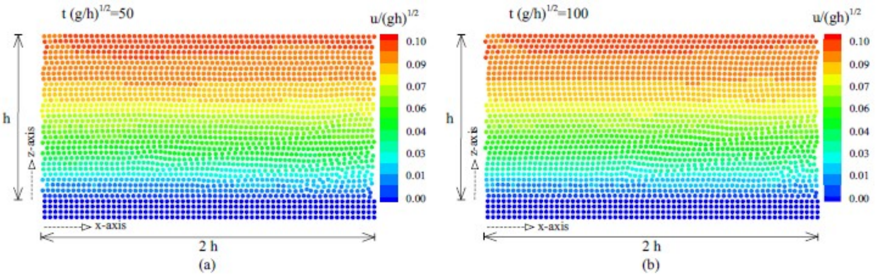

Figure 21: Particles distributions and velocity field at $t(g/h)^{1/2} = 50$ (a) and $t(g/h)^{1/2} = 100$ (b) for a free-surface channel flow in laminar regime. The Reynolds number is $Re = 10$.

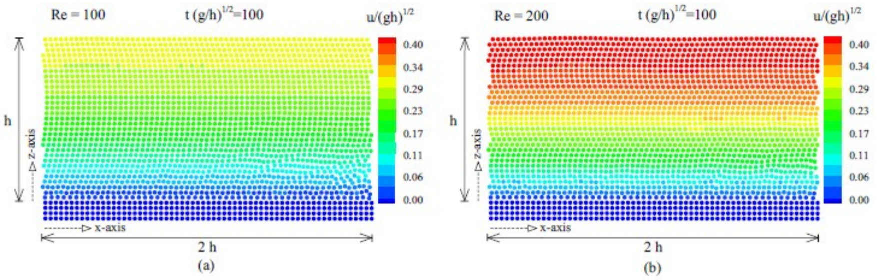

Figure 22: Particles distribution and velocity field at $t(g/h)^{1/2} = 100$ for $Re = 100$ (a) and $Re = 200$ (b).

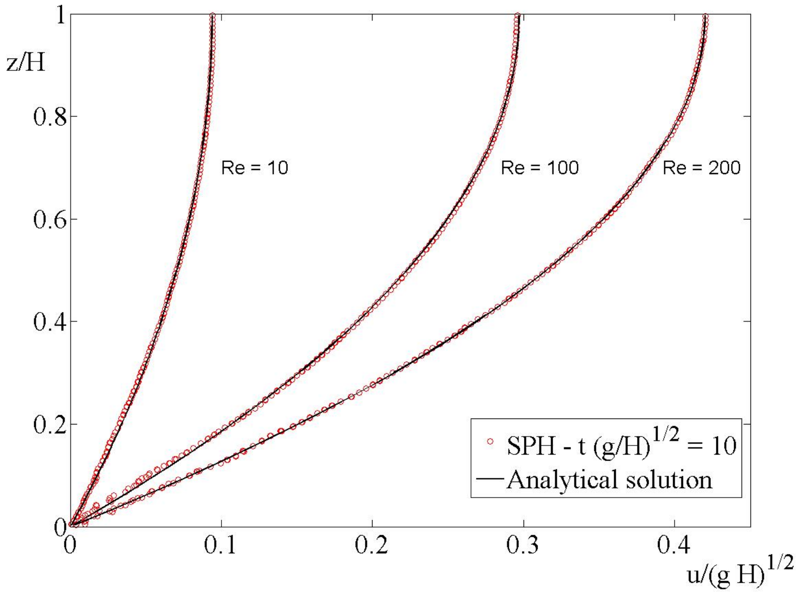

Figure 23: Comparisons between analytical solution and numerical results at $t(g/h)^{1/2} = 100$ and $x = h$ for $Re = 10$, 100 and 200.

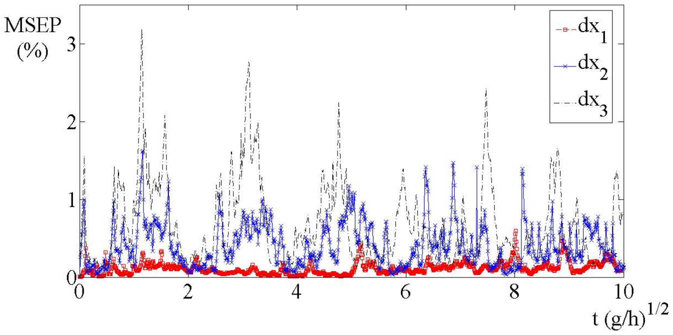

Figure 24: Time variation of MSEP for dx_1, dx_2 and dx_3 ($Re = 10$).

for the three spatial resolutions is evaluated, comparing the numerical velocity profile at $x = h$ with the analytical solution (7.1) for $Re = 10$. In particular, u^a and u^n are the analytical and numerical horizontal velocity, respectively, and N is the number of velocity values at a given time.

Figure 24 shows an enlarged view of the convergence of the scheme. Reducing the initial interparticle distance, the mean square errors decrease and the order of convergence is 1.52. The errors are less than 3.5% for the three spatial resolutions.

7.2 HYDRAULIC JUMP

In this section all the simulations are performed using the equations of system 2 in §3.4.

The hydraulic jump is a well known phenomenon in hydraulic engineering generally exploited for the dissipation of energy below structures such as spillways and outlets. Such structures are subjected to considerable pressure fluctuations due to the dynamics of turbulence and the air entrapment inside the hydraulic jump. It occurs in channels whenever the flow changes from supercritical ($Fr > 1$) to subcritical ($Fr < 1$) regime, being the Froude number $Fr = U/(gh)^{1/2}$. The literature on the macroscopic features of the hydraulic jump is quite extensive (see *e.g.* [135] [136]). However, many characteristics of the internal flow behaviour remain unanswered since there are several difficulties in experiments caused by the intense bubbly flow in the jump which does not permit efficient measurements with recent techniques as LDV and PIV [137].

A hydraulic jump in a horizontal rectangular channel with frictionless bottom has been considered. Figure 25 shows a sketch of a hydraulic jump is displayed. The symbols Fr_1 and Fr_2 are the upstream and downstream Froude numbers, h_1 and h_2 the conjugate water depths of the jump, U_1 and U_2 the mean horizontal velocity, and S_1 and S_2 the pressure forces.

In the literature (see *e.g.* [7] [138] [139] [137]), the hydraulic jump for $Fr_1 < 2.5$ is generally classified in different types: undular, breaking undular and weak. The undular jump is formed by low supercritical inflow Froude number ($1 < Fr_1 < 1.2$), and is characterized by undulations of the water surface without vortex dynamics on the crests. For

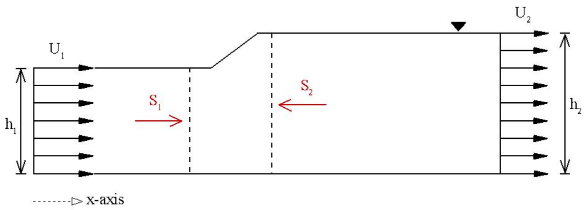

Figure 25: Sketch of a hydraulic jump with control volume.

$1.2 < Fr_1 < 1.6 - 1.7$, the jump is breaking undular: small wave breakings occur at the toe of the jump associated to vorticity generation. For $1.6 - 1.7 < Fr_1 < 2.5$, a weak jump is formed: a series of rollers develop on the surface of the jump even if the downstream water surface remains essentially smooth. It should be noted that the ranges of the Froude number given above for the various types of jump are not clear-cut but overlap to a certain extent depending on local conditions. In the present work several simulations of hydraulic jumps are performed varying Fr_1 in the above mentioned ranges.

As regards the experimental set up in horizontal channels, the hydraulic jump is typically generated by a sluice gate. Moreover, in order to confine the jump, a weir is generally placed in the channel downstream . However, the simulation of these devices is not an efficient solution in the numerical context. Indeed, particular care has to be taken to model the sluice gate and the weir. If the weir is not present, a large computational domain is needed (in SPH context see *e.g.* [140]). The use of the proposed in/outflow boundary conditions allows the sluice gate and the weir modeling to be avoided.

SPH computations are performed using the following values: $dx = 0.02h_1$, $c_0 = 10\,U_1$ and $\alpha = 0.02$.

7.2.1 Hydraulic jump with initial condition no. 1

In this section two types of jump involving a 2D channel of length $L = 40h_1$ are simulated. The first case is an undular jump characterized by $Fr_1 = 1.15$, $Fr_2 = 0.87$ and $h_2/h_1 = 1.2$. The second one is a weak jump characterized by $Fr_1 = 1.88$, $Fr_2 = 0.57$ and $h_2/h_1 = 2.2$. The upstream boundary conditions are assigned to velocity components, $u_i(t) = U_1$ and $w_i(t) = 0$, and water depth, $z_i(t) = h_1$, while the downstream ones are imposed solely on velocity, $u_o(t) = U_2$ and $w_o(t) = 0$. The initial conditions are $z_f(t = 0) = h_1$, $u_f(t = 0) = U_2$ and $w_f(t = 0) = 0$ where the latter imposes subcritical regime (see Figure 26). The sub-indexes i, f and o refer respectively to inflow, fluid and outflow particles.

When the steady state is reached the conservation of momentum requires that upstream and downstream pressure forces, S_1 and S_2, applied at the sections of the conjugate depths are equal. This implies the following relation between h_2, h_1 and Fr_1 (see *e.g.* [7]):

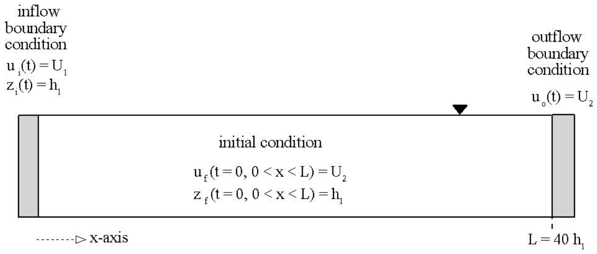

Figure 26: Sketch of in/out-flow boundary conditions and initial condition *no. 1*.

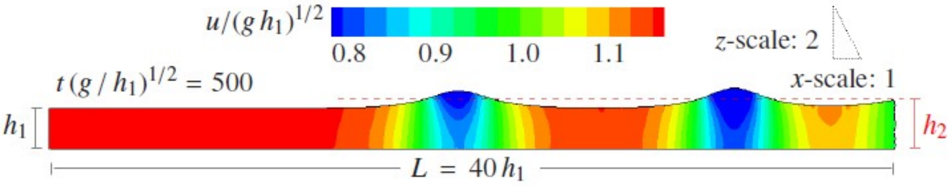

Figure 27: SPH configuration for the undular jump ($Fr_1 = 1.15$, $Fr_2 = 0.87$ and $h_2/h_1 = 1.2$) at $t(g/h_1)^{1/2} = 150$. The colours represent the horizontal component of the velocity field.

$$h_2 = \frac{h_1}{2}\left(-1 + \sqrt{1 + 8Fr_1^2}\right). \tag{7.4}$$

With reference to the undular jump with $h_2/h_1 = 1.2$, as clearly shown in Figure 27, the simulated jump at the steady state is a non-breaking undular bore, as expected. The velocity field is uniform and smooth.

In Figure 28 the generation and propagation of the weak jump ($h_2/h_1 = 2.2$) up until reaching the steady state is shown. The dashed line represents the theoretical downstream water depth h_2 evaluated through (7.4). Figure 28a displays the generation of a "shock wave" upstream of the fluid domain at $t\,(g/h_1)^{1/2} = 1$. It is caused by the sharp discontinuity between the inflow velocity that is in supercritical regime and the initialized velocity of fluid domain that is in subcritical regime. Successively, the shock wave propagates downstream generating other waves and raising the downstream water level as shown in Figure 28b at $t\,(g/h_1)^{1/2} = 50$. As soon as the downstream pressure force equals and prevails on the upstream one, the wave starts to propagate in the opposite direction (Figure 28c at $t\,(g/h_1)^{1/2} = 100$). After approximately $t\,(g/h_1)^{1/2} = 500$, the hydraulic jump reaches a steady state and the front position remains constant in x-direction (Figure 28d).

In Figure 29 the time variation of the non-dimensional upstream and downstream pressure forces $S_1/\left(\rho g h_1^2\right)$ and $S_2/\left(\rho g h_1^2\right)$ for the weak jump ($h_2/h_1 = 2.2$) is displayed. In Figure 30 the sketch for the determination of the pressure forces is shown. The balance of S_1 and S_2 is evaluated considering two elementary volumes Δx long upstream and downstream the region within the jump is developed. This fluid region has a length $2\Delta x_h$

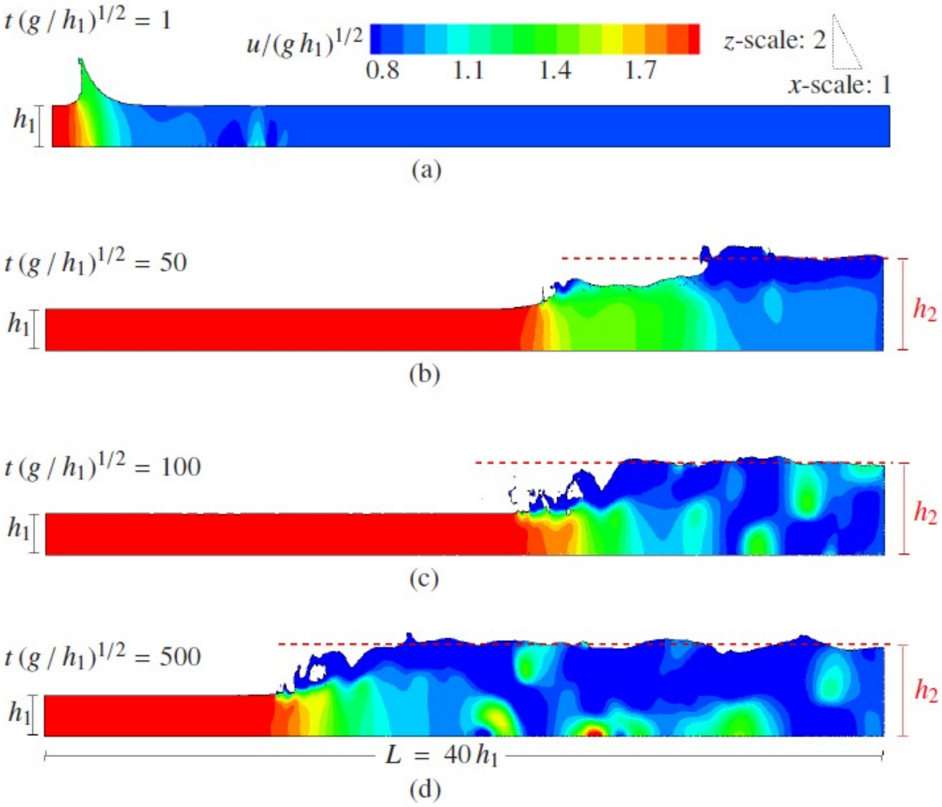

Figure 28: SPH configurations for the weak jump ($Fr_1 = 1.88$, $Fr_2 = 0.57$ and $h_2/h_1 = 2.2$) at $t(g/h_1)^{1/2} = 1$, $t(g/h_1)^{1/2} = 50$, $t(g/h_1)^{1/2} = 100$ and $t(g/h_1)^{1/2} = 500$. The colours represent the horizontal component of the velocity.

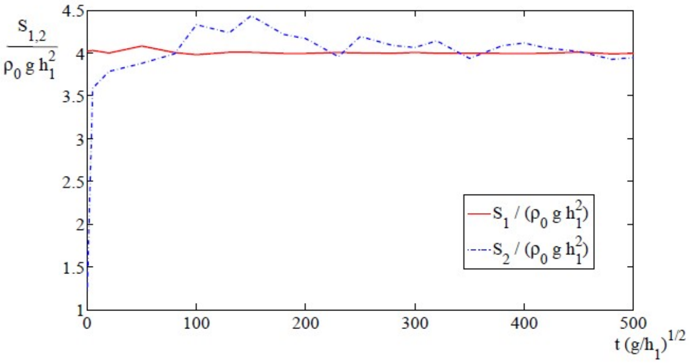

Figure 29: Time variation of the upstream and downstream pressure forces adopting the initial condition *no. 1*.

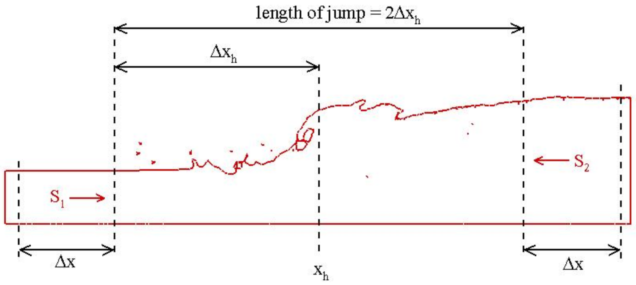

Figure 30: Sketch for the determination of the pressure forces.

with $\Delta x_h = 3(h_2 - h_1)$ (see *e.g.* [134]). The hydraulic jump front x_h is defined at each time as the x-abscissa where the water level is approximately $h_1 + 0.8(h_2 - h_1)$ [58]. The upstream and downstream pressure forces are evaluated by:

$$S_k = \frac{1}{2}\, g\, \bar{\rho}_k\, h_k^2 + \bar{\rho}_k\, \bar{U}_k^2\, h_k$$

where the parameters are defined as:

$$\bar{\rho}_k = \frac{1}{N_{\Delta x}} \sum_{a \in \Delta x} \rho_a \qquad\qquad \bar{U}_k = \frac{1}{N_{\Delta x}} \sum_{a \in \Delta x} u_a$$

with $N_{\Delta x}$ being the number of particles within each elementary volume. The sub-index k is equal to 1 or 2 depending if it refers to the upstream or downstream pressure force respectively.

7.2.2 Hydraulic jump with initial condition no. 2

Here a different initial condition is adopted with respect to §3.2.1 in order to confine the hydraulic jump in a limited fluid domain and reduce the computational cost. It is characterized by a discontinuity on water depth and velocity. Figure 31 illustrates the initial and boundary conditions, where h_2 is the theoretical water level evaluated by (9). The channel length is $L = 20h_1$ and $x_1 = 7h_1$. In this way, the hydraulic jump quickly reaches a steady state confined in the control volume, after a first transient stage. This initial condition allows simulating different cases of jump at increasing Fr_1 without increasing the length of the fluid domain, which is necessary when the initial condition *no.1* is adopted.

Six types of jumps are studied varying the Froude numbers. The values of Fr_1, Fr_2 and h_2/h_1 are reported in Table 4.

Due to the initial condition *no. 2*, all the six simulations start with a water collapse caused by the discontinuity at the free surface. The generated wave front starts to move downstream for a short time interval. After that the front propagates in the opposite direction for the remaining time evolution. After approximately $t\,(g/h_1)^{1/2} = 100$, the front position remains constant along the x-direction and the hydraulic jump reaches a steady state condition.

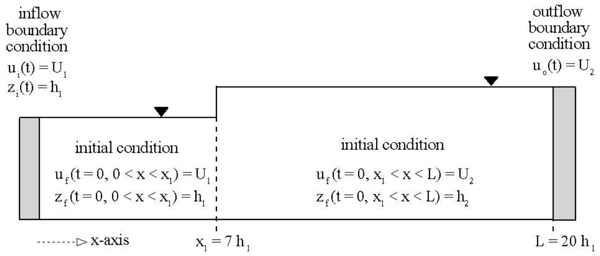
inflow boundary condition
$u_i(t) = U_1$
$z_i(t) = h_1$
outflow boundary condition
$u_o(t) = U_2$
initial condition
$u_f(t = 0, 0 < x < x_1) = U_1$
$z_f(t = 0, 0 < x < x_1) = h_1$
initial condition
$u_f(t = 0, x_1 < x < L) = U_2$
$z_f(t = 0, x_1 < x < L) = h_2$
x-axis
$x_1 = 7\,h_1$
$L = 20\,h_1$

Figure 31: Sketch of in/out-flow boundary conditions and initial condition *no. 2*.

h_2/h_1	Fr_1	Fr_2
1.5	1.37	0.75
1.7	1.51	0.68
1.8	1.59	0.66
1.9	1.66	0.63
2.1	1.80	0.59
2.2	1.88	0.57

Table 4: Upstream and downstream Froude numbers for the six hydraulic jumps varying h_2/h_1.

In Figure 32 the horizontal velocity field of the considered cases are reported for $t\,(g/h_1)^{1/2} = 150$. The simulated free-surface level downstream of the hydraulic jump is compared with the analytical one (dashed line).

The six jumps cases are characterized by intense breakings at the free surface with the generation of several vortical structures. In particular, in the cases at $h_2/h_1 = 2.1$ and $h_2/h_1 = 2.2$, that simulate a weak jump, a more violent dynamics and a non-smooth velocity field is observed, as expected. A similar behaviour is observed both in laboratory experiments (see *e.g.* [141]) as well as in numerical simulations (see *e.g.* [58]).

In Figure 33 the time variation of the non-dimensional pressure forces using the initial condition *n. 2* for the weak jump ($Fr_2/Fr_1 = 0.31$) is displayed. As clearly shown, the value of $S_2/(\rho_0 g h_1^2)$ is close to $S_1/(\rho_0 g h_1^2)$ already from the first stage allowing a balance between the two pressure forces. Adopting this condition the steady state is reached significantly before that using the initial condition *no. 1*.

In Figures 34-35, the time evolution of non-dimensional SPH water depths, z/h_1, evaluated at two gauges are compared with the non-dimensional theoretical downstream ones, h_2/h_1. The data are filtered eliminating the high frequency oscillations due to the multi-splash cycles. This make it easier to see the global behaviour of the free surface. In Figure 34 the plots represent the water levels measured at the abscissa $x_1 = 7.0h_1$, where the discontinuity of the initial conditions is located. At this position the free surface elevation recovers the theoretical downstream water depth after a first transient stage. Conversely, in Figure 35 the plots representing the water levels measured at the outflow threshold, $L = 20.0h_1$, remain close to the analytical value h_2/h_1 for the whole simulation. This is also clear

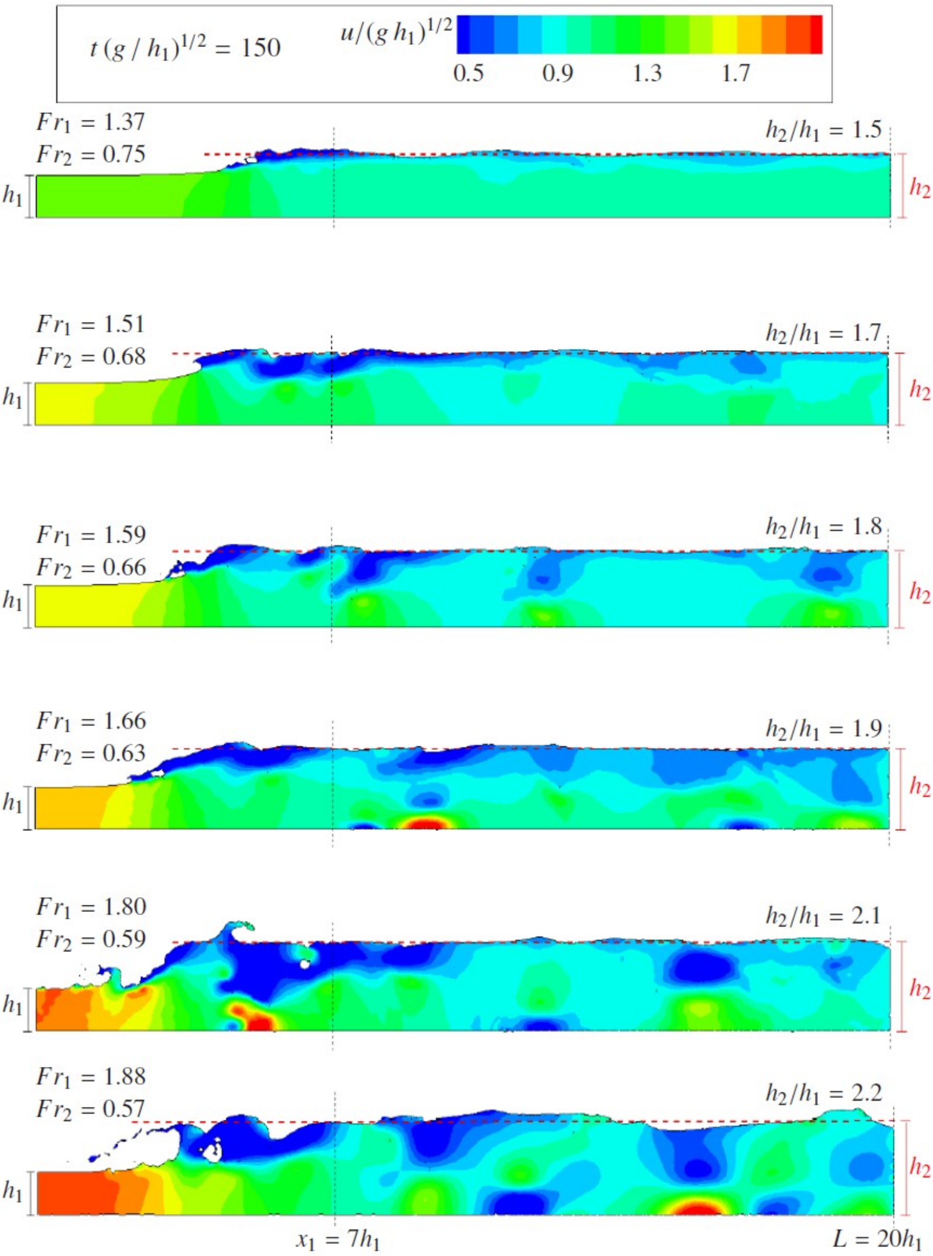

Figure 32: SPH configurations at $t(g/h_1)^{1/2} = 150$ for the considered hydraulic jumps. The colours represent the horizontal component of the velocity.

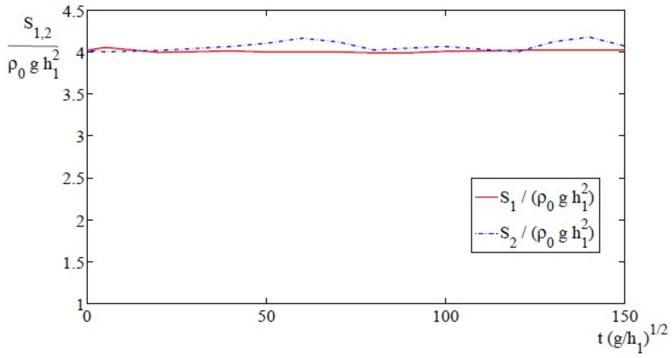

Figure 33: Time variation of the upstream and downstream pressure forces adopting the initial condition *no. 2*.

in Figure 32 where the dashed line set at h_2 overlaps with the free surface at $t\,(g/h_1)^{1/2} = 150$.

7.3 CONCLUDING REMARKS

The algorithm for the enforcement of different upstream/downstream boundary conditions presented in §5.3 has been successfully validated through the simulations of viscous free-surface channel flows in laminar regime and hydraulic jumps. For the laminar viscous case the suitability of the in/out-flow algorithm has been highlighted comparing the velocity field with the analytical Poiseuille solution.

In the second cases, different types of jump have been simulated varying the Froude numbers. The numerical downstream water depths have been compared to the theoretical ones. A particular initial conditions has been adopted that permits to maintain the jump close to its initial position without the use of any weir downstream. In this way it is possible to set a suitable computational domain to study the details of the flow field downstream the hydraulic jump.

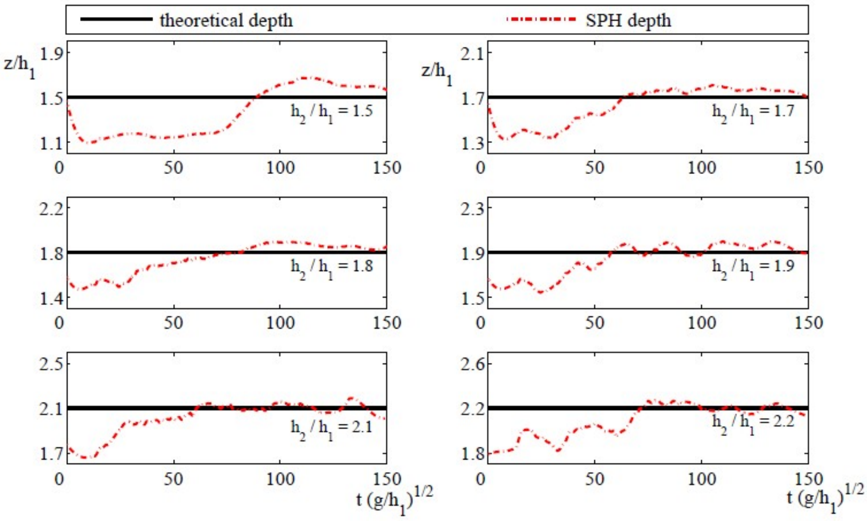

Figure 34: Comparisons between non-dimensional numerical water depths and theoretical ones at $x_1 = 7.0h_1$.

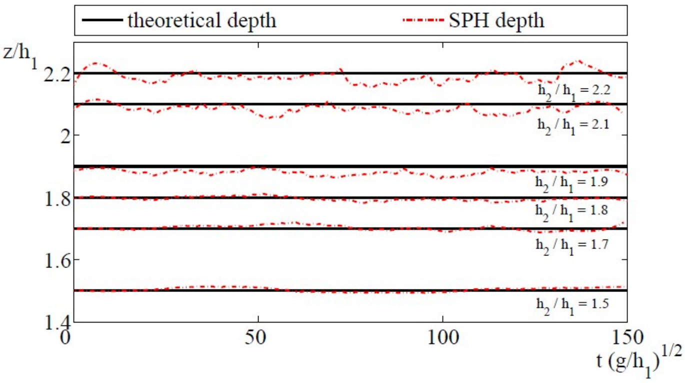

Figure 35: Comparisons between non-dimensional numerical water depths and theoretical ones at $L/h_1 = 20.0h_1$.

8 SIMULATIONS OF TWO-PHASE FLOWS

CONTENTS

8.1 Evolution of pollutant in water 73

8.2 Evolution of air in water 74

In this Chapter, the simulations refer to a circle bubble of pollutant and air in still water. In the last years, this test has become a benchmark case. It has been simulated by different authors (see *e.g.* [6], [130], [133], [5]) in order to validate two-phase model.

Here, the simulations are performed for defining the effectiveness of the implemented code. The studies in this Chapter are preparatory for the computations of the next one where the implemented two-phase model will be coupled to the proposed diffusion equations (see §4.2).

8.1 EVOLUTION OF POLLUTANT IN WATER

A bubble of pollutant having density $\rho_2 = 500\,\mathrm{kg/m^3}$ in still water ($\rho_1 = 1000\,\mathrm{kg/m^3}$) is considered. In the following the sub-indexes 1 and 2 are always refer to water and pollutant (or air in the next paragraph), respectively.

The circle bubble has the centre at $x_0 = 0.72\,\mathrm{m}$ and $z_0 = 0.48\,\mathrm{m}$, and radius $R = 0.24\,\mathrm{m}$. The measurements of the tank are $B = 1.44\,\mathrm{m}$ and $H = 2.4\,\mathrm{m}$ (see Figure 36).

The adopted discrete equations are reported in §3.4 (system 1). Furthermore, it is used the Tait's equation (3.14) as state equation assuming polytropic index $\gamma = 7$ both for pollutant and water. The initial sound speed for water is evaluated through $c_{0,1} = 14\sqrt{gR}$ as suggested by [5]. Being $B = c_0^2\rho_0/\gamma$ the parameter in state equation (3.14) and imposing $B_1 = B_2$, the pollutant sound speed assumes value $c_{0,2} = 19.8\sqrt{gR}$.

The other parameters are: $\alpha = 0.01$, $\epsilon_X = 0.3$ and $dx = 0.01\,\mathrm{m}$. The walls and the bottom of the tank are modeled through the enforcement of the *ghost particles* (see §5.2.4).

The configuration of the bubble for $t = 0\,\mathrm{s}$, $t = 0.5\,\mathrm{s}$, $t = 1.0\,\mathrm{s}$ and $t = 1.5\,\mathrm{s}$ is shown in Figure 37. Specifically, it notes the rising of pollutant bubble in time evolution caused by the different densities between the fluids. A gradual deformation of the circular shape is evident accompanied by a progressive flattening of the upper face until the bubble is shaped like an *umbrella*.

The numerical results are validated through a comparison with the analytical solution by Batchelor [111] that define the upper position of the bubble:

$$z(t) = z_s + \frac{1}{2}\sqrt{g\frac{\rho_1 - \rho_2}{\rho_1}R}\,t \tag{8.1}$$

where $z_s = 0.72\,\mathrm{m}$ is the maximum z-coordinate of the bubble at $t = 0\,\mathrm{s}$. The comparison between SPH and analytical results is reported in Figure 38. A underestimate of the upper face can be observed in the first stage. Then, a progressive agreement between SPH results and Batchelor solution is evident.

8.2 EVOLUTION OF AIR IN WATER

Here, it is considered an air bubble having density $\rho_2 = 1\,\mathrm{kg/m^3}$ in still water. The geometries of the bubble and the tank are the same of the previous case (see Figure 36).

In this case, the Grenier et *al.* [5] SPH discrete formulations is adopted (see system 4 in §3.4). Furthermore, it is used the Tait's equation (3.14) assuming polytropic index $\gamma = 7$ for water and $\gamma = 1.4$ for air. The initial sound speed for water is evaluated through $c_{0,1} = 14\sqrt{g\,R}$ (see [5]). Being $B = c_0^2\rho_0/\gamma$ the parameter in state equation (3.14) and imposing $B_1 = B_2$, the air sound speed assumes value $c_{0,2} = 198\sqrt{g\,R}$.

The other parameters are: $\chi = 0.08$, $\epsilon_X = 0.3$ and $dx = 0.01\,\mathrm{m}$. The walls and the bottom of the tank are modeled through the enforcement of the *ghost particles* (see §5.2.4).

The configuration of the bubble for $t = 0\,\mathrm{s}$, $t = 0.2\,\mathrm{s}$, $t = 0.5\,\mathrm{s}$ and $t = 0.7\,\mathrm{s}$ is shown in Figure 39. Specifically, the rising of bubble occurs faster than the previous case. The bubble shows a strong deformation to take a horseshoe shape, and at $t = 0.7\,\mathrm{s}$ splits into three main parts. Also in this case the numerical results are validated through a comparison with the

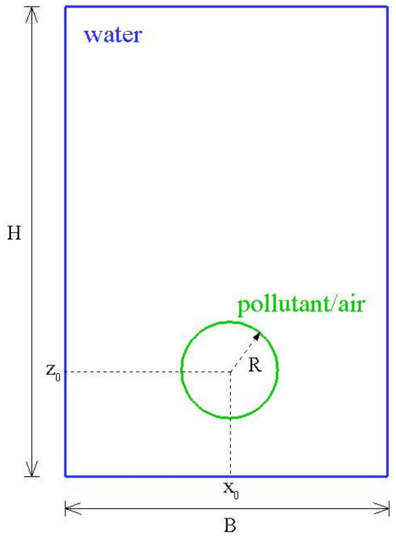

Figure 36: Sketch of the bubble in tank and adopted nomenclature.

analytical solution by Batchelor (8.1). The comparison between SPH and analytical results is reported in Figure 40. After a first slight underestimate of the bubble upper face, it notes a good agreement between SPH and analytical results.

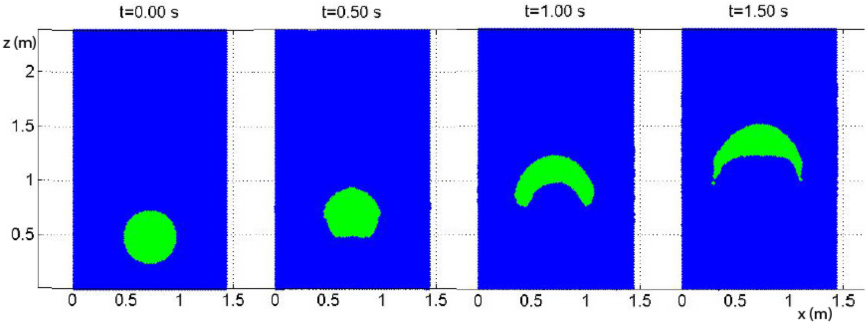

Figure 37: 2D evolution of pollutant circular bubble in still water at $t = 0.0s$, $t = 0.5s$, $t = 1.0s$ and $t = 1.5s$.

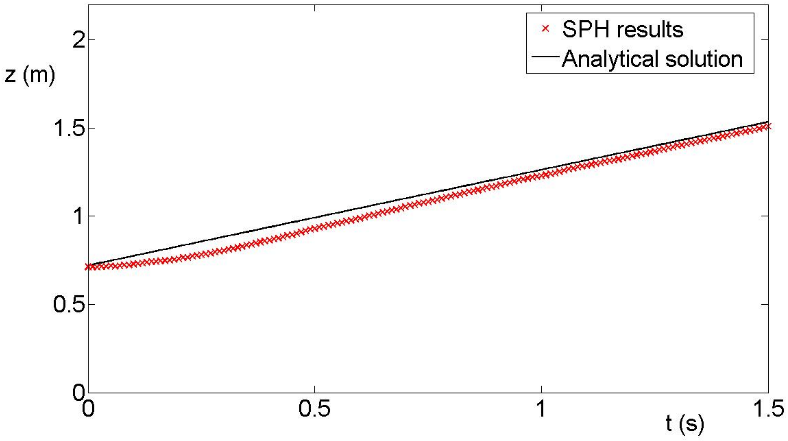

Figure 38: Time evolution of upper face for pollutant bubble: comparison between numerical results and analytical solution.

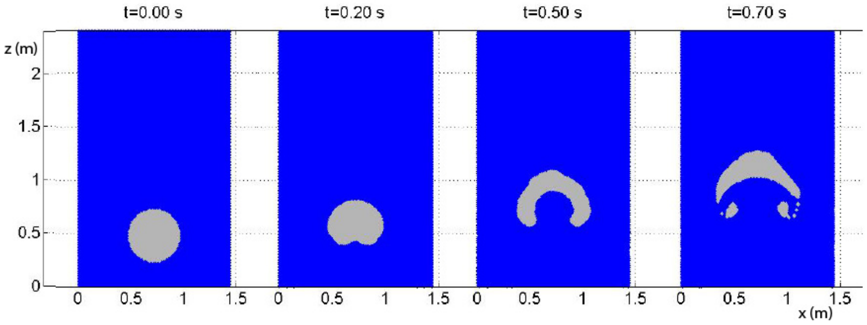

Figure 39: 2D evolution of air circular bubble in still water at $t = 0.0s$, $t = 0.2s$, $t = 0.5s$ and $t = 0.7s$.

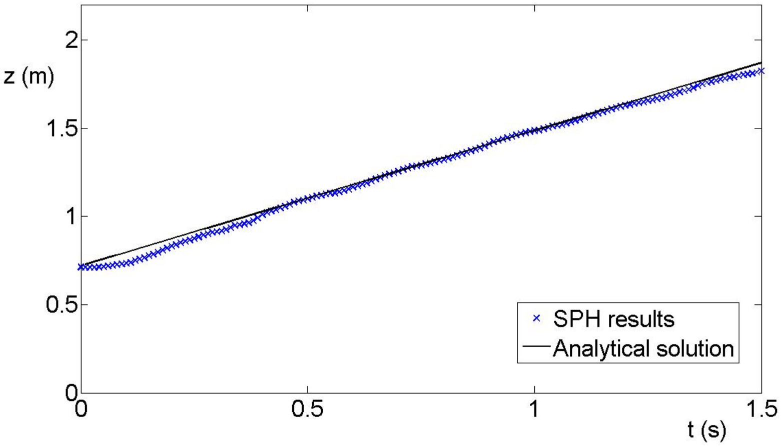

Figure 40: Time evolution of upper face for air bubble: comparison between numerical results and analytical solution.

9 SIMULATIONS OF DIFFUSION AND ADVECTIVE DIFFUSION PHENOMENA

CONTENTS

9.1 Diffusion of pollutant in water 77
  9.1.1 Strip of pollutant with initial uniform concentration. 78
  9.1.2 Strip of pollutant with initial exponential concentration. 80
  9.1.3 Bubble of pollutant with initial exponential concentration. 80
9.2 Reactive diffusion of pollutant in water 81
  9.2.1 Bubble of pollutant with initial exponential concentration. 81
9.3 Advective diffusion of pollutant in water 83
9.4 Concluding remarks 89

In this Chapter, several test cases of diffusion, advective diffusion and reactive diffusion processes are simulated in order to validated the equations derived in Chapter 4. The tests refer to strips and bubbles of pollutant with different density in still water. Numerical simulations using the proposed SPH diffusion model are compared with the lagrangian models of Zhu and Fox [89] [90] and Monaghan [104], and with analytical solutions

9.1 DIFFUSION OF POLLUTANT IN WATER

The present section reports some two-phase SPH numerical simulations applied to molecular diffusion phenomena. The proposed SPH diffusion model (Equation 4.7) is compared with diffusion models of Zhu and Fox [89] [90] and Monaghan [104], and with analytical solutions derived by the classical diffusion equation as a function of the adopted geometry and the initial concentration law of the pollutant. When the contaminant has the same initial density as the water ($\rho_0 = 1000 \text{ kg/m}^3$) and the diffusion coefficient is assumed constant during the evolution of the concentration field, SPH diffusion forms proposed by Zhu and Fox [89] [90] and Tartakovsky and Meakin [91] furnish coincident results. These two SPH models expressed by Equations (4.8) and (4.9) give different values of concentration when the pollutant density is significantly different and the diffusion coefficient is variable along the computational domain.

The numerical simulations are addressed to evaluate the spatial evolution of the concentration field in still water conditions. The process is characterized by fickian diffusion for a two-phase pollutant-water flow. Three numerical tests in a water tank have been performed:

- A vertical strip of pollutant with initial constant concentration and limited length;
- A vertical strip of pollutant with initial exponential concentration law along the whole depth of the water tank;

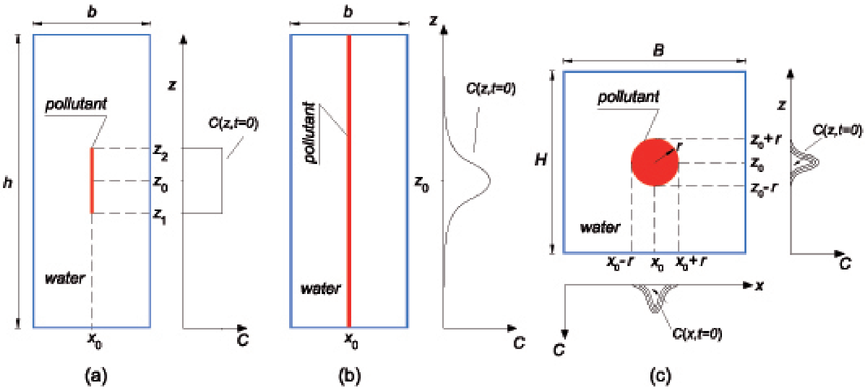

Figure 41: Geometry of the computation domains and initial concentrations for the three diffusion test cases.

- A circular bubble of contaminant with initial exponential concentration law.

Figure 41 shows a sketch of the geometries of the water tanks and the pollutants, and the shape of the assumed initial concentration laws. More detailed information on the adopted domains and the characteristics of the pollutants and the concentrations can be found in the following subsections.

The SPH fluid mechanics equations used in these simulations are reported in §3.4 (system 1). In order to optimize the numerical simulations a sensitivity analysis has been performed. On this basis the model parameters have been selected as follows. The parameter α involved in the artificial viscosity is equal to 0.01. In order to reduce the fluctuations of the velocity field the XSPH parameter ϵ_X is assumed equal to 0.1. The initial sound speed c_0 is taken as equal to $10\sqrt{gh}$, where h is the depth of the water tank. The time step Δt is computed by setting the Courant number C_{FL} equal to 1.2. The periodic re-initialization of the density is applied every 25 time steps to give a smoother pressure field.

9.1.1 Strip of pollutant with initial uniform concentration.

The first numerical simulation refers to a finite vertical strip of tracer within a rectangular water tank (see Figure 41a). The width of the strip is equal to the size of the pollutant particles. The tank is $b = 0.4$ m and $h = 1$ m and the length of the strip is equal to 0.11 m, located at $x_0 = 0.2$ m and ranging from $z_1 = 0.44$ m to $z_2 = 0.55$ m (see Figure 41a). The pollutant has an initial constant concentration $C_0 = 1$ kg/m^3 and the initial water concentration is set equal to 0. The diffusion coefficient $\mathcal{D}$ is equal to 10^{-4} m^2/s. Numerical simulations are carried out using water and pollutant particles of size $dx = 0.01$ m.

Referring to the x-position of the pollutant, the time evolution of the concentration field along z coordinate using SPH models (Equations 4.7, 4.8 and 4.10) is compared with the following analytical solution derived from the classical diffusion equation (Equation 4.1) as a function of the length and the initial constant distribution of the contaminant concentration:

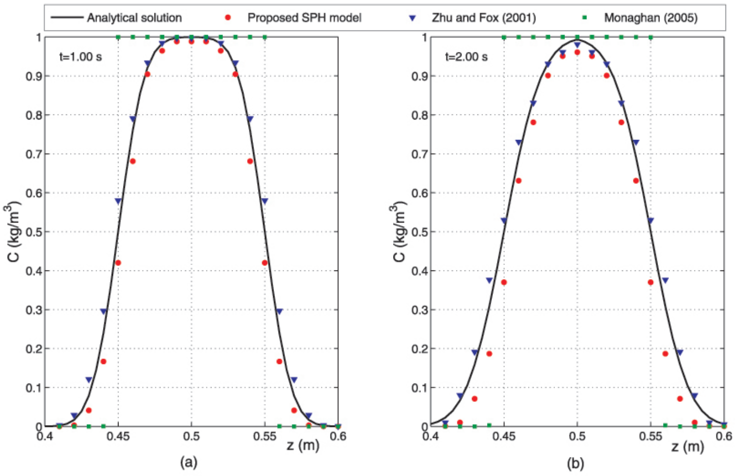

Figure 42: Comparisons between SPH diffusion models and analytical solution of the concentration field for a strip of pollutant with initial constant law (t = 1.00 s and 2.00 s).

$$C(z,t) = \frac{C_0}{2}\operatorname{erfc}\left(\frac{z_1 - z}{\sqrt{4Dt}}\right) \qquad \text{for } z \leqslant z_0 \tag{9.1}$$

$$C(z,t) = \frac{C_0}{2}\operatorname{erfc}\left(\frac{z - z_2}{\sqrt{4Dt}}\right) \qquad \text{for } z > z_0 \tag{9.2}$$

where $z_0 = 0.495$ m.

Figure 42 shows the comparisons of the proposed SPH diffusion formulation (red dots), the SPH diffusion models developed by Zhu and Fox [89] [90] (blue triangles), the results by Monaghan [104] (green squares), and the analytical solution expressed by Equations (9.1) and (9.2) (black line). The concentration field induced by an initial uniform distribution of pollutant in water for t = 1.00 s (Figure 42a) and 2.00 s (Figure 42b) is plotted. Starting from an initial concentration field having a rectangular shape the process shows a progressive reduction in the values of the concentration and a consequent symmetrical diffusion along the z-direction. SPH simulations using the present Lagrangian formulation of the diffusion equation and the solution by Zhu and Fox [89] [90] are in better agreement with the analytical solution. In this test the proposed model highlights a small underestimate of the concentration for the observed time window with respect to the model proposed by Zhu and Fox [89] [90], which however shows a small time shift for smaller values of C. A less refined estimate of the concentration values is given by the SPH formulation proposed by Monaghan [104]. This behaviour derives from a formulation characterized by a very small rate of change in the concentration with a consequent negligible decay of diffusion.

9.1.2 Strip of pollutant with initial exponential concentration.

This numerical test refers to the evolution of the concentration field induced by a vertical strip with a length equal to the depth of the water tank and a width equal to the size of the contaminant particles (see Figure 41b). As in the previous case, SPH simulations have been performed with particles having $dx = 0.01$ m. Using an initial exponential distribution of the concentration field of the pollutant:

$$C\,(z, t = 0) = exp\left[-\frac{(z - z_0)^2}{4Dt_0}\right] \tag{9.3}$$

the analytical solution of this diffusion problem is expressed as follows:

$$C\,(z, t) = \frac{c_0}{\sqrt{t + t_0}} exp\left[-\frac{(z - z_0)^2}{4D(t + t_0)}\right] \tag{9.4}$$

where t_0 = 1 s, $c_0 = 1$ kg $s^{1/2}/m^3$ and D = 10^{-4} m^2/s.

Figure 43 shows the plots of the concentration field of a two-phase pollutant-water flow at t = 1.00 s (Figure 43a) and 2.00 s (Figure 43b) obtained by SPH diffusion models versus the analytical solution expressed by Equation 9.4. The plots refer to the vertical middle section of the tank. The concentration has initially a gaussian shape and its evolution shows a progressive decay of all the values. As in the case of the initial uniform concentration (see Figure 42) the symmetry with the respect to the peak value of the concentration is time preserved. With reference to the analytical solution the use of the proposed SPH diffusion model furnishes in this case better results than the different Lagrangian diffusion formulations. In particular the SPH diffusion form proposed by Zhu and Fox [89] [90] overestimates the maximum values of concentration and underestimates the lower values. The rate of change of the concentration obtained by this formulation proves to be twice the value furnished by the proposed SPH model. As observed for the strip with initial uniform concentration, SPH diffusion modelling by Monaghan [104] exhibits a very small decrease in the diffusion process.

9.1.3 Bubble of pollutant with initial exponential concentration.

In this test the concentration field of a circular bubble of pollutant in a square water tank, having the centre at $x_0 = 1.2$ m and $z_0 = 1.2$ m and radius $r = 0.2$ m, is simulated. The measurements of the tank are $B = 2.4$ m and $H = 2.4$ m. The fluid particles have an initial interparticle distance equal to 0.03 m. The diffusion coefficient is equal to 10^{-3} m^2/s. The initial concentration follows the exponential law expressed by Equation (9.3) along the radius of the bubble, exhibiting an axial symmetric reduction from the centre to the boundary (see Figure 41c).

The comparison of the evolution of the concentration between the SPH diffusion models and the analytical relationship expressed by Equation 9.4 are plotted along z in Figure 44a and b for t = 1.00 s and 2.00 s, respectively. Also in this case the symmetry of the phenomenon and a gradual decay of

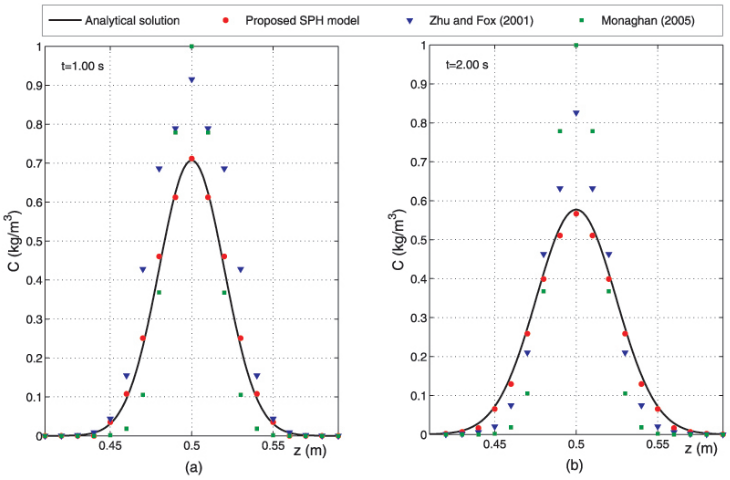

Figure 43: Comparisons between SPH diffusion models and analytical solution of the concentration field for a strip of pollutant with initial exponential law (t = 1.00 s and 2.00 s).

the concentration is observed. The present numerical results show the better performance of the proposed SPH diffusion model in comparison with the other diffusion models. In this case the behaviour of the model proposed by Zhu and Fox [89] [90] appears to be more accurate with respect to the case of the strip (see Figure 43). Monaghan's model [104] shows the same limitations as the previous numerical tests.

Finally, a comparison based on the maximum value of concentration (C_{max}) between the proposed diffusion model and the analytical solution is shown (see Figure 45) varying the diffusion coefficient $\mathcal{D}$ in the range $10^{-3} \div 10^{-4}\ m^2/s$.

It notes that in a first stage a slight overestimate occurs. After that, a good agreement between numerical and analytical results is clearly shown.

9.2 REACTIVE DIFFUSION OF POLLUTANT IN WATER

9.2.1 Bubble of pollutant with initial exponential concentration.

Another case based on kinetics reaction is performed considering a pollutant bubble in a still water tank having the same features of the previous one (see Figure 41c).

Here, the reactive diffusion SPH equation introduced in §4.2.3 is compared with the analytical relationship derived by the classical diffusion equation (Equation 4.1) and adding a first-order kinetics reaction:

$$C(z,t) = \frac{c_0}{\sqrt{t+t_0}} \exp\left[-\frac{(z-z_0)^2}{4D(t+t_0)}\right] \exp[-\mathcal{R}C] \qquad (9.5)$$

where the reaction coefficient is evaluated through the Lewis-Whitman theory [123]: $\mathcal{R} = \mathcal{D}/\delta$, being $\delta = 2\epsilon$ the mixing layer and ϵ the length

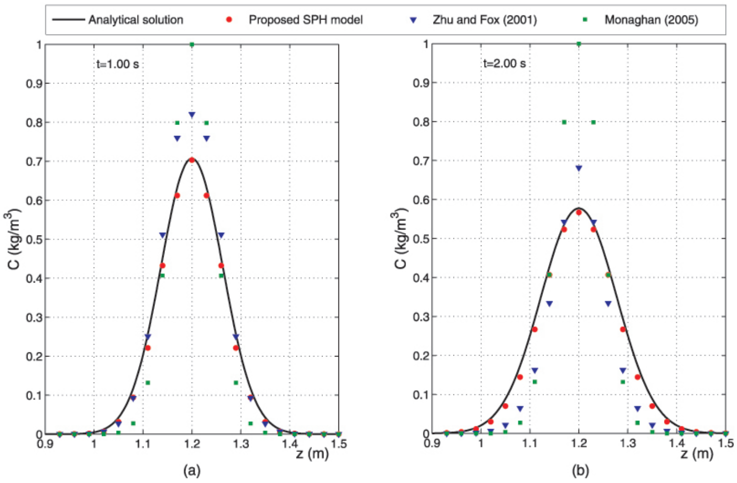

Figure 44: Comparisons between SPH diffusion models and analytical solution of the concentration field for a bubble of pollutant with initial exponential law (t = 1.00 s and 2.00 s).

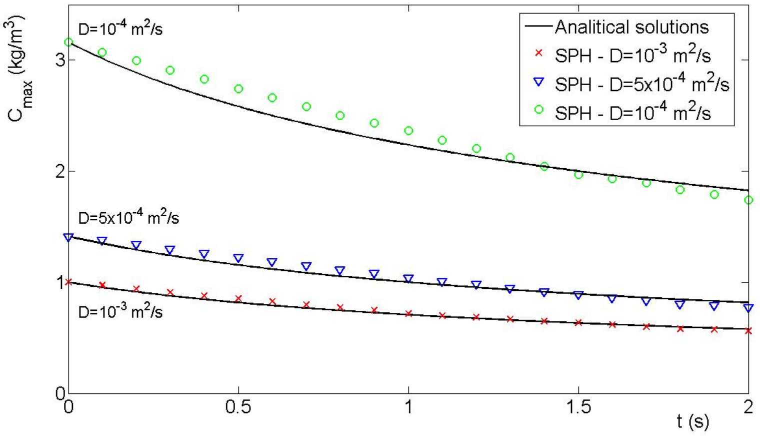

Figure 45: Maximum concentration curves C_{max}: comparison between SPH and analytical results varying the diffusion coefficient.

of the compact support of kernel (see §4.2.3). A sketch representing the mixing layer for the bubble of pollutant is shown in Figure 46.

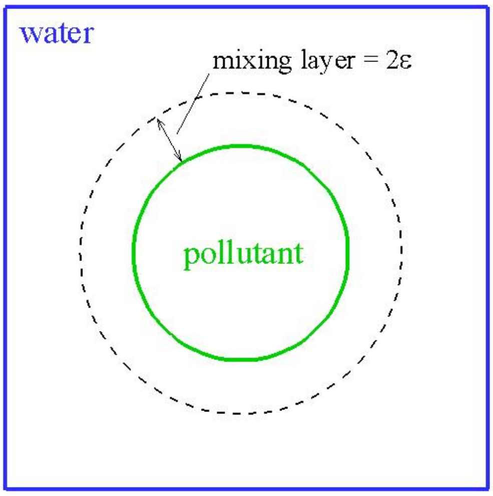

Figure 46: Sketch of the mixing layer for the bubble of pollutant.

Also in this case the comparison is based on the maximum value of concentration (C_{max}). The simulations referred to $\mathcal{D} = 10^{-3}\ m^2/s$ are reported in Figure 47, where the reactive diffusion SPH results (named "SPH RD Eq." in Figure 47) are compared with the analytical one ("Analytical solution RD Eq." in Figure 47). Also in this case after a first stage, it notes a good agreement between numerical and analytical solutions. Furthermore, it is evident a decay caused by the negative reaction that reduce the maximum values of concentration in comparison with the maximum diffusion curves (named "Analytical solution D Eq." and "SPH D Eq." in Figure 47).

9.3 ADVECTIVE DIFFUSION OF POLLUTANT IN WATER

Numerical modelings dealing with advective diffusion phenomena of two-phase flows using a wide range of pollutant densities less than the water are reported here. The tests refer to the problem of a circular bubble of pollutant in a square water tank. SPH results obtained by the proposed SPH model in the solution of the advective diffusive equation expressed by Equation (4.12) are compared with available analytical relationships. For the following simulations the water tank, the radius of the bubble, the diffusion coefficient and the interparticle distance are the same as the previous diffusion test case.

SPH simulations of advective diffusion tests have been carried using the following model parameters: $\alpha = 0.01$, $\varepsilon = 0.1$, $C_{FL} = 1.2$ and $\tau = 25$.

Adopting again the initial exponential concentration field along the radius, the analytical solution of the advective diffusion equation problem is expressed as follows [119]:

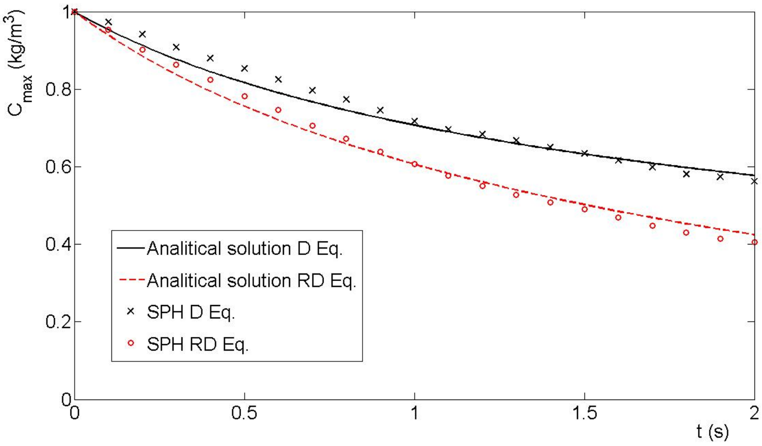

Figure 47: Maximum concentration curves C_{max}: comparison between SPH and analytical results considering diffusion and reactive diffusion processes.

$$C(x,z,t) = \frac{c_0}{\sqrt{t+t_0}} \exp\left[-\frac{(x-x_0)^2}{4D(t+t_0)} - \frac{(z-z_0-Vt)^2}{4D(t+t_0)}\right] \tag{9.6}$$

where $t_0 = 1$ s, $c_0 = 1\ \mathrm{kg\,s^{1/2}/m^3}$ and V is the vertical mean velocity of the pollutant, evaluated analytically by the following relationship [111]:

$$V = \frac{1}{2}\sqrt{g\frac{\rho_1-\rho_2}{\rho_1}r} \tag{9.7}$$

This analytical solution of V has been verified with a numerical solution based on a two-phase SPH modeling carried out in Chapter 6.

As observed above, if the density ratio between pollutant and water is not close to 1, the evolution of the concentration in still water conditions is characterized by the phenomenon of fickian diffusion and the contribution of natural advection has to be added. This process requires that the kinematic field be taken into account for a correct modeling of advective diffusion phenomena. The use of the simple SPH diffusion model (see Equation 4.7), like the other diffusion formulations, does not perform well in the evaluation of the contribution of the velocity field induced by differences between the fluid densities. The SPH diffusion formulation allows only a part of the general phenomenon of advection diffusion to be considered. For $t = 0.00$ s (black dots), 0.20 s (red triangles) and 0.50 s (blue squares), Figure 48 highlights the limitations of a SPH diffusion modeling to simulate accurately the evolution of the concentration field induced by a two-phase contaminant-water flow having low density ratios. In particular SPH simulations using Equation (4.7) are compared with the analytical solution expressed by Equation (9.6) (black, red and blue line) for a density ratio $\rho_2/\rho_1 = 0.3$. The values of the simulated concentration are time shifted and a poor evaluation of the maximum values with respect to the analytical relationship is found.

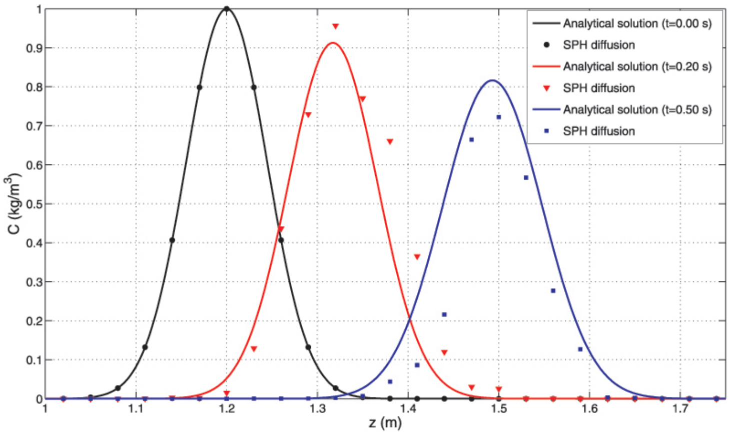

Figure 48: Comparisons between the proposed SPH diffusion model and analytical solution of the concentration field for a bubble of pollutant with initial exponential law and $\rho_2/\rho_1 = 0.3$ ($t = 0.00$ s, 0.20 s and 0.50 s).

An improvement in the evaluation of the concentration field for a wide range of density ratios can be performed using the proposed SPH model for the solution of the advective diffusion equation (see Equation 4.12). Figure 49 shows the comparison between SPH advective diffusion model and the analytical solution expressed by Equation (9.6). SPH simulations prove to be now in better agreement with the analytical equation with respect to the simple SPH diffusion model, exhibiting a reduced time shift and determining the peak values accurately. The movement of the pollutant mass is dependent on the natural advection phenomenon induced by low density ratio between the fluids. In order to check the capabilities of the present SPH advective diffusion model, another comparison between the model and the analytical solution is reported in Figure 50 for $t = 0.00$ s, 0.20 s and 0.50 s, and $\rho_2/\rho_1 = 0.5$.

For a bubble of pollutant in water with an initial exponential concentration, Figure 51 a and b show in the 2D domain the initial spatial arrangement of the fluid particles and the concentration field simulated by the proposed SPH advective diffusion model for $t = 0.00$ s and $\rho_2/\rho_1 = 0.5$. Figure 52 a and b and Figure 53 a and b report the spatial distribution of the particle with the associated velocity vectors, and the concentration field for successive times equal to 0.20 s and 0.50 s. In Figures 51, 52 and 53, blue dots and arrows are referred to the water particles and their velocity magnitude, red dots and arrows to the pollutant. SPH numerical simulations describe the arising and the deformation of the bubble in the water tank induced by the different density between pollutant and water. The kinematic field shows a progressive increase, emphasizing the importance of taking into account the velocity to model an advective diffusion process. The concentration field evolves following the movement of the bubble, resulting in a progressive asymmetric shape along the depth. A gradual deformation of the boundary of the concentration field and a temporal decay of all values can be observed. A consequent growth in the pollutant concentration for the particles having an initial concentration close to 0 is

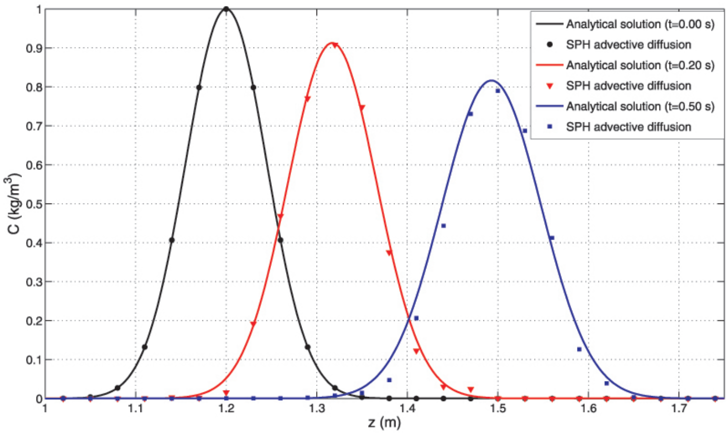

Figure 49: Comparisons between SPH advective diffusion model and analytical solution of the concentration field for a bubble of pollutant with initial exponential law and $\rho_2/\rho_1 = 0.3$ ($t = 0.00$ s, 0.20 s and 0.50 s).

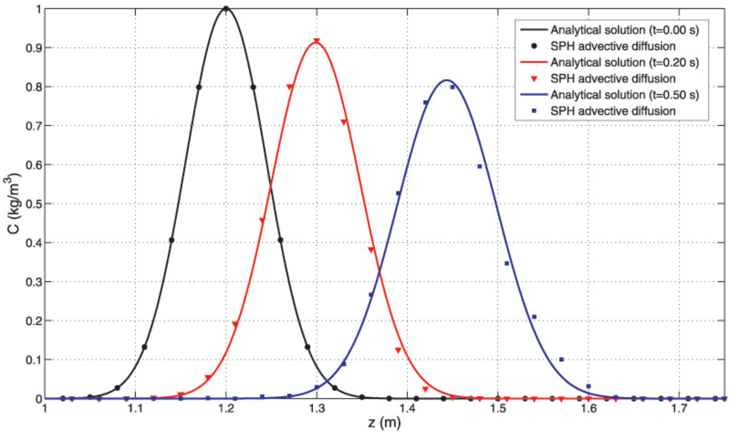

Figure 50: Comparisons between SPH advective diffusion model and analytical solution of the concentration field for a bubble of pollutant with initial exponential law and $\rho_2/\rho_1 = 0.5$ ($t = 0.00$ s, 0.20 s and 0.50 s).

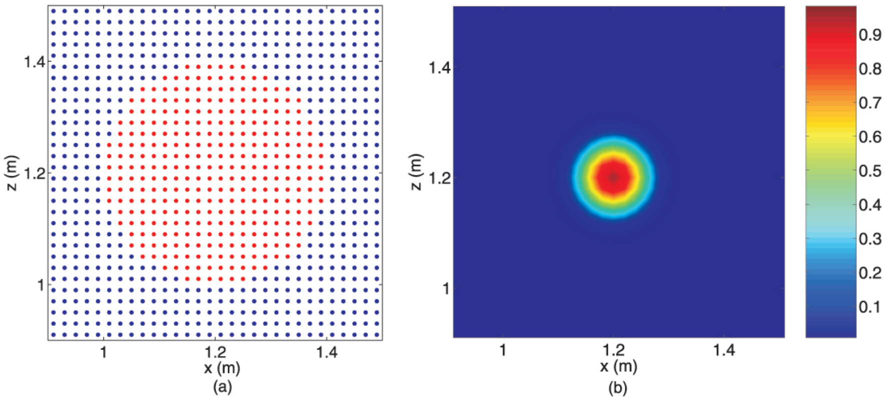

Figure 51: Two-dimensional spatial distribution of particle velocities and concentration field of a bubble of pollutant with initial exponential concentration for $\rho_2/\rho_1 = 0.5$ (t = 0.00 s).

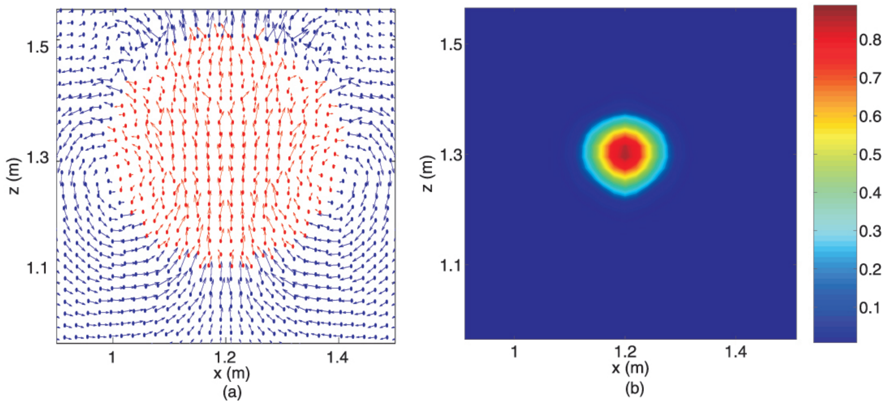

Figure 52: Two-dimensional spatial distribution of particle velocities and concentration field of a bubble of pollutant with initial exponential concentration for $\rho_2/\rho_1 = 0.5$ (t = 0.20 s).

also produced. For the analyzed time intervals the water particles are not influenced by the advective diffusion process but they play an important role in the transport of the contaminant mass.

Figure 54 shows at $t = 0.00$ s, 0.20 s and 0.50 s a three-dimensional view of the evolution of the concentration field having an initial exponential concentration for $\rho_2/\rho_1 = 0.5$. The concentration tends to propagate following the movement of the pollutant. The decrease in the concentration is associated to a radial expansion within the water tank.

The performances of the proposed SPH diffusion model (Equation 4.7) and the advective diffusion model (Equation 4.12) in simulating an advective diffusion phenomenon are investigated for density ratios between pollutant and water ranging from 0.1 and 1. These SPH models are compared with the analytical solution of the advective diffusion equation (Equation 9.6) on the basis of the root mean square error:

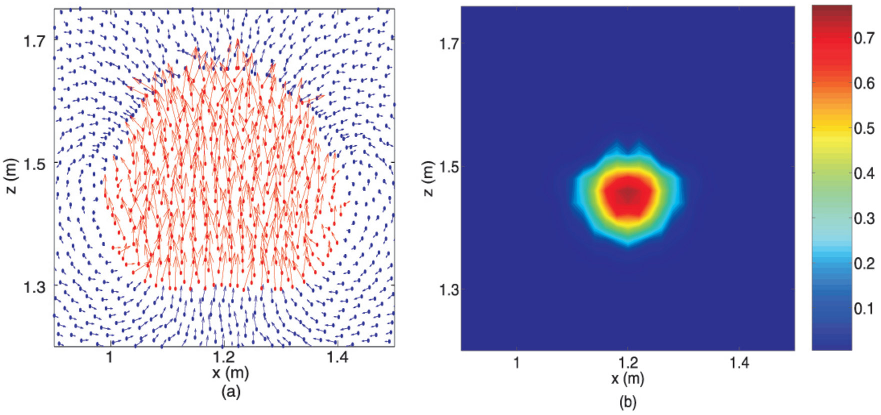

Figure 53: Two-dimensional spatial distribution of particle velocities and concentration field of a bubble of pollutant with initial exponential concentration for $\rho_2/\rho_1 = 0.5$ (t = 0.50 s).

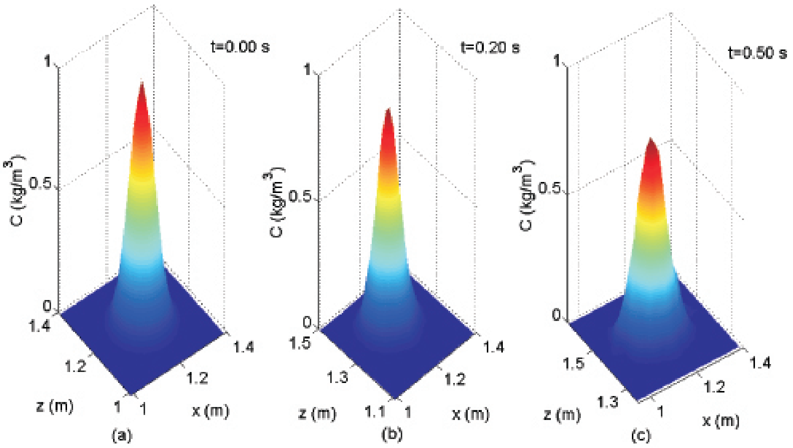

Figure 54: Three-dimensional view of the evolution of the concentration field of a bubble of pollutant with initial exponential concentration for $\rho_2/\rho_1 = 0.5$ (t = 0.00 s, 0.20 s and 0.50 s).

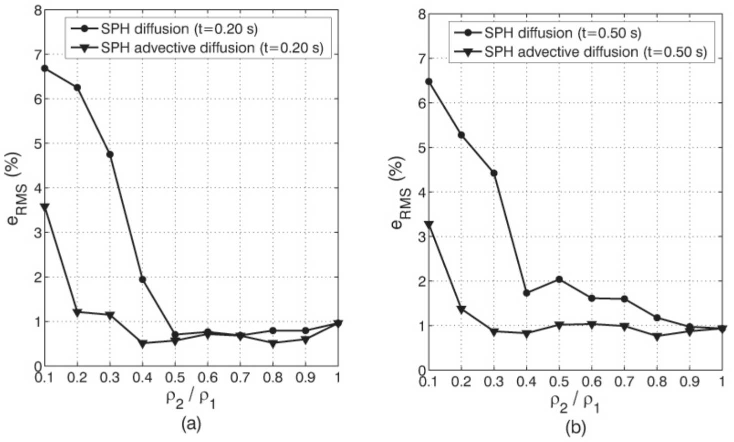

Figure 55: Root mean square errors vs. density ratios between pollutant and water (t = 0.20 s and 0.50 s).

$$e_{RMS} = \sqrt{\frac{1}{(N-1)} \sum_{j=1}^{N} \left(C_{aj} - C_{nj}\right)^2} \tag{9.8}$$

where C_a and C_n are the analytical and numerical concentrations, respectively, and N is the number of the concentration values at a given time instant.

Figure 55 a and b show the percentage values of e_{RMS} as a function of the density ratio between pollutant and water for t = 0.20 s and 0.50 s, respectively. It is worth noting that the simple SPH diffusion model makes comparable errors with respect to the SPH advection diffusion model until about ρ_2/ρ_1 = 0.50 for t = 0.20 s, and ρ_2/ρ_1 = 0.8 for t = 0.50 s. The reduction in the density ratio is directly related to an increase in the velocity field and, consequently, the SPH diffusion model gives a progressive poorer evaluation of the concentration field. The use of the SPH advective diffusion modeling furnishes lower values of e_{RMS}. Thus, the contribution of the advective term plays a relevant role in the modeling of natural advective cases. For the cases of advective diffusion in still water, the present analysis shows that a simple SPH diffusion model is able to evaluate only the first evolution of the process, in the presence of high values of the density ratio.

9.4 CONCLUDING REMARKS

This Chapter is concerned with numerical models for the analysis of diffusion and advective diffusion phenomena. The proposed SPH diffusion formulation (see Chapter 4) has been coupled to the fluid dynamic equations (see Chapter 3) with a description of diffusion, reactive diffusion and advective diffusion processes, within the framework of the SPH formalism. In this context a numerical meshless model has been developed which allows the approximate description of molecular diffusion and natural advection.

Environmental engineering problems, concerning diffusion and natural advection of a pollutant in still water, have been studied. In particular, the numerical simulations have been used to evaluate the evolution of the concentration field of a strip and a bubble of pollutant in a water tank starting from initial concentration distributions.

Numerical simulations of the concentration field induced by a two-phase flow with the same density show that the proposed SPH diffusion model is more accurate than other Lagrangian diffusion models. For relevant differences between the fluid densities, the spatial evolution of the concentration due to the coupled effect of fickian diffusion and natural advection has been modeled with a SPH advective diffusion model which takes into account the presence of a velocity field. The results obtained by this model show a good agreement with analytical solutions. The comparison of the capabilities of the proposed SPH diffusion and advective diffusion models in simulating an advective diffusion phenomenon for a wide range of density ratios shows that a simple SPH diffusion formulation gives a satisfactory modeling of the concentration field only for high density ratios.

The proposed SPH models could be extended to the turbulent diffusion and dispersion processes for applications to large scale hydrodynamic problems.

10 CONCLUSIONS AND FUTURE PERSPECTIVES

The thesis treated Computational Fluid Dynamics based on particle methods. The fully Lagrangian approach Smoothed Particle Hydrodynamics (SPH) has been developed for two-phase flows and open-channel flows. The model has been extended to research fields of environmental and river hydraulic.

Firstly, an algorithm has been developed to treat upstream/downstream boundary conditions for 2D open-channel flows in SPH context. For this purpose two suitable sets of particles (in/out-flow particles) have been defined allowing the enforcement of different upstream and downstream flow conditions. As first test case, the proposed algorithm has been validated for a viscous laminar flow in open channel. The obtained results have been compared with analytical ones in order to heuristically check the convergence of the numerical scheme. The suitability of the in/out-flow algorithm has been highlighted comparing the velocity field with the analytical Poiseuille solution. The second test case has been dealt with a hydraulic jump for which different upstream and downstream conditions are needed. Several types of jumps, obtained varying the flow Froude number, have been investigated with particular reference to the location of the jump and the velocity field. Comparisons between the numerical results and the classical theory of the hydraulic jump have been provided, showing good agreements.

In the second part, the SPH model has been applied to evaluate the concentration field of pollutants in water. A Lagrangian formalism has been formulated to solve the fickian diffusion equation considering pollutants with the same density as the water. Furthermore, a SPH form of the advective diffusion equation has been also developed for pollutant-water, taking into account the effects of molecular diffusion and natural advection induced by differences between the fluid densities. Numerical tests referring to a strip and a bubble of contaminant in a water tank with different initial concentration laws have been carried out. The results obtained by the proposed SPH models have been compared with other available SPH formulations, showing an overall better agreement with standard analytical solutions in terms of spatial evolution of the concentration values. Capabilities and limits of the proposed SPH models to simulate advective diffusion phenomena for a wide range of density ratios have been discussed. The proposed SPH models could be extended to the turbulent diffusion and dispersion processes for applications to large scale hydrodynamic problems.

As future perspectives, the capabilities of SPH model will be considered in simulations of long 3D open channels. These kinds of simulations mean an increase of computing costs that will be avoided through the extension of SPH code from serial language to *OpenMP* parallel one. This will allow running code using millions of particles. Futhermore, the SPH method will be applied to the Graphics Processing Unit (*GPU*) instead the Central Processing Unit (*CPU*) in order to reduce considerably the running costs. These computational improvements will be exploit for hydraulic simulations of complex geometry channels and different upstream/downstream boundary conditions. The first aim is to test the model for hydraulic jumps in 3D open channels varying Froude number. Laboratory experiments will be carried out in order to provide comparisons with numerical results. Other comparisons will be provided adopting Eulerian *CFD* solvers.

Then, the model will be extended to several environmental hydraulic cases. It will be simulated pollutant jets in free-surface channels in order to evaluate the evolution dynamics that will be compared to experimental investigastions. Furthermore, the concentration field will determined through the implementation of diffusion, advective diffusion and reactive diffusion equations. Moreover, SPH results will be compared with other *CFD* methods based on *VOF* (Volume-Of-Fluid) approach.

A further purpose will be the development of two-phase SPH model for water-sediments interaction cases, taking into account stress tensor effects. Local scouring phenomena will be simulated for open channels in uniform and non-uniform steady flows. Laboratory experiments will be also performed in order to show comparisons with numerical scour depth.

Finally, the two-phase sediment-water model will be extended to fluvial geomorphology problems. Plane large scale cases of river networks generation will be treated considering straight, meandering or braided paths.

BIBLIOGRAPHY

[1] L. Lucy. *A Numerical approach to the Testing of Fission Hypothesis*. The Astronomical Journal, 82(12), 1013-1024, 1977.

[2] R. Gingold R and J.J. Monaghan. *Smoothed particle hydrodynamic: theory and application to non-spherical stars*. Monthly Notices of the Royal Astronomical Society, 181, 375-389, 1977.

[3] W. Benz. *Smooth particle hydrodynamics: a review*. In B.J.R. (Ed.), the numerical modelling of nonlinear stellar pulsation, Kluwer Academic Publisher, 269-288, 1990.

[4] J.J. Monaghan. *Simulating free surface flows with SPH*. Journal of Computational Physics, 110, 399-406, 1994.

[5] N. Grenier, M. Antuono, A. Colagrossi, D. Le Touzé and B. Alessandrini. *An Hamiltonian interface SPH formulation for multi-fluid and free surface flows*. Journal of Computational Physics, 228, 8380-8393, 2009.

[6] A. Colagrossi and M. Landrini. *Numerical simulation of interfacial flows by smoothed particle hydrodynamics*. Journal of Computational Physics, 191, 448-475, 2003.

[7] V.T. Chow, *Open-channel hydraulic*, McGraw-Hill, New York, 1959.

[8] W.G. Hoover. *Isomorphism linking smooth particles and embedded atoms*. Physica A, 260:244-254, 1998.

[9] W.G. Hoover, C.C. Hoover and E.C. Merritt. *Smooth particle applied mechanics: conservation of angular momentum with tensile stability and velocity averaging*. Physical Review E, 69:016702, 2004.

[10] T. Belytschko, Y. Krongauz, D. Organ, M. Fleming, and P. Krysl. *Meshless methods: An overview and recent developments*. Computer Methods in Applied Mechanics and Engineering, 139:3-47, 1996.

[11] A. Colagrossi. *A Meshless Lagrangian Method for Free-Surface and Interface Flows with Fragmentation*. PhD thesis, 1-219, 2005.

[12] M. Griebel and M. A. Schweitzer. *Meshfree Methods for Partial Differential Equations*. Springer, 2002.

[13] G. R. Liu. *Meshfree Methods*. CRC Press, 2002.

[14] G. R. Liu and M. B. Liu. *Smoothed Particle Hydrodynamics: A meshfree particle method*. World Scientific, 2003.

[15] J. P. Vila. *On particle weighted methods and smooth particle hydrodynamics*. Mathematical Models and Methods in Applied Science, 9:161-209, 1999.

[16] F. H. Harlow. *The particle-in-cell computing method for fluid dynamics*. Methods in Computational Physics, 3:319-343, 1964.

[17] F. H. Harlow and J. E.Welch. *Numerical calculation of time-dependent viscous incompressible flow of fluid with free surface*. Physics of Fluids, 8:2182-2189, 1965.

[18] F. H. Harlow and J. E. Welch. *Numerical study of large-amplitude free-surface motions*. Physics of Fluids, 9:842-851, 1966.

[19] R. K.-C. Chan and R. L. Street. *A computer study of finite-amplitude water waves*. Journal of Computational Physics, 6:68-94, 1970.

[20] V. Armenio. *An improved MAC method (SIMAC) for unsteady high-Reynolds free surface flows*. International Journal For Numerical Methods in Fluids, 24:185-214, 1997.

[21] J. A. Viecelli. *A computing method for incompressible flows bounded by moving walls*. Journal of Computational Physics, 8:119-143, 1971.

[22] J. U. Brackmill and H. M. Ruppel. *FLIP: A method for adaptively zoned, particle-in-cell calculations of fluid flows in two dimensions*. Journal of Computational Physics, 65:314-343, 1986.

[23] D. Sulsky, Z. Chen, and H. L. Schreyer. *A particle method for historydependent materials*. Computer Methods in Applied Mechanics and Engineering, 118:179-196, 1994.

[24] D. Sulsky and H. L. Schreyer. *Axisymmetric form of the material point method with applications to upsetting and Taylor impact problems*. Computer Methods in Applied Mechanics and Engineering, 139:409-429, 1996.

[25] D. Sulsky, S.-J. Zhou, and H. L. Schreyer. *Application of a particle-in-cell method to solid mechanics*. Computer Physics Communications, 87:236-252, 1995.

[26] B. Banerjee. *Material point method simulations of fragmenting cylinders*. Proceeding of 17th ASCE Engineering Mechanics Conference, 2004.

[27] D. Shepard. *A two-dimensional interpolation function for irregularly spaced data*. Proceeding of the 23rd Association for Computing Machinery National Conference, Princeton, NJ: Brandon/Systems Press, 517-524, 1968

[28] P. Lancaster and K. Salkauskas. *Surfaces Generated by Moving Least Squares Methods*. Mathematics of Computation, 37 , 141-158, 1981.

[29] B. Nayroles, G. Touzot and P. Villon. *Generalizing the finite element method: Diffuse approximation and diffuse elements*. Computational Mechanics, 10, 307-318, 1992.

[30] T. Belytschko, Y. Y. Lu and L. Gu. *Element-Free Galerkin methods*. International Journal for Numerical Methods in Engineering, 37, 229-256, 1994.

[31] D. Hietel, K. Steiner and J. Struckmeier. *A finite volume particle method for compressible flows*. Mathematical Models and Methods in Applied Science, 10:1363-1382, 2000.

[32] R. Keck. *The finite volume particle method: a meshless projection method for incompressible flow*. PhD thesis, University of Kaiserslautern, 2002.

[33] R. Keck and D. Hietel. *A projection technique for incompressible flow in the meshless finite volume particle method*. Advances in Computational Mathematics, 23:143-169, 2005.

[34] R. M. Nestor, M. Basa, M. Lastiwka and N. J. Quinlan. *Extension of the finite volume particle method to viscous flow*. Journal of Computational Physics, 228:1733-1749, 2008.

[35] D. Teleaga. *A finite volume particle method for conservation laws*. PhD thesis, University of Kaiserslautern, 2005.

[36] E. Oñate, S. Idelsohn, O. C. Zienkiewicz, R. L. Taylor and C. Sacco. *A stabilized finite point method for analysis of fluid mechanics problems*. Computer Methods in Applied Mechanics and Engineering, 139: 315-346, 1996.

[37] S. Tiwari and J. Kuhnert. *Finite Pointset Method Based on the Projection Method for Simulations of the Incompressible Navier-Stokes Equations*. Lecture Notes in Computational Science and Engineering 26:373-388, 2003.

[38] S. Tiwari and J. Kuhnert. *Modeling of two-phase flows with surface tension by finite pointset method (FPM)*. Journal of Computational and Applied Mathematics 203-2:376-386, 2007.

[39] R. Vacondio and P.Mignosa. *Incompressible Finite Pointset method for free surface flow*. Proceeding of 4th SPHERIC International workshop, Nantes, France, 201-208, 2009.

[40] S. Koshizuka, H. Tamako and Y. Oka. *A particle method for incompressible viscous flow with fluid fragmentation*. Comput. Fluid Dyn. J. 4(1), 29-46, 1995.

[41] G.H. Cottet, P.D. Koumoutsakos. *Vortex methods: theory and practice*. Cambridge University Press, 2000.

[42] L. Hernquist and N. Katz. *Treesph: A unification of sph with the hierarchical tree method*. The Astrophysical Journal Supplement Series, 70, 419-446, 1989.

[43] R.P. Nelson and J.C.B. Papaloizou. *Variable smoothing lengths and energy conservation in smoothed particle hydrodynamics*. Monthly Notices of the Royal Astronomical Society, 270, 1-20, 1994.

[44] H. Martel, P. Shapiro, J. Villumsen and H. Kang. *Adaptive smoothed particle hydrodynamics with application to galaxy and large-scale structure formation*. Mem. Soc. Astron. It., 65(4), 1061-1071, 1994.

[45] J.W. Swegle, S.W. Attaway, M.W. Heinstein, F.J. Mello and D. Hicks. *An analysis of smooth particle hydrodynamics*. Sandia Report SAND93-2513, 1994.

[46] J.W. Swegle, D. Hicks and S.W. Attaway. *Smoothed particle hydrodynamics stability analysis*. Journal of Computational Physics, 116, 123-134, 1995.

[47] J.C.B. Dyka, P.W. Randles and R.P. Ingel. *Stress points for tension instability in SPH*. International Journal for Numerical Methods in Engineering, 40:2325-2341, 1997.

[48] P.W. Randles and L.D. Libersky. *Smoothed particle hydrodynamics: some recent improvements and applications*. Computer Methods in applied mechanics and engineering, 139, 375-408, 1996.

[49] D.A. Mandell, C.A. Wingate, G.A. Dilts and L.A. Schwalbe. *Computational Brittle Fracture Using Smooth Particle Hydrodynamics (U)*. Los Alamos National. Lab. Report: LA-CP-96-209, 1996.

[50] J.J. Monaghan. *SPH without a tensile Instability*. Journal of Computational Physics, 159, 290-311, 2000.

[51] P. Español and M. Revenga. *Smoothed dissipative particle dynamics*. Physical Review E, 67, 026705, 2003.

[52] A. Colagrossi, M. Antuono and D. Le Touzé, *Theoretical considerations on the free surface role in the SPH model*. Physical Review E, 79 (5), pp. 1-13, 2009.

[53] J.P. Vila. *On Particle Weighted Methods and SPH*. Mathematical Models and Methods in Applied Science, 9, 61-210, 1999.

[54] M. Antuono, A. Colagrossi, S. Marrone and D. Molteni. *Free-surface flows solved by means of SPH schemes with numerical diffusive terms*. Computer Physics Communications, 181, 532-549, 2010.

[55] S. Marrone, M. Antuono, A. Colagrossi, G. Colicchio, D. LeTouzé and G. Graziani. *Violent Fluid-structure impacts solved through a δ-SPH model*. Proceeding of 5th SPHERIC International workshop, Manchester, UK, 114-121, 2010.

[56] M. Antuono, S. Marrone, A. Colagrossi and C. Lugni. *Propagation of gravity wave-packets through a δ-SPH method*. Proceeding of 5th SPHERIC International workshop, Manchester, UK, 122-129, 2010.

[57] J.J. Monaghan and A. Kos. *Solitary waves on a Cretan beach*. J. Waterways Port Coastal Ocean Eng. 125(3), 145-54, 1999.

[58] M. Landrini, A. Colagrossi, M. Greco, M.P. Tulin, *Gridless simulations of splashing processes and near-shore bore propagation*, Journal of Fluid Mechanics, 591, pp. 183-213, 2007.

[59] J.J. Monaghan, A. Kos and N. Issa. *Fluid motion generated by impact*. J. Waterway Port Coastal Ocean Eng. 129, 250-259, 2004.

[60] R.A. Dalrymple and B.D. Rogers. *Numerical modeling of water waves with the SPH method*. Coastal Eng., 53, 141-147, 2006.

[61] S.J. Cummins and M. Rudman. *An SPH projection method*. ournal of Computational Physics, 152, 584-607, 1999.

[62] S. Shao and E.Y.M. Lo. *Incompressible SPH method for simulating Newtonian and non-Newtonian flows with a free surface*. Advances in Water Resources, 26(7), 787-800, 2003.

[63] S. D. Shao, C. Ji, D.I. Graham, D.E. Reeve, P.W. James and A.J. Chadwick. *Simulation of wave overtopping by an incompressible SPH model*. Coastal Engineering, 53(9), 723-735, 2006.

[64] H. Gotoh, S.D. Shao and T. Memita. *SPH-LES model for numerical investigation of wave interaction with partially immersed breakwater*. Coastal Eng. Jour., JSCE, 46(1), 39-63, 2004.

[65] S.D. Shao and H. Gotoh. *Simulation coupled motion of progressive wave and floating curtain wall by SPH-LES model*. Coastal Eng. Jour., JSCE, 46(2), 171-202, 2004.

[66] S. Marrone, A. Colagrossi, D. Le Touzé and G. Graziani. Fast free-surface detection and level-set function definition in SPH solvers. Journal of Computational Physics, 229 (10), 3652-3663, 2010.

[67] G.A. Dilts. *Moving-least-squares-particle hydrodynamics - I. Consistency and stability*. International Journal for Numerical Methods in Engineering Volume, 44(8), 1115-1155, 1999.

[68] M. Ellero, M. Serrano and P. Español. *Incompressible smoothed particle hydrodynamics*. Journal of Computational Physics, 226(2),1731-1752, 2007.

[69] J.J. Monaghan. *Smoothed particle hydrodynamics*. Ann. Rev. Astron. Astrophys. 30, 543-574, 1992.

[70] H. Takeda, S.M. Miyama and M. Sekiya. *Numerical simulation of viscous flow by Smoothed Particle Hydrodynamics*. Prog. Theor. Phys., 92(5), 939-960, 1994.

[71] J.P. Morris, Y. Zhu, P.J. Fox. *Modeling Low Reynolds Number Incompressible Flows Using SPH*, Journal of Computational Physics, 136, 214-226, 1997.

[72] J. Fang, A. Parriaux, M. Rentschler and C. Ancey. *Improved SPH methods for simulating free surface flows of viscous fluids*. Applied Numerical Mathematics, 59(2), 251-271, 2009.

[73] R. Nestor, M. Basa, M. Lastiwka and N.J. Quinlan. *Extension of the finite volume particle method to viscous flow*. Journal of Computational Physics, 228(5), 1733-1749, 2009.

[74] A. Colagrossi, M. Antuono, A. Souto-Iglesias and D. Le Touzé. *Theoretical analysis of SPH in simulating free-surface viscous flows*. Proceeding of 5th SPHERIC International workshop, Manchester, UK, 138-145, 2010.

[75] W.C. Welton. *Two-dimensional PDF/SPH simulations of compressible turbulent flows*. Journal of Computational Physics, 139, 410-443, 1998.

[76] G.J. Wagner and W.K. Liu. *Turbulence Simulation and Multiple Scale Subgrid Models*. Computational Mechanics, 25, 2/3, 117-136, 2000.

[77] H. Gotoh, T. Shibahara and T. Sakai. *Sub-Particle-Scale Turbulence Model for the MPS Method -Lagrangian Flow Model for Hydraulic Engineering*. Comput. Fluid Dynamics Jour., 9(4), 339-347, 2001.

[78] J.J. Monaghan. *SPH compressible turbulence*. Monthly Notices of the Royal Astronomical Society, 335 (3), 843-852, 2002.

[79] J.J. Monaghan. *An SPH Turbulence Model*. Proceeding of 4th SPHERIC International workshop, Nantes, France, 187-191, 2009.

[80] D. Violeau and R. Issa. *Numerical modelling of complex turbulent free surface flows with the SPH Lagrangian method: an overview*. Int. J. Num. Meth. Fluids, 53(2):277-304, 2007.

[81] J.J. Monaghan and A. Kocharyan. *SPH simulation of multi-phase flow*. Computuer Physics Commununication, 87, 225, 1995.

[82] J.J. Monaghan, R.A.F. Cas, A. Kos and M. Hallworth. *Gravity currents descending a ramp in a stratified tank*. Journal of Fluid Mechanics, 379, 39-69, 1999.

[83] X.Y. Hu and N.A.Adams. *A multi-phase SPH method for macroscopic and mesoscopic flows*. Journal of Computational Physics, 213 (2), 844-861, 2006.

[84] X.Y. Hu and N.A.Adams. *An incompressible multi-phase SPH method*. Journal of Computational Physics, 227(1), 264-278, 2007.

[85] X.Y. Hu and N.A.Adams. *A constant-density approach for incompressible multi-phase SPH*. Journal of Computational Physics, 228 (6), 2082-2091, 2009.

[86] A.M. Tartakovsky and P. Meakin. *Modeling of surface tension and contact angles with smoothed particle hydrodynamics*. Physical Review E, 72, 026301, 2005.

[87] S. Adami, X.Y. Hu and N.A. Adams. *A new surface-tension formulation for multi-phase SPH using a reproducing divergence approximation*. Journal of Computational Physics, 229(13), 5011-5021, 2010.

[88] P.W. Cleary and J.J. Monaghan. *Conduction modelling using Smoothed Particle Hydrodynamics*. Journal of Computational Physics, 148, 227-264, 1999.

[89] Y. Zhu and P.J. Fox. *Smoothed Particle Hydrodynamics model for diffusion through porous media*. Trasport in Porous Media, 43, 441-471, 2001.

[90] Y. Zhu and P.J. Fox. *Simulation of pore-scale dispersion in periodic using Smoothed Particle Hydrodynamics*. Journal of Computational Physics, 182, 622-645, 2002.

[91] A.M. Tartakovsky and P. Meakin. *A Smoothed Particle Hydrodynamics model for miscible flow in three-dimensional fractures and the two-dimensional Rayleigh-Taylor instability*. Journal of Computational Physics, 207, 610-624, 2005.

[92] A.M. Tartakovsky, P. Meakin, T.D. Scheibe and R.M.E. West. *Simulations of reactive trasport and precipitation with Smoothed Particle Hydrodynamics*. Journal of Computational Physics, 222, 654-672, 2007.

[93] S. Manenti, A. Di Monaco, M. Gallati, S. Sibilla, G. Agate, R. Guandalini and A. Maffio. *Simulating rapid sediment scour by water flow with SPH*. Proceeding of 4th SPHERIC Workshop, Nantes, 145-149, 2009.

[94] S. Adami, X.Y. Hu and N.A. Adams. *A conservative SPH method for surfactant dynamics*. Journal of Computational Physics, 229 (5), 1909-1926, 2010.

[95] J.P. Morris. *Simulating surface tension with Smoothed Particle Hydrodynamics*. International Joornal for Numerical Methods in Fluids, 33, 333-353, 2000.

[96] S. Nugent and H. Posch. *Liquid drops and surface tension with Smoothed Particle Applied Mechanics*. Physical Review E - Part A 62(4), 4968-4975, 2000.

[97] S. Marrone, M. Antuono, A. Colagrossi, G. Colicchio and G. Graziani. *Enhanced Boundary Treatment in 2D Smoothing Particle Hydrodynamics Model*. Proceedings of XIX AIMETA Congress of Theoretical and Applied Mechanics, Ancona, Italy, 2009.

[98] J. Fang, R.G. Owens, L. Tacher and A. Parriaux. *A numerical study of the SPH method for simulating transient viscoelastic free surface flows*. Journal of Non-Newtonian Fluid Mechanics, 139, 68-84, 2006.

[99] T. P. Fries and H.G. Matthies. *Classification and Overview of Meshfree Methods*, Informatikbericht 2003-03, Institute of Scientific Computing, Technical University Braunschweig, Brunswick, Germany, 2004.

[100] M. De Leffe, D. Le Touzé and B. Alessandrini. *Normal flux method at the boundary for SPH*. Proceeding of 4th SPHERIC International workshop, Nantes, France, 150-156, 2009.

[101] M. Ferrand, D. Laurence, B.D. Rogers and D. Violeau. *Improved time scheme integration approach for dealing with semi analytical boundary conditions in SPARTACUS2D*. Proceeding of 5th SPHERIC International workshop, Manchester, UK, 98-105, 2010.

[102] J. Bonet, S. Kulasegaram, M.X. Rodriguez-Paz and M. Profit. *Variational formulation for the smooth particle hydrodynamics (SPH) simulation of fluid and solid problems*. Computer Methods in Applied Mechanics and Engineering, 193 (12-14), 1245-1256, 2004.

[103] M. Lastiwka, M. Basa and N.J. Quinlan. *Permeable and non-reflecting boundary conditions in SPH*. International Journal for Numerical Methods in Fluids, 61(7), 709-724, 2008

[104] J.J. Monaghan. *Smoothed Particle Hydrodynamics*. Reports on Progress in Physics, 68, 1703-1759, 2005.

[105] G.R. Johnson, R. A. Stryk and S. R. Beissel. *SPH for high velocity impact computations*. Computer Methods in applied mechanics and engineering 139, 347-373, 1996.

[106] J.J. Monaghan and J.C. Lattanzio. *A refined particle method for astrophysical problems*. Astronomy and Astrophysics, 149, 135-143, 1985.

[107] H. Wendland. *Piecewise polynomial, positive definite and compactly supported radial functions of minimal degree*. Advances in Computational Mathematics, 4(1), 389-396, 1995.

[108] J. Hongbin and D. Xin. *On criterions for Smoothed Particle Hydrodynamics kernels in stable field*, J. Comput. Phys. 202, 699-709, 2005.

[109] J.P. Morris. *Analysis of Smoothed Particle Hydrodynamics with applications*. PhD Thesis, Monash University, 1-169, 1996.

[110] J.J. Monaghan and R.A. Gingold. *Shock simulation by the particle method SPH*. Journal of Computational Physics, 52, 374-389, 1983.

[111] G.K. Batchelor. *An introduction to fluid dynamics*. Cambridge Univ. Press, Cambridge, 1-615, 1967.

[112] P.A. Madsen and H.A. Scäffer. *A discussion of artificial compressibility*. Coastal Engineering 53, 93-98, 2006.

[113] D. Molteni and A. Colagrossi. *A simple procedure to improve the pressure evaluation in hydrodynamic context using the SPH*. Computer Physics Communications, 180, 861-872, 2009.

[114] T. Belytschko, Y. Krongauz, J. Dolbow and C. Gerlach. *On the Completeness of Meshfree Particle Methods*. International Journal for Numerical Methods in Engineering, 43:785-819, 1998.

[115] J. Bonet and T.S.L. Lok. *Variational and momentum preservation aspects of smooth particle hydrodynamic formulations*. Computer Methods in Applied Mechanics and Engineering, 180, 97-115, 1999.

[116] E.G. Flekkøy, P.V. Coveney and G. de Fabritiis. *Foundations of dissipative particle dynamics*. Phys. Rev. E, 62(2), 2140-2157, 2000.

[117] A. Colagrossi, L. Delorme, J.L. Cercòs-Pita and A. Souto-Iglesias. *Influence of Reynolds number on shallow sloshing flows*. Proceeding of 3rd SPHERIC International workshop, Lausanne, Switzerland, 2008.

[118] B. Lafaurie, C. Nardone, R. Scardovelli, S. Zaleski and G. Zanetti. *Modelling merging and fragmentation in multiphase flows with SURFER*. J. Comput. Phys., 113(1), 134-147, 1994.

[119] S.A. Socolofsky and G.H. Jirka. *Special Topics in Mixing and Transport Processes in the Environment*. Texas AM University, College Station, 1-172, 2004.

[120] A.E. Fick. *Poggendorff's Annelen der Physic*. 94, 1-59, 1885.

[121] H.B. Fischer, E.G. List, R.C.Y. Koh, J. Imberger and N.H. Brooks. *Mixing in Inland and Coastal Waters*. Academic Press, New York, 1-483, 1979.

[122] L. Brookshaw. *A method of calculating radiative heat diffusion in particle simulations*. Astronomical Society of Australia, 6, 207-210, 1985.

[123] S. Chapra. *Surface Water-Quality Modeling*. Ed. McGraw-Hill, New York, 1997.

[124] P. Veltri, A. Fiorini Morosini, G. Maradei and B. Verbeni. *Analysis of the re-oxigenation process in water streams*. Proceeding of 32th Congress of IAHR, the International Association of Hydraulic Engineering & Research, Harmonizing the Demands of Art and Nature in Hydraulics, Venice, 2007.

[125] W.G. Whitman. *The two-film Theory of gas absorption*. Chem. Metallurg. Eng., 29(4), 146-148, 1923.

[126] J.J. Monaghan. *Simulating gravity currents with SPH lock gates*. Applied Mathematics Reports and Preprint, 95/5, 1995.

[127] G. Oger. *Aspects théoriques de la méthode SPH et applications à l'hydrodynamique à surface libre*. PhD Thesis, Ecole Centrale de Nantes, France, 2006 (in French).

[128] A. Souto-Iglesias, L.M. Gonzàlez, A. Colagrossi and M. Antuono. *SPH no-slip BC implementation analysis at the continuous level*. Proceeding of 5th SPHERIC International workshop, Manchester, UK, 29-36, 2010.

[129] J.P. Morris, Y. Zhu and P. J. Fox. *Parallel simulations of pore-scale flow through porous media*. Computers and Geotechnics, 227-246, 1999.

[130] A. Valizadeh, M. Shafieefar, J.J. Monaghan and S.A.A. Salehi Neyshaboori. *Modeling Two-Phase Flows Using SPH Method*. Journal of Applied Sciences, 8(21), 3817-3826, 2008.

[131] F. Aristodemo, S. Marrone, A. Panizzo, T. Capone, P. De Girolamo and P. Veltri. *A lagrangian SPH model to simulate a non-steady flow on a triangular sill*. Proceeding of 3th SCACR International Short Course and Workshop on Applied Coastal Research, Lecce, 240-251, 2008.

[132] F. Aureli, P. Mignosa and M. Tomirotti. *Dam-Break flows in presence of abrupt bottom variations*. Proceedings of The XXVIII IAHR International Congress, Graz, 1999.

[133] J. Leduc, J.C. Marongiu, F. Leboeuf, M. Lance and E. Parkinson. *Multiphase-SPH: A new model based on acoustic riemann solver*. Proceeding of 4th Int. SPHERIC Workshop, Nantes, France, 8-13, 2009.

[134] W.H. Graf and M.S. Altinakar, *Fluvial Hydraulics (Flow and transport processes in channels of simple geometry)*, John Wiley and Sons, Lld, 1998.

[135] U.S. Bureau of Reclamation, *Research studies on stilling basins, energy dissipators, and associated appurtenances*, Hydraulic Laboratory Report, n. Hyd-399, 1955.

[136] J.N. Bradley, A.J. Peterka, *The hydraulic design of stilling basins*, Journal of Hydraulic Division, 83(5), pp. 1401-1406, 1957.

[137] J.S. Montes, H. Chanson, *Characteristics of undular hydraulic jumps: Experiments and analysis*, Journal of Hydraulic Engineering, 124(2), pp. 192-205, 1998.

[138] R. Reinauer, W.H. Hager, *Non-breaking undular hydraulic jump*, Journal of Hydraulic Research, 33(5), pp. 683-698, 1995.

[139] I. Ohtsu, Y. Yasuda, H. Gotoh, *Characteristics of undular jumps in rectangular channels*, Proc. 26th IAHR Congr., Hydra 2000, London, U.K., 1997.

[140] D. Lopez, R. Marivela, L. Garrote, *Smoothed particle hydrodynamics model applied to hydraulic structures: a hydraulic jump test case*, Journal of Hydraulic Research, 47 (extra issue), pp. 142-158, 2009.

[141] H.G. Hornung, C. Willert, S. Turner, *The flow field downstream of a hydraulic jump*, Journal of Fluid Mechanics, 287, pp. 299-316, 1995.

ASSOCIATED PUBBLICATIONS

- FEDERICO I., MARRONE S., COLAGROSSI A., ARISTODEMO F., VELTRI P., *An algorithm to treat upstream/downstream boundary conditions in open-channel flows through SPH model.* Computer Physics Communication, *under review*, 2010.

- ARISTODEMO F., FEDERICO I., VELTRI P., PANIZZO A., *Two-phase SPH modelling of advective diffusion processes*. Environmental Fluid Mechanics, Vol. 10, pp. 451-470, 2010.

- ARISTODEMO F., FEDERICO I., VELTRI P., *Evoluzione di fluidi bifase e di fenomeni diffusivi attraverso la tecnica SPH*. L'ACQUA, Vol. 4, pp. 63-70, 2010 (in Italian).

- FEDERICO I., MARRONE S., COLAGROSSI A., ARISTODEMO F., VELTRI P., *Simulating free-surface channel flows through SPH*. Proceeding of V International Spheric SPH Workshop, Manchester, UK, 2010.

- FEDERICO I., MARRONE S., COLAGROSSI A., ARISTODEMO F., VELTRI P., *Simulations of hydraulic jump through SPH model*. Proceeding of XXXII Italian Conference of Hydraulic and Hydraulic Constructions, Palermo (Italy), 2010.

- ARISTODEMO F., FEDERICO I., VELTRI P., PANIZZO A., *SPH simulations of advective-diffusion phenomena induced by pollutants in water*. Proceeding of V International Spheric SPH Workshop, Manchester, UK, 2010.

- ARISTODEMO F., FEDERICO I., VELTRI P., *Modellazione numerica SPH applicata a problemi di idraulica ambientale*. Proceeding of "Acqua & Città" - III Italian Urban Hydraulic Conference, Milan (Italy), 2009 (in Italian).

- VERBENI B., VELTRI P., MARADEI G., FIORINI MOROSINI A., FEDERICO I., *Sulle difficoltà connesse alla limitata disponibilità di dati per le previsioni dello stato di qualità di un fiume*. Proceeding of *XXIX Tecniche per la difesa dall'inquinamento*, Guardia Piemontese, Cosenza (Italy) Nuova Bios, 2008 (in italian).

COLOPHON

This thesis has been typeset with $\LaTeX\,2_\varepsilon$ on Windows XP using *ArsClassica*, a package developed by Lorenzo Pantieri (I would like to thank him). This package is a re-elaboration of *ClassicThesis* style by Andrè Miede. The *ClassicThesis* style, inspired to Robert Bringhurst work *The Elements of Typographic Style* (1992), is available on CTAN web site. The graphics custum of this thesis can be reproduced uploading the package *ArsClassica*, also available on CTAN or on www.lorenzopantieri.net.

NOTE: This work has been realized using Hermann Zapf's Palatino (Type 1 PostScript fonts URW Palladio L and FPL have been used) and Euler type faces for Mathematics formulæ. The listings are typeset in Bera Mono, originally developed by Bitstream, Inc. as "BitstreamVera".

Definitive version: November 26, 2010.